UNIVERSIDAD NACIONAL AUTÓNOMA DE MÉXICO

POSGRADO EN CIENCIA E INGENIERÍA DE MATERIALES

INSTITUTO DE INVESTIGACIONES EN MATERIALES

BOVINE PERICARDIUM RANDOM LASERS AND OPTOMECHANICAL TESTING

TESIS

QUE PARA OPTAR POR EL GRADO DE

DOCTOR EN CIENCIA E INGENIERÍA DE MATERIALES

PRESENTA

NATANAEL BENITO CUANDO ESPITIA

TUTOR PRINCIPAL

DR. JUAN ARNALDO HERNÁNDEZ CORDERO

INSTITUTO DE INVESTIGACIONES EN MATERIALES

COMITÉ TUTOR

DR. CRESCENCIO GARCÍA SEGUNDO

CENTRO DE CIENCIAS APLICADAS Y DESARROLLO TECNOLÓGICO

DR. MAYO VILLAGRÁN MUNIZ

CENTRO DE CIENCIAS APLICADAS Y DESARROLLO TECNOLÓGICO

MÉXICO, D.F., OCTUBRE DE 2015.

AGRADECIMIENTOS

Este trabajo hubiera sido imposible sin el apoyo del **IIM** que facilitó las instalaciones y el equipo esencial para este trabajo. Gracias también a la **UNAM** que destino recursos para este trabajo a través del proyecto **PAPIIT-IT 101215**. Gracias al **Concejo Nacional de Ciencia y Tecnología** por otorgar la beca doctoral en tiempo y forma. Gracias a mi asesor **Dr. Juan Hernández Cordero** por toda la presión, la guía y la confianza que se me ha brindado. Gracias a mi comité tutor **Dr. Mayo Villagrán Muniz** y **Dr. Crescencio García Segundo** y al **Dr. Francisco Sánchez Arévalo** por sus invaluables comentarios y enseñanzas. Gracias a todos mis compañeros **del laboratorio de sensores de fibra y fibra óptica láser** y del IIM por permitirme compartir con ustedes espacios, materias, exámenes, y risas. Gracias a la gente de la coordinación del **PCeIM** por su inagotable paciencia. Gracias a mi familia por su constante apoyo. Gracias ***Ana Laura*** por mostrar tanto amor hacia este humilde payasito de crucero.

19 de Octubre 2015

En memoria de:

Benito Cuando Celis
Mario Alfredo Ibarra Pereyra

INDEX

CHAPTER 5

CHAPTER 6

INTRODUCTION

Emission of coherent light is generally associated with optical resonators. In these devices, light travels describing trajectories that are repeated after completing a round trip [1]. Fabry-Perot resonators, for example, base their operation on multiple reflections of light between two parallel mirrors. When an active medium is placed within a resonator, light within the device interacts with the active medium in each round trip and stimulated emission is achieved, thus leading to laser action [2]. However, there are other ways to generate lasing phenomena, such as using multiple scattering of light as a feedback mechanism. Generation of coherent optical radiation with this effect is known as random lasing, and is an optical phenomenon that generates coherent emission in a medium with a disordered structure [3].

The simplest way to generate random laser action is using a liquid laser medium with particles. When scattering particles are added to this active medium, the generated light is scattered within the medium allowing for an increased interaction with the active medium; hence, the conditions for the stimulated emission of light may be generated. In these lasers, the characteristics of the emitted light such as the resonance wavelength, polarization and spatial profile are determined by the set of scattering particles [3]. The dependence of the laser light with the disordered scattering media makes these systems useful for applications such as characterization of complex materials [4], micrometer laser sources [5] and photodynamic therapy [6], to name a few. During the last decade, there have been reports on random lasers based on lasers powders [7], liquid crystals [8], dielectric particles [9], electroluminescent materials [10] and biological tissue [11, 12].

Recently, random lasers have attracted attention due to their potential use in tissue characterization. The basic idea for this application has been to correlate the spectral features of random lasing with tissue pathologies such as cancer [11, 12]. According to previous reports on random lasers, the change in the scatterer size maps to a shift in emission wavelength [13]. This leads to the possibility of using random laser emission as an indicator of the size and concentration of scatterers within the disordered material. As an example, this idea has been exploited to detect microfractures in bone tissue [4]. In a

theoretical study, it has been demonstrated that even a single scatterer added to the ensemble may dramatically change the random laser emission [5]. In this sense, random laser emission has the potential to enhance the detection sensitivity of passive optical methods such as dynamic light scattering. In general, one can obtain random laser emission from multiple scattering materials by incorporating an adequate active medium. In this work, we study the random laser emission from bovine pericardium treated with a solution of Rhodamine 6G as a laser medium. Furthermore, we incorporate this and other optical techniques in tensile tests to directly correlate the optical measurements with the mechanical response of the tissue.

MOTIVATION AND OBJECTIVES

Most patients with heart valve disorders will require surgery to repair or replace the heart valves [14]. This has been a serious health issue and has led to develop several types of prosthetic heart valves, which are generally classified into mechanical and biological prosthetic valves. The latter are known as bioprosthetic heart valves and they are attractive for patients because a lifelong anticoagulation treatment is not required [15]. Nevertheless, the long-term durability of theses valves is mostly limited by calcification, which leads to progressive tissue degeneration and eventually to valve failure. Recent studies aimed at improving valve performance have focused on the fluid dynamics governing different valve replacement designs [16]. These are relevant because they may lead to the ability of proposing new valve replacement designs based on material parameters needed to mimic the natural flow within the heart. In the case of bioprosthetic valves, the complex structure of the tissue ultimately determines the mechanical properties of valve leaflets. This in turn leads to the need of mechanical characterization of tissue in order to predict its mechanical response under applied loads.

This work presents the first study related to random lasing obtained from bovine pericardium treated with a solution based on an organic dye solution. The motivation to study bovine pericardium is its widespread use as replacement heart valves, biological patch and cellular scaffold [17]. We thus explore the use of optical techniques as a means to address the actual needs for mechanical characterization of this tissue. The pericardium is a membrane covering the heart of mammals, showing a uniform and suitable thickness for valve replacement applications. Despite its widespread use for this purpose, the lifetime of this type of valve is reduced. As an example, it has been observed that processes such as calcification increase the stiffness of the pericardium generating disturbances in blood flow, blood pressure and hence increasing the risk of valve failure [15-17]. Among other important achievements, a detailed study of the structural characteristics of this tissue would allow improving the performance of valve replacements based on bovine

pericardium. Since the mechanical properties of the tissue are determined by its own structure, knowledge of the structural features would allow for optimizing the mechanical performance of these materials. In principle, random laser emission can provide information about tissue structure because the spectral features, such as the wavelength and spectral width, are dependent on the multiple scattering events that photons experience before leaving the disordered material [3].

Along with the random laser emission from pericardium tissue we have explored optical passive techniques such as enhanced backscattering and Müller matrix imaging in order to compare the results of random lasing. Enhanced backscattering is an optical phenomenon in which an increase of intensity appears near the backscattering direction [18]. In this effect, the angular distribution of the intensity depends on the mean distance of scatterers inside the material. Recently we have performed enhanced backscattering measurements in bovine pericardium tensile test showing a good correlation with the stress-elongation ratio [19]. In addition, Müller matrix imaging has proved to be a suitable technique to elicit information from biological tissue [20]. In few words, Müller matrix calculus is the polarization analysis of a light beam after interacting with an optical device. Among the interesting features of this method is the direct evaluation of optical parameters such as retardance and optical rotation. In general, both techniques can give information about the internal structure of the tissue owing the scattering and polarization effects of the samples over a known probe beam. We will use these techniques to contrast and compare the results of random laser emission from bovine pericardium samples.

Summarizing, the first objective of this work is to generate random laser emission from bovine pericardium samples. Then, we will design and construct an experimental setup suitable to perform tensile test at the same time that random laser emission from pericardium samples is generated and captured. Moreover, our aim is to correlate the spectral features of random laser emission with the mechanical parameters provided by the tensile test. We will also perform enhanced backscattering measurement and Müller matrix imaging with pericardium samples in order to contrast the information given by the random

laser experiments. Finally, we wish to show a comprehensive evaluation of the random laser emission as an indicator of the deformation in pericardium samples.

The present work is organized as follows: Chapter 1 reviews briefly the basics of random lasers and principal properties of pericardium as a bioprosthetic material. In Chapter 2 the experiments of enhanced backscattering and Müller matrix imaging are described. Chapter 3 covers the macromechanical behavior of tissue samples along with the spectral features of random laser emission during the tensile tests. A study of the polarization of random laser emission is presented in Chapter 4. Chapter 5 deals with a contrast analysis between the random laser emission and the passive techniques shown in Chapter 2. Finally, in Chapter 6 we present the conclusions and future work.

CHAPTER 1

BACKGROUND

1.1. BASIC CONCEPTS OF LASERS

1.1.1. Emission and absorption in active media

Laser systems are based on the processes of absorption, spontaneous emission and stimulated emission [1, 2]. These processes describe the interaction of light with matter via electronic transitions. Electromagnetic radiation and matter interact because the latter is formed by electrically charged particles. Light and matter interactions may provide access to higher energy states for electrons otherwise located in lower orbitals. Aside from the probabilistic nature of these effects, this condition is achieved if the photon energy equals the energy difference between the electron energy states. Energy states of matter are governed by the laws of quantum mechanics. In general, it is not easy to determine the energy states of electrons and some approaches have been used involving the approximation of the molecular wave function. These approaches have proved to be very useful in describing light and matter interactions.

Once the electrons reach a higher energy state, they remain in that state a time τ before decaying to its original state. The decay time τ between two energy states is known as spontaneous lifetime, and is a characteristic feature for each material as it depends on the atomic structure. During electron decay, the absorbed energy can be delivered in a radiative or a non-radiative way. When radiative decay takes place, photons are emitted with equal energy to the energy difference between electronic states [1]. In the case of non-radiative decay, energy is transferred to the atomic structure by quantized vibrations called phonons. The proportion of electrons decaying radiatively and non-radiatively after absorption is also a distinctive feature of the material. Those materials having a high proportion of radiative decays are known as active media and they are one of the key elements in laser systems. In contrast, passive absorbent materials deliver the absorbed

energy mostly in the form of non-radiative decays. Absorption and emission processes are illustrated with hypothetical energy diagrams in Figure 1.1.

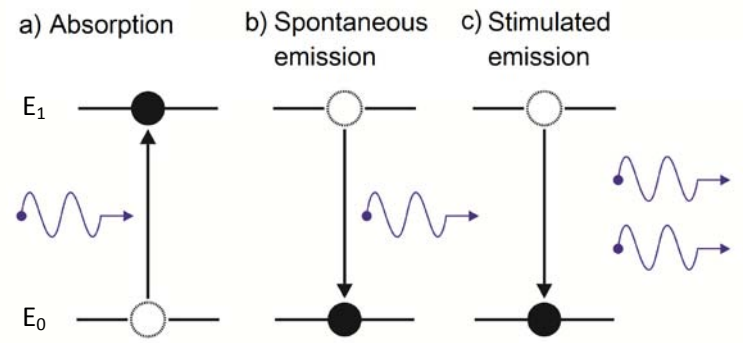

Figure 1.1. Absorption and emission processes in active media. In a) an electron is promoted to a higher-level state; while in b) a photon is emitted when electron decay to a lower energy state. In c) an external photon stimulates the decay; both photons have the same wavelength and same phase. E_1 and E_0 indicate energy levels which holds the condition $E_1>E_0$.

Radiative decays can occur as spontaneous emission or stimulated emission. Spontaneous emission occurs when electrons in excited states decay after a characteristic time τ. Photons generated by spontaneous emission have random propagation directions and phases. Moreover, stimulated emission occurs when a photon interacts with an electron in an excited state and thus promotes the radiative decay. The photon originated from this decay propagates in the same direction as the first photon and with the same phase. The chain reaction of stimulated emission processes results in a coherent beam of light. When stimulated emission processes are generated within an optical cavity, the emitted photons are amplified in a preferred direction typically yielding a collimated beam.

1.1.2. Fundamental elements of lasers

Laser systems can be described as optical amplifiers with positive feedback [2]. Optical amplification is achieved with an active medium and an appropriate source of external energy to provide the necessary electronic transitions to obtain a condition known as population inversion. This condition arises from absorption of the external energy in the active medium, leading to electronic transitions of electrons towards higher energy levels.

Since the electrons are effectively taken to a higher electronic state, the external energy source is termed as pump source. During electron decay, photons are emitted via radiative transitions, and some of these photons contribute to generate stimulated emission of additional photons. Regarding the positive feedback, this is achieved by allowing the emission to interact repeatedly with the active medium, which is generally done with optical resonators. Thus, a laser system comprises an active medium, a pumping source and a resonator or optical cavity.

Some active media used in laser systems include crystals such as ruby, or mixtures of gases as in helium-neon lasers; organic dyes such as Rhodamine 6G diluted in a solvent also serve as an active medium. The absorption and emission features for each active medium vary depending on its molecular structure. Thus, the suitable pump source for a specific active medium is determined by the absorption characteristics of the laser material. Population inversion is achieved upon pumping the active medium to increase the electron population in the higher energy levels. Once this condition is achieved and there are holes available (i.e. vacant energy levels) in the material, spontaneous emission and subsequent stimulated emission will lead to laser emission, provided that the gain in the system is higher than the optical losses. Analysis of the electron population dynamics is based on rate equations, involving the lifetimes of the electron at energy levels associated to the absorption and emission processes.

Laser emission originates from the action of an external power source in an active medium inside an optical resonator which provides coherent feedback. Without this feedback the emission of the active medium has a broad spectral width and lacks spatial and temporal coherence. With the exception of random lasers, most laser systems use an optical resonator as a feedback mechanism. An optical resonator stores energy and provides the feedback required to obtain laser emission. The simplest resonator is the Fabry-Perot resonator, formed by two parallel mirrors separated by a known distance. In its simplest form, a laser system includes an active medium and two highly reflective mirrors. This configuration is shown schematically in Figure 1.2.

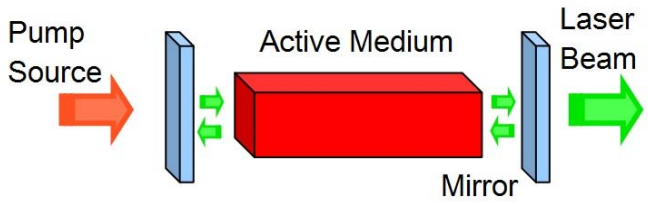

Figure 1.2. General representation of a laser system. Part of the light emitted by the active medium is reflected back to interact again with the active medium (positive feedback).

In a Fabry-Perot resonator, the pump enters from one of the partially reflective mirrors to generate stimulated emission within the gain medium. This stimulated emission is reflected by the mirrors allowing for multiple interactions between the photons and the active medium. The resonator configuration allows for constructive interference to occur at specific frequencies, which are termed as oscillation modes. These can be obtained using the complex representation of the wave function for a monochromatic wave with frequency v [1]:

$$u(\mathbf{r},t) = a(\mathbf{r})\exp[j\varphi(\mathbf{r})]\exp[j2\pi vt] \qquad 1.1$$

The wave function $u(\mathbf{r},t)$ represents the transversal component of the electric field, and the factor $U(\mathbf{r})=a(\mathbf{r})exp[j\varphi(\mathbf{r})]$ is known as the complex amplitude. Since the complex amplitude $U(\mathbf{r})$ satisfies Helmholtz equation:

$$\nabla^2 U(\mathbf{r}) + k^2 U(\mathbf{r}) = 0 \qquad 1.2$$

$$k = \frac{2\pi\upsilon}{c} \text{ (wave number)} \qquad 1.3$$

The resonator modes can be obtained as basic solutions that satisfy Equation 1.2 for appropriate boundary conditions. For a parallel mirrors resonator, and considering $\mathbf{z}$ as the propagation direction, the electric field is zero on the surfaces (that is, $U(\mathbf{r})=0$, for $z=0=d$), hence, the solutions have the form:

$$U(\mathbf{r}) = A\sin(kz) \qquad 1.4$$

With A=constant. In order to satisfy the boundary conditions of Equation 1.4, the function $U(\mathbf{r})$ must be restricted to discrete values of k:

$$kd = q\pi \qquad 1.5$$

This indicates that the resonator frequencies are also discrete and are given by:

$$f = \frac{mc}{2nL} \qquad 1.6$$

Where:

f: resonance frequency

c: speed of light

n: refractive index within the mirrors

L: cavity length

m: positive integer

The resonance frequencies of the resonator are integers multiples of half wavelengths from the length of the cavity. Only those frequencies that meet this condition will oscillate and generate stimulated emission in the active medium. These frequencies are called longitudinal modes of the resonator.

All resonators have losses due to scattering and imperfections in the mirrors surfaces. Furthermore, absorption of the active medium and non-radiative effects will also contribute to losses within the laser cavity. Due to these losses, laser systems always present a threshold for laser emission and this is generally overcome upon increasing the pumping energy. The emission output of the laser system contains the longitudinal modes that are delimited by the emission spectrum of the active medium and those that exceed resonator losses. In general, laser light is spectrally narrow, highly coherent and presents a high energy density.

1.2. RANDOM LASERS

1.2.1. Basics of random lasers

In conventional lasers, the optical cavity that confines the photons determines the essential characteristics of laser emission such as wavelength, emission spectrum and state of polarization. In random lasers, which have no defined cavity or mirrors, the light is confined within the active medium through multiple scattering effects. Figure 1.3 depicts

schematically the general components in a conventional laser and in a random laser.

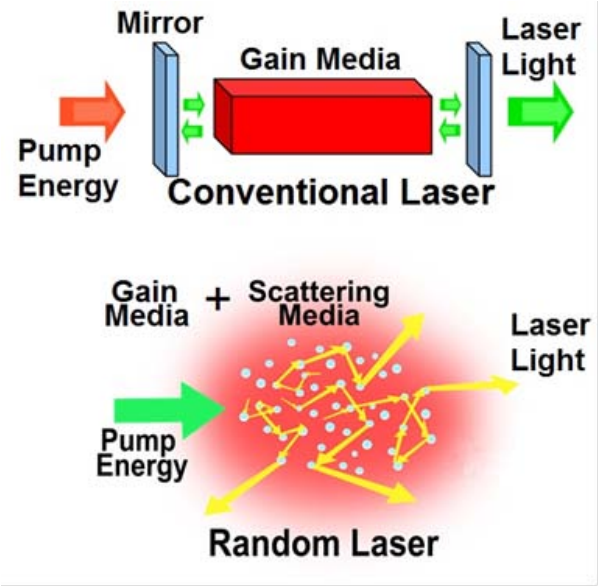

Figure 1.3. Schematic representation of a conventional laser and a random laser. In a random laser, multiple scattering acts as the feedback mechanism.

Theoretical studies on lasing in disordered media started in the early years of lasers physics. However, it was not until 1999 that narrow laser lines (about tenths of nanometer) were reported in semiconductor powders [7]. Despite the many reports on random lasing, the mechanisms enabling the consistent feedback required for laser emission are still under discussion. It has been shown that the experimental observations of random lasers do not meet the conditions of strong multiple scattering required for photon localization [21]. This photon localization would be analogous to Anderson localization regime, which is the confinement of electrons due to extremely strong scattering. On the other hand, the study of these kind of system based on the diffusion equation assumes that the light scattered by a particle is independent of the light scattered by any other particles in the system, i.e., it assumes that coherent interference by multiple scattering is negligible [22]. This simplification becomes invalid for saturated concentrations of particles, in which the mean spacing between the scattering centers is of the same order of magnitude than the size of the scattering particles. Until now, the most general description of this problem has focused on solving the rate equations for a four-level system coupled to the Maxwell equations [23]. The authors of reference [23] model the random medium through the dielectric constant

$\varepsilon(\mathbf{r})$ that is in general a spatial random variable depending on the parameters of the scattering particles. Detailed work discussing this model can be found in references [21, 23]. In these reports, solutions for the rate equations have been obtained using numerical methods such as the finite difference time-domain method (FDTD). In addition, the existence of a low energy threshold for random lasers has also been theoretically verified. Moreover, these theoretical studies have shown two scattering regimes in which random laser emission can be achieved. When the scattering inside a disordered material is high enough to exhibit feedback mechanisms in a spatial length compare with the wavelength of a light beam localized modes appear. In the other hand, when the scattering material produces feedback in a wider scale than the wavelength modes that spread in an expanded area appear (i.e. expanded modes). For Jiang and Soukoulis [23], the scattering force is the principal mechanism that determines the existence of localized modes or expanded modes in the active medium. This scattering force is a parameter depending on the scatterer concentration, refractive index and the geometry of scatterers.

According to Andreasen *et al* [21], the random medium by its elf is capable of generating modes due to interference processes within the random medium. The scattering model consists of a two-dimensional arrangement of scattering particles in random positions. The dimensions of the particles and their positions remain constant, while the refractive index is varied for different scattering forces. As in reference [23], Andreasen *et al* find localized modes for the case of strong scattering force and extended modes for low scattering force.

Analysis of the scattering medium also reveals that the spatial location of the modes with and without active medium is almost the same for a strong scattering force. Another important change observed when the refractive index of the scattering particles is varied is the central emission wavelength. Andreasen *et al* reported a change in the central emission wavelength of $\Delta\lambda\approx10$ nm associated to a change in refractive index from 1.25 to 2.0 [21]. These theoretical findings have been experimentally confirmed in recent studies [24,25]. Random lasers based on silica particles have shown notorious changes in spectral emission

when the concentration or the particle size are varied [25]. Figure 1.4 shows two plots taken from reference [25] in which several random laser spectra are depicted.

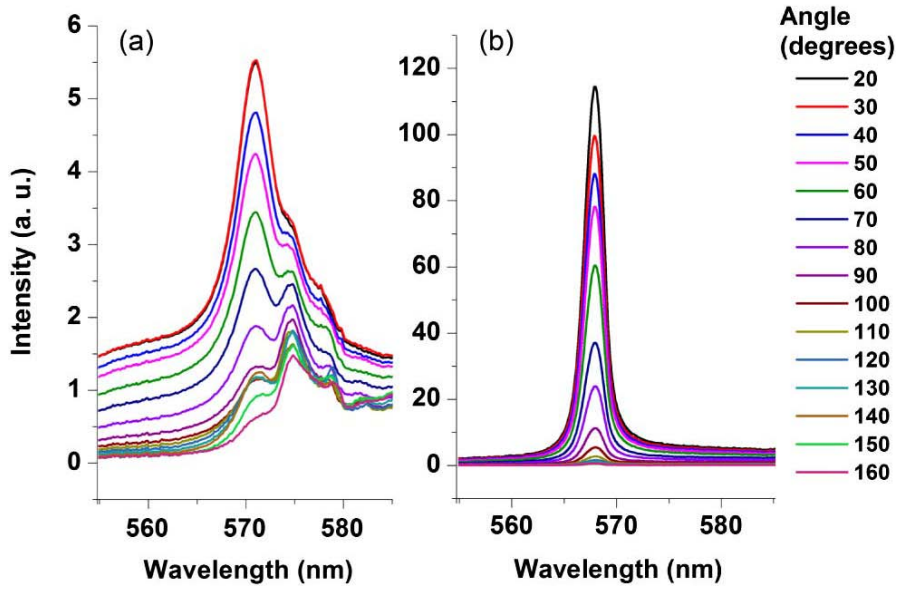

Figure 1.4. Random laser spectra for different angles and pump power fixed. a) 1x10^{11} particles/mL. b) 4x10^{12} particles/mL. With low particle concentration the angular dependence is more evident and the spectral features change dramatically depending on the angle in which the spectrum is captured. The graphs were adapted from reference [25].

The spectra shown in Figure 1.4 were obtained by pumping a solution of Rhodamine 6G dissolved in methanol with SiO_2 nanoparticles incorporated into the dye solution. From Figure 1.4 it is clear that the spectral features strongly depend on the particle concentration but also in the angle in which the spectrum is captured. Figure 1.4 a) shows clearly how the emission spectra have a strong dependence on the angle in which emission is captured. The rich spectral content depicted in Figure 1.4 a) suggests mode competition within the pumped volume. This behavior is expected taking into account the disordered nature of random lasers. Nevertheless, as Figure 1.4 b) shows, when more scattering particles are added (increasing scattering force), the spectral features are angularly preserved. These two behaviors are in accordance to the theoretical description of extended and localized modes explained above. Therefore, the structure of the scattering medium, i.e. the geometry, composition and particle concentration are closely linked to the spectral characteristics of random lasers. Moreover, the ensemble variations in a disordered

media may change dramatically the spectral features of random laser emission. This is very important in applications aiming to find characteristic parameters in complex materials. Anisotropic, micro-structured and non-homogeneous materials are difficult to study because conventional tests aiming to determine their physical parameters cannot provide information effectively. A good example of a complex material is the biological tissue which involves hierarchical structure at micro and meso scales. Therefore, random lasers have the potential to be used for characterization of complex materials such as biological tissue.

1.2.2. Biological random lasers

Despite its potential application in medical diagnosis, few studies have exploited the use of biological material as scattering medium to obtain random laser emission. Some of these studies have been aimed at detecting microfractures in bone [4], malignant tissue identification [11,12] or rapid cell counting [26]. The idea of using random laser action to detect cell abnormalities is very interesting as it can lead to early cancer detection. In general, all the reports mentioned above relate the features of random laser action with the microstructure of the tissue. Polson and Vardeny compared random laser emission from healthy and cancerous tissue samples (human colon) [12]. Spectral analysis of the laser emission enabled tissue mapping to discriminate between healthy and damaged regions in a sample.

Reports on biological random lasers use a solution of Rhodamine 6G as an active medium [9,10]. The samples are pumped with a pulsed laser at a wavelength of 532 nm and the spectral emission is collected and analyzed using the power Fourier transform. Figure 1.5 shows images taken with an optical microscope for the types of tissues analyzed, i.e., healthy and malignant tissue. Clearly, each sample shows different histological features.

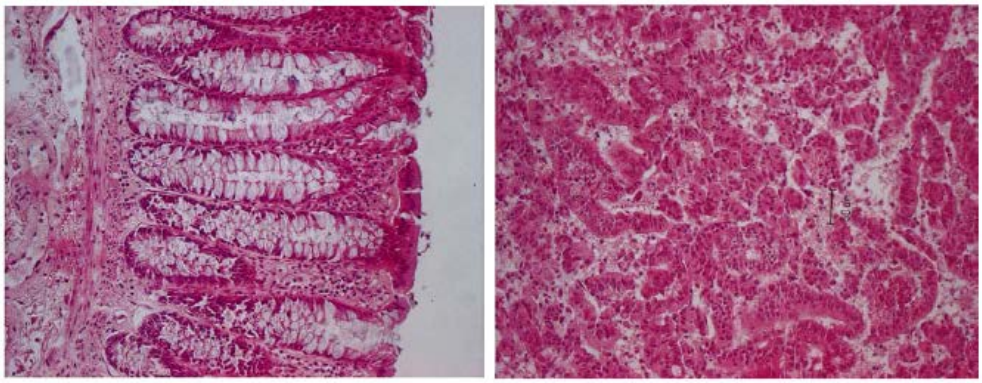

Figure 1.5. Images of histological samples studied in reference [11]. Left: healthy tissue. Right: malignant tissue.

The results from analyzing the random laser emission from both samples show that both the spectral output and the power Fourier transform show a different behavior. Figure 1.6 shows the plots of the spectral emission and the Fourier transform for the cases of healthy tissue and malignant tissue. As shown in the figure, both, the emission spectrum and the power Fourier transform of healthy tissues present significant differences compared to malignant tissues.

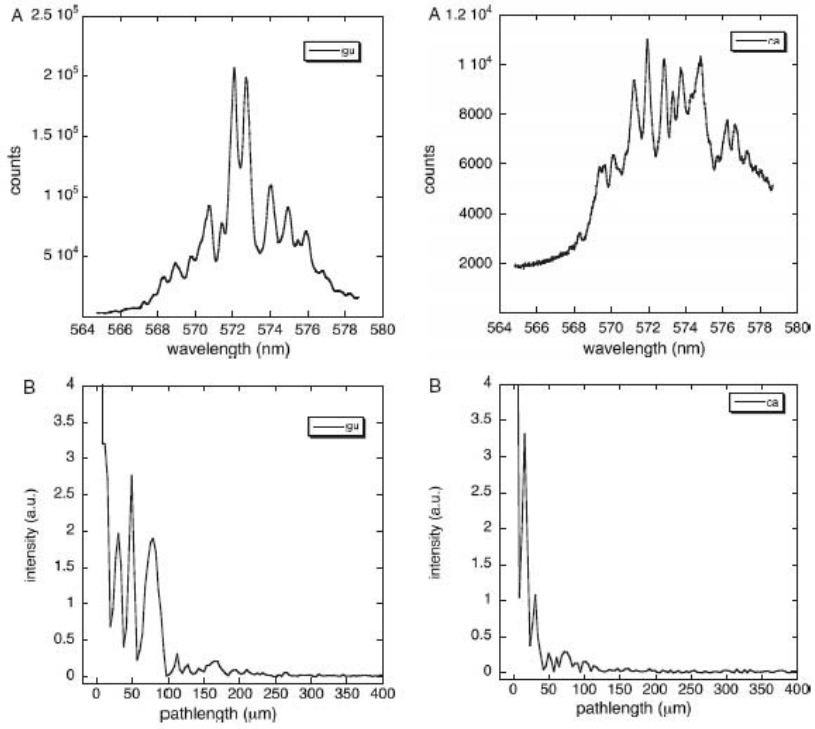

Figure 1.6. Spectral emission (up) and Power Fourier transform (down) of healthy tissue (left) and malignal tissue (right). All the plots are taken from reference [12].

Other studies on random laser emission from biological tissue have related the central emission wavelength with changes in the disordered material such as microfractures or cell concentration. In reference [4], a bone sample was infiltrated with a solution of Rhodamine 800 and subjected to uniaxial strain while being pumped with a tunable pulsed laser. As a result, a shift in the peak wavelength of the emission was registered as the sample was loaded. Figure 1.7 a) shows the spectra of the random laser emission before, during and after the mechanical load. This behavior has been associated to microfractures induced within the tissue leading to different scattering paths. Similarly, in reference [26], the linewidth of the random laser emission has been shown to correlate with the concentration of spermatozoa in bovine semen. In this case, the gain medium is provided by a solution of water-soluble dye laser (Rhodamine 640). The dependence of the linewidth on the spermatozoa concentration can be seen in Figure 1.7 b), showing that narrower spectra are obtained for higher cell concentration.

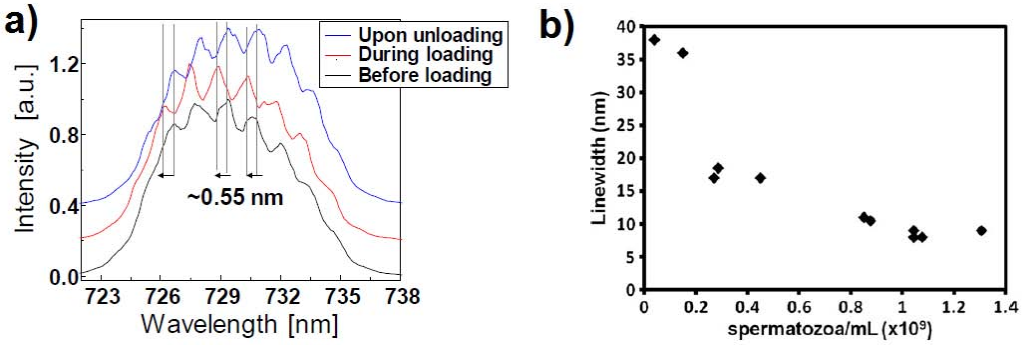

Figure 1.7. a): Spectral emission of Rhodamine infiltrated bone tissue (the figure is taken from reference [4]). b) Linewidth of random laser emission as function of cell concentration (the figure is taken from reference [26]).

Some of the variables involved in the emission features of biological random lasers are the internal ordering of the cells, which function as scattering centers in the tissue, as well as the geometry and the change in refractive index of diseased cells. In spite of the vast types of materials used to achieve random lasing and its promising potential in medical diagnosis, biological random lasers have not been fully exploited and the reports in literature are still very limited. In general, random laser action can be used in any material with strong multiple scattering effects. With this in mind, we have recently explored the

possibility of obtaining random laser emission using bovine pericardium as the scattering medium [27]. The high content of collagen fibers makes of this tissue a high scattering material in the visible region of the optical spectrum. With the infiltration of a gain medium, in our case a solution of an organic dye in glycerin, bovine pericardium is suitable for sustaining random laser action. Figure 1.8 shows some recent results with this approach.

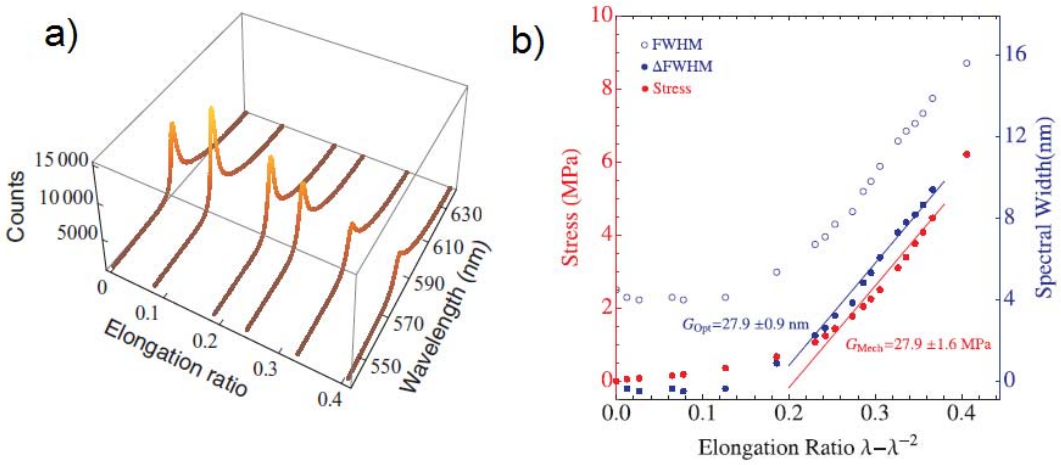

Figure 1.8. a) Random laser spectra during a bovine pericardium tensile test. b) Stress and spectral width as function of elongation ratio. The figure was adapted from reference [27].

Narrow spectra (~5nm) can be seen in Figure 1.8 a), which is one of the main characteristic of laser emission above threshold. Furthermore, we performed a uniaxial load test at the same time in order to study the effect of the deformation in the spectral features of random lasing. We found that the width of the emission correlates well with the stress-elongation ratio curve, as shown in Figure 1.8 b). As a general conclusion, these results shown that the deformation of the tissue by means of the mechanical load have a notorious effect in the random laser emission. This suggests that the microstructure of pericardium provides different optical paths while the tissue is elongated, as evidenced by the widening of the random laser emission. Furthermore, the fiber alignment of collagen fibers could be related in the dynamic behavior of random lasing showed above. These promising results have motivated deeper studies on scattering effects during tensile tests with bovine pericardium, requiring novel experimental setups to perform several optical techniques along with the mechanical test. The first step towards a better understanding of

the random laser emission on bovine pericardium is to briefly overview the composition of this tissue, and how the complex structure of fibers provides it with the adequate mechanical properties to be used as heart valve replacement.

1.3. BOVINE PERICARDIUM AS A BIOPROSTHETIC MATERIAL

1.3.1. Structure and composition

As all the important organs in the body of mammals, the heart has a protective two-layer membrane with a small volume of fluid between the layers called pericardium [28]. Pericardium is a stiff membrane that closely encloses the heart, the origins of the great arteries and the terminations of the great veins. This membrane is composed of a single layer of mesothelial cells and a fibrous outer layer. The visceral pericardium is constituted by the inner layer and is attached to the surface of the heart. Parietal pericardium consists of a smooth serosal layer; the fibrosa, which contains collagen elastin, nerves, blood vessels and lymphatics; and a rough epipericardial connective tissue [29]. Figure 1.9 illustrates the gross anatomy of pericardium and its relation with great veins.

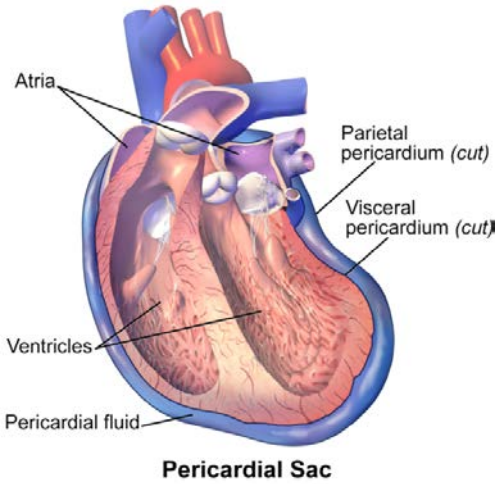

Figure 1.9. Illustration of pericardium sac and main parts of heart. The image has been taken from: http://commons.wikimedia.org/wiki/File:Blausen_0724_PericardialSac.png

As in other connective tissues, collagen is a major component of pericardium. Pericardium is predominantly homogenous in composition, comprised mainly of Type I collagen and elastin. Collagen is the most abundant protein in mammals and helps to maintain the tissue shape, dissipate loads and partition cells and tissues into functional units. Collagenous tissues consist in general of collagen fibrils embedded in an amorphous gel-like matrix of proteoglycans and water [29]. A high degree of organization from the molecular to the macroscopic level can be seen in the collagen structure. The collagen building block is a triple-helix molecule synthesized from three amino acid chains coiled into left-handed helices. The molecule itself is a 290 nm in length right-handed triple helical structure called tropocollagen. Figure 1.10 shows schematically the assembly of the three alpha chains to form procollagen.

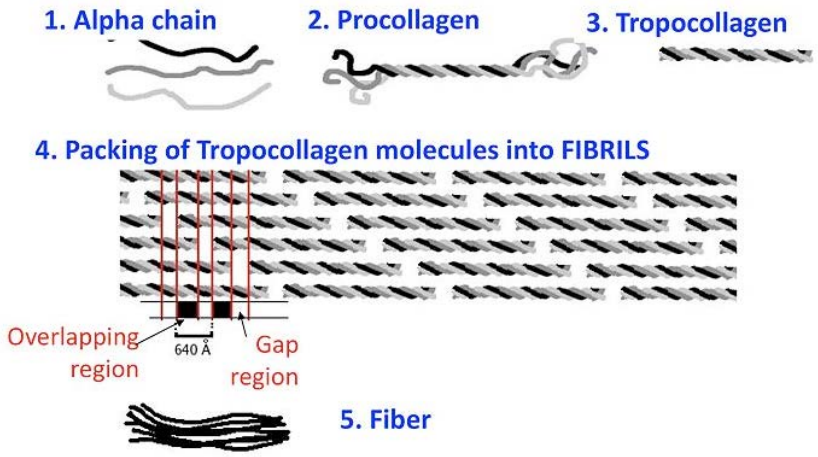

Figure 1.10. Schematic illustration of the collagen structure. The image has been taken from: http://en.wikipedia.org/wiki/Collagen#/media/File:Collagen_biosynthesis_(en).png

As it is illustrated in Figure 1.10, tropocollagen molecules pack into an ordered structure called fibril. This crystalline organization gives rise to supermolecular coiling of collagen fibers. All fibrils possess the D-periodicity, which is a period of 67-nm and corresponds to 1/4 of the total length of the collagen molecule. Figure 1.10 shows several tropocollagen molecules aggregated into a staggered parallel array. This staggering creates holes and overlap zones which when viewed under an electron microscope, manifests as light and dark bandings [30]. The fibril diameter ranges from 10 nm to 100 nm and can aggregate either by forming larger scale parallel arrays or by forming more complicated 2

or 3 dimensional super-structures. Finally, the fiber dimensions usually range from ~1 mm to several hundreds of millimeters and may aggregate in a parallel fashion leading to the macroscopic tendon or other more complex arrangements. The hierarchical structure of collagen is important because it ultimately determines the characteristic properties of pericardium as a bioprosthetic material such as tensile strength and elasticity [31,32].

1.3.2. Mechanical properties and fixation

It has been shown that bovine pericardium possesses the higher content of collagen among several pericardium species [29]. Extensive work has been carried out to determine the relation of collagen recruitment with the mechanical properties of bovine pericardium and other collagen tissues [30, 31]. Collagen fiber orientation and fiber diameter significantly influence the mechanical properties of collagenous tissues. For tissues in which the collagen fibers are totally oriented, like in tendons, the stress-elongation ratio curve is a highly linear curve; in contrast, in disordered oriented tissues such as pericardium, the stress-elongation ratio curve show a highly nonlinear behavior. Fiber direction is always indicative of prevalent tensile stresses because fiber reorientation is the most efficient and selective way to optimize strength without increasing weight and metabolic costs [29]. This explains why the pericardium is comprised mainly of Type I collagen, whose main function is to transmit loads adjusting to stresses in varied directions.

Bovine pericardium exhibits three main regions in a stress-elongation ratio curve. In the first region, the elongation ratio increases with few changes in the stress. The energy applied to the tissue is used to uncoil the collagen fibers initially in a wavy fashion [29], offering relatively little resistance to stretch. After a certain value in elongation ratio, some of the fibers start to align, and a highly nonlinear transition region appears [32]. Finally, when most of the fibers are aligned, one can distinguish a third region where a more linear curve is present. This is expected since once collagen fibers are straight; stretching them requires a much greater force. Figure 1.11 depicts the behavior of samples of bovine pericardium subjected to tensile tests.

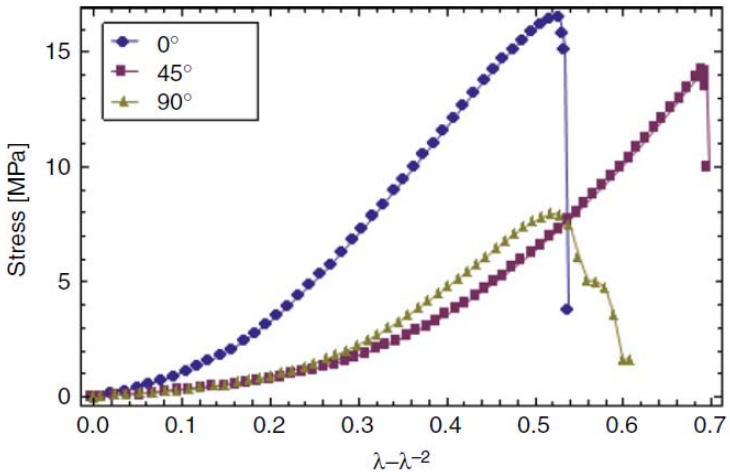

Figure 1.11. Stress-elongation ratio curves for bovine pericardium samples subjected to uniaxial load. The curves correspond to different orientation cuts of bovine pericardium samples. The horizontal axis is labeled as λ-λ^{-2} which is a measure of the deformation of the material and is known as the elongation ratio. The figure is taken from reference [32].

The sample cuts performed in reference [32] were made by determining the fiber orientation by visual inspection. Once the fiber orientation was obtained, three cuts were made. One of the samples was cut along the determined fiber orientation (labeled as 0° in Figure 1.11), other of the samples was cut perpendicular to the fiber orientation (labeled as 90° in Figure 1.11) and the last sample was cut in an oblique direction (labeled as 45° in Figure 1.11) according to the fiber orientation. It is convenient to say that although the present work also explore the behavior of samples cut in different orientations, we have adopted a more general scheme which takes the base-apex axis of the bovine pericardium as orientation reference. The base-apex axis along with the details of the sample manipulation protocol will be opportunely described in following sections.

As seen in Figure 1.11, the three curves show a nonlinear behavior varying according to the orientation at which the sample is cut. This emphasizes again the relevant role of fiber orientation in the mechanical behavior of the whole tissue. It is important to note that the samples reported in reference [32] were treated with an external agent (glutaraldehyde) in order to enhance the mechanical properties of the tissue. This treatment is known as fixation and the most common fixation procedure for collagenous tissues is based on glutaraldehyde. Glutaraldehyde fixed valves were first implanted in 1967 after it

was determined that glutaraldehyde stabilized collagenous biomaterials [33]. In general, glutaraldehyde fixation protects the tissue against enzymatic degradation, sterilizes pathogenic agents and reduces immunogenic responses. Glutaraldehyde forms complex, degradation-resistant cross-links between collagen molecules. Glutaraldehyde-preserved trileaflet bovine pericardial prostheses were first introduced in 1977 [34].

After this brief description of the fundamentals of lasers and random lasers and the basic characteristics of pericardium, we proceed to detail the experimental setup, methods and materials used in this study. We divide the study in two main sections, the experiments without gain medium in which scattering in tissue is studied and the experiments with Rhodamine 6G as gain medium in which random laser action is obtained. Both sections have different experimental setups and their own methods that will be described properly in the following chapters. Briefly, Chapter 2 deals with two techniques: Enhances Backscattering (EBS) and Müller Matrix Imaging (MMI). On the other hand, Chapter 3 and Chapter 4 focus on the spectral analysis of the random laser emission and Stokes vector imaging respectively. Then, we compare in Chapter 5 the two sets of experiments and we finally discuss in Chapter 6 the advantages and disadvantages of random laser analysis in contrast to conventional scattering techniques.

CHAPTER 2

SCATTERING CHARACTERIZATION OF BOVINE PERICARDIUM DURING TENSILE TESTS

In previous sections the basic principles of conventional and random lasers were overviewed. The structure and composition of pericardium was also described briefly. Our final goal is to obtain random laser action in bovine pericardium and study its spectral features during a tensile test. First, we study in this chapter the scattering properties of bovine pericardium prior studying random lasing in this particular tissue. This approach is based on previous results with synthetic (i.e. non-biological) random lasers [24]. In the case of random lasers based on silica particles, the study of the variables that affect the scattering medium, such as concentration and scatterer geometry, provided a better insight of the feedback mechanisms in random lasers [13]. If random lasing is generated in tissue, the tensile test is expected to change the spectral emission because the structure of the scattering medium (i.e. the tissue) is modified due to mechanical deformation. These changes in the microstructure should also be detectable with conventional optical methods. Hence, we expect that random lasing analysis could provide complementary information about the microstructure of the tissue as well as an improved resolution for analyzing ordering effects within this complex material. These expectations rely on the fact that lasers are active devices in which any perturbation gives rise to variations on the spectral features of the laser emission. In principle, these effects should be easier to detect than performing a full characterization of the angular intensity distribution in a multiple scattering experiment.

Instead of obtaining a full spatial distribution of the light scattered by a diffuse material, requiring complex and expensive techniques such as dynamic light scattering or X ray diffraction [34,35], standard optical methods were implemented in order to obtain complementary information of the biological tissue. The experimental setup used in this

work was designed to perform enhanced backscattering measurements, Müller matrix imaging and digital image correlation during the uniaxial tensile tests. Data and subsequent analysis from these experiments can thus provide information about the photon mean free path within the tissue, the polarization parameters and the viscoelastic behavior of the tissue sample. The information recorded in the experiments shown in this chapter will be useful to compare the results of random laser tests and determine the potential application of random lasers to tissue characterization.

2.1. SAMPLE PREPARATION

Sample preparation is a very important step in any experimental study of complex materials such as tissue. Standardized and careful preparation benefits results validation because samples are manipulated following the same protocol each time before a test is performed. In general, sample preparation refers to all the processes undergone by a sample before its analysis. For the experiments reported in this work, bovine pericardiums from 18-month calves were collected fresh from local slaughterhouse. Certification of the slaughterhouse is not a requirement at this stage of the research because human implantation is beyond the scope of this study. Nevertheless, we followed a sample preparation protocol similar to those used in actual medical applications where a chemical agent is used to preserve and crosslink the tissue [33]. Table 2.1 summarizes the protocol used in these experiments and a description of each step is exposed in what follows.

Bovine death.	t=0
PBS washing.	t<1hr
GA fixing (PBS+ 0.5%GA).	t<4hr
Sample cutting.	t<1 day
Glycerin immersing	t<2 days
Optomechanical tests.	t<2.5 days
Material disposal.	t<3 days

Table 2.1. Sample preparation protocol from the death of the animal to the material disposal.

The pericardium sac was washed in cold saline solution and fat and excess tissues

were removed from the tissue within the following hour after the death of the bovine. Subsequently, the whole sac was allocated in a custom-built frame to be cross-linked with glutaraldehyde. The fixation process was carried out during 24 hours at 4°C, using 0.5% glutaraldehyde in 0.1 M phosphate buffered saline solution with a pH of 7.4; this is a common procedure for fixing bovine pericardium [31, 33]. The custom-built frame allows for the complete sac to undergo the fixing process while mimicking its native disposition. Figure 2.1 shows a photograph of the custom-built frame with a bovine pericardium sac.

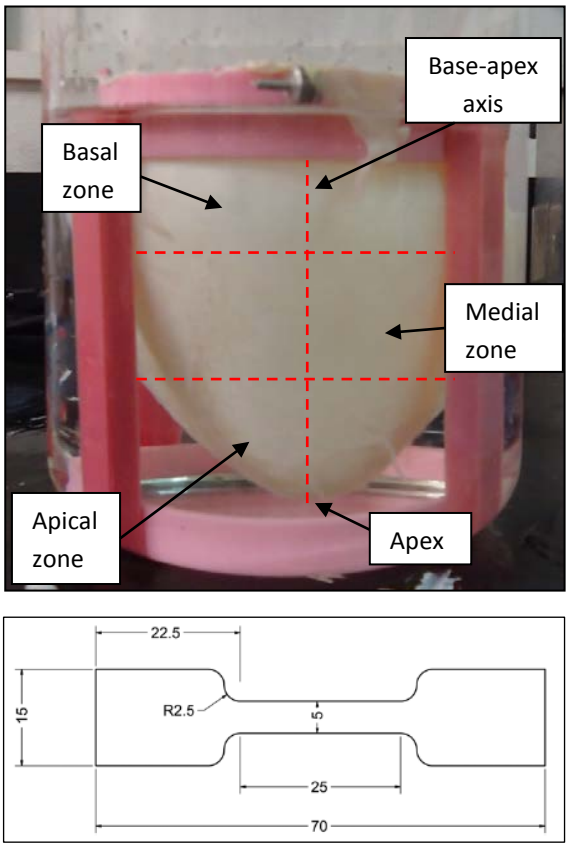

Figure 2.1. Photograph of the custom-built frame with a bovine pericardium. The vertical dashed line show the base-apex axis. The two horizontal dashed lines indicate the delimitation for the apical, medial and basal zones. The image at the bottom shows the dimensions in millimeters of the dog bone shape used to cut the pericardium samples.

As figure 2.1 shows, the tissue is suspended by its upper section and is immersed in a similar fashion to its natural disposition inside the bovine body. After the fixation process, the sacs were washed in distilled water and subsequently cut with a special jig to

obtain samples with a dog bone shape, a standard for tensile tests. In total, 4 samples were cut with the same dog bone geometry in order to perform the scattering experiments described in this chapter. Two of them were cut near the apex (apical zone, see Figure 2.1) while the rest were cut at the central part of the pericardium (medial zone shown in Figure 2.1). One of the apical samples was cut along the apex axis (apex-base axis), while the other apical sample was cut following the perpendicular direction of the apex axis; the same was done for the medial samples. It is important to note that no samples were cut in the basal zone. This was done for convenience as basal zone is the closest zone to the initial cut. In the basal zone the fiber orientation is not representative of the medial zone and thus the fiber and density of the fibers are not the same, the base zone of the pericardium was discarded. Next, samples for the scattering experiments were immersed in a solution of glycerin in order to minimize sample deterioration and to maintain the samples moisten during the test. All tests were carried out during a time lapse of two hours approximately. Finally, the tissue samples were disposed before 72 hours after the death of the bovine.

During sample preparation, small inner cuts of the tissue were set apart before and after the fixation process as well as after immersion in glycerin. These samples were dehydrated by washing in alcohol-water solutions with proportions of: 10:90, 25:75, 50:50, 75:25, 90:10 and 100:0. Then, the samples were dried by heating at 60°C during 8 hours. Dehydration-drying is a typical scanning electron microscope (SEM) sample preparation for collagen based tissue [36]. The samples were observed in a SEM to account for changes in the apparent tissue structure during sample preparation.

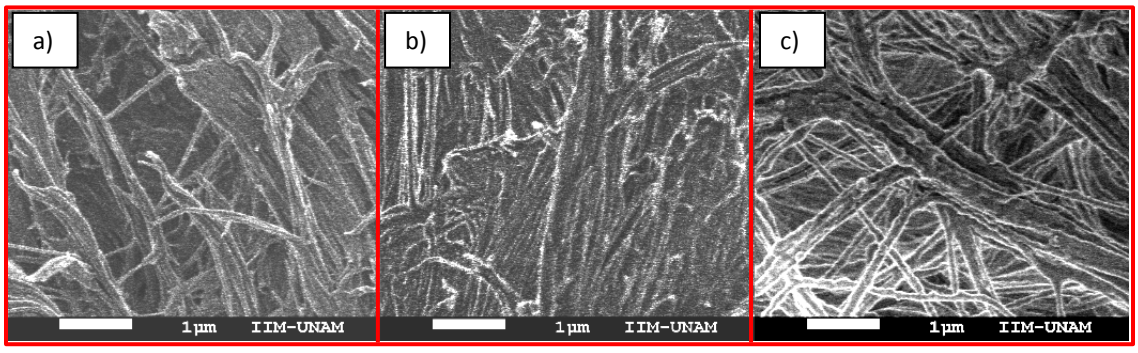

Figure 2.2. SEM images of the bovine pericardium from different stages of the sample preparation protocol. a) Bovine pericardium before fixation. b) Bovine pericardium after fixation. c) Bovine

pericardium after fixation with glycerin.

Figure 2.2 shows representative SEM images of the tissue samples obtained under the same settings for the microscope. The diameters of the collagen fibers in the three images are in the order of 100 nm. Figure 2.2b (after fixation) shows a more compact fiber arrangement than Figure 2.2a, which correspond to the tissue without fixation. This is expected since the fixation process using glutaraldehyde promotes fiber adhesion by chemically bonding collagen molecules [37,38]. Finally, Figure 2.2c shows a dense packed fiber structure similar to that observed in Figure 2.12; notice however that a layer of glycerin on the collagen is observed as wavy features covering the fibers. This indicates that the glycerin solution can impregnate the inner fibers after 24 hrs. of immersion. It is important to note that although images from Figure 2.12a and 2.12b show a preferred orientation of the fibers, Figure 2.12c shows a random fiber orientation. Random orientation of collagen fibers is the general case for bovine pericardium [17, 37]. This protocol has proved to be useful to enhance the mechanical properties of pericardium through fixation with glutaraldehyde [37]. Furthermore, it is also appropriate for optical and mechanical tests as glycerin prevents tissue drying during the tensile test and is a good solvent for organic dyes such as Rhodamine 6G [39].

2.2. EXPERIMENTAL SETUP

One of the key features in correlating mechanical and optical parameters is an adequate experimental setup allowing simultaneous mechanical and optical tests. A mechanical testing device for thin and elastic samples is required to induce stress to the sample. Based on previous reports, uniaxial tensile test was selected as an adequate scheme for mechanical testing the pericardium samples [19, 26, 31]. An optical system comprising lenses, CCD cameras and filters is also needed to visualize the sample as it is subjected to uniaxial tension. The mechanical tester along with the optical system used in these experiments will be described in detail shortly. In order to automatically control the mechanical and optical tests a Virtual Instrument was written in *LabVIEW*. Figure 2.3 shows a general block diagram for the main components of the experimental setup.

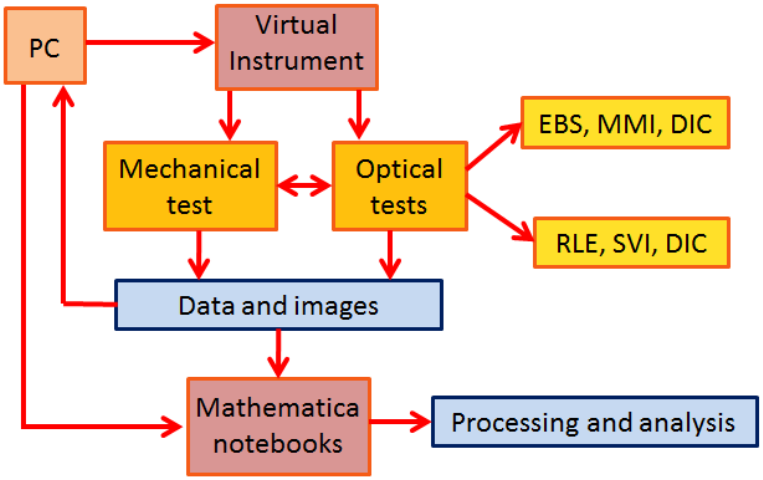

Figure 2.3. Block diagram overviewing the setup, data acquisition and analysis of the experiments with bovine pericardium. The optical tests comprise two set of tests: enhanced backscattering (EBS), Müller matrix imaging (MMI) and digital image correlation are set for the scattering characterization of the samples (chapter2). The spectral analysis of Random laser emission (RLE), Stokes vector imaging (SVI) and DIC are performed for the set of experiments in which the organic dye (R6G) is added.

The Virtual Instrument is manipulated from a conventional PC where data and images from mechanical and optical tests are recorded. Relevant parameters during the mechanical test are the induced force and the displacement of the sample; these parameters allow constructing the stress-elongation ratio curve. On the other hand, several optical techniques such as enhanced backscattering, Stokes vector imaging or digital image correlation were incorporated to the experimental setup. Processing and analysis of the data acquired was carried out by means of *Mathematica* notebooks specifically written for these experiments.

2.2.1. Load frame

The mechanical testing device used in our experiments is based on a load frame designed to apply uniaxial load on soft and thin materials. Relevant parameters for this test, such as the force load and displacement are monitored via electronic sensors. Data acquisition as well as synchronization of the electronic and optical devices is conveniently

carried out with *LabVIEW* as will be detailed in a subsequent section. The load frame of the apparatus was built using stainless steel bars supporting the axial load system composed by two rectangular cross-heads. A mechanical actuator is fixed to the upper cross-head of the frame, and a force sensor is coupled to the end of the actuator. As depicted in Figure 2.4, the load frame is held together by a rectangular stainless steel beam, which also serves for housing the displacement sensor (a linear variable differential transformer, LVDT) and its corresponding reference device for calibration.

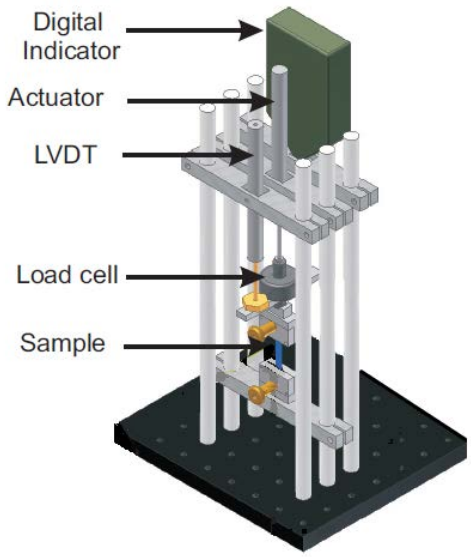

Figure 2.4. Schematic representation of the load frame. The actuator allows moving the upper grip in the vertical direction while the LVDT and the load cell register position and force, respectively.

The tissue samples are held using a special set of grips specifically designed to avoid damage and slip during the tensile test. The mechanical actuator used in the load frame is a T-LA28A Zaber with a linear displacement range of 28 mm and providing up to 10 N of loading force. A stepper motor is used to control the actuator allowing for linear displacements of 304.8 µm per revolution and 0.01 µm per microstep. With this arrangement, displacements can be controlled with an accuracy of ± 12µm. A precision miniature load cell, model 31 from Honeywell Sensotec, is used to measure the axial load during the tensile tests. Tension and compression load forces (± 9.81 N range, 0.15 %–0.25 % accuracy) are registered with this device, which also compensates for off-axis loading effects thus minimizing the shear force components. This feature avoids shear

stress contributions to the measurements, which would modify the general state of stress of the sample during the test [40]. Displacement of the linear actuator during the tests is measured by means of a LVDT, model MHR1000, from Lucas Schaevits. Calibration curves for the force registered in the load cell and the displacements measured with the LVDT are provided in Appendix A. Data acquisition and control is performed with a National Instruments NI-USB 6009 data acquisition board, used to register time, displacement, and force data during the tensile tests. The load frame was mounted over an optical table (*Thorlabs*) in order to couple the mechanical test with the optical techniques described below [19, 26].

2.2.2. Illumination and optics

In general, the optical techniques described in this section are optically passive (i.e., an active medium is not used) and consist in shining a light beam on a sample and detect the portion of light interacting with the sample. As we will see next, for some detection methods the characteristics of the illumination beam, such as polarization and intensity, are important or even crucial. The illumination scheme for these experiments comprises a pulsed laser and a mercury white lamp. To obtain proper illumination for enhanced backscattering measurements and Müller matrix imaging, a Nd:YAG pulsed laser (New Wave Solo I, 532 nm wavelength) was used as light source. This equipment can deliver up to 11.25 mJ per pulse with a nominal pulse width of 6-10 ns. A table of the pulse energy for some settings on the console indicator is included in Appendix B.

The spot of the pump laser had a diameter of approximately 0.5 cm and was oriented to illuminate the central region of the tissue sample trough a mirror and a beam splitter, as Figure 2.5 shows schematically. The mirror was a silver coated mirror from *Thorlabs* covering the visible spectrum with 99% of reflectivity, whereas the beam splitter (50:50 ratio) allows shining the laser light to the sample at the same time that the enhanced backscattering cone is registered. A quartz halogen lamp (Fiber-Lite DC950, Dolan-Jenner) was used as the illumination source to record images for subsequent processing

through digital image correlation. The white lamp used in the setup is coupled to an optical fiber bundle and attached to the optical system via a beam splitter, as depicted in Figure 2.5. Additionally, the white lamp allows low noise illumination (~21 dB) and permits remote control that can be incorporated into a *LabVIEW* virtual instrument.

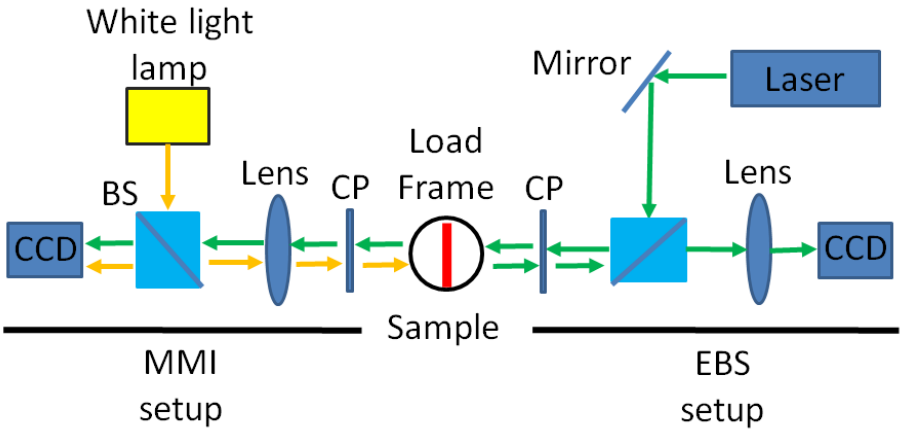

Figure 2.5. Schematic representation of the experimental setup. Laser illumination is shown as green arrows. White light illumination is represented by yellow arrows. BS: beam splitter, CP: circular polarizer. MMI: Müller matrix imaging, EBS: Enhanced Backscattering.

As Figure 2.5 shows, two different imaging setups were coupled to the load frame. While Müller matrix imaging and white light images were registered with one camera (MMI in Figure 2.5), a second camera recorded the back-reflected light for acquiring enhanced backscattering images. The Müller matrix imaging setup comprises a Pixelink USB CCD camera with a C-mount, a Mitutoyo objective (5X), and an *InfiniTube* assembly to couple the microscope system. The *InfiniTube* assembly unit further allows for placing filter holders and a beam splitter within the optical axis of the microscope. Enhanced backscattering measurements were performed with a 5X Mitutoyo achromatic objective and a CCD camera placed at the other side of the sample (EBS in Figure 2.5). The objective and the camera sensor are separated a distance of 43 mm matching the focal length of the objective. This allows for mapping the intensity registered onto each pixel to a corresponding ray backscattered at angle θ from the sample [41].

Two circular polarizers were used in the setup: one to generate different states of polarization and the remaining one to analyze the output beam. Both polarizers were assembled upon combining a linear polarizer and a quarter wave plate with an angle of 45° between their optical axes [42]. The linear polarizers and quarter wave plates were models LPVISE100-A and WPQ10M-532, respectively, both from *Thorlabs*. The calibration curves for the polarizers and wave plates were constructed by recording the intensity as a function of the rotation angle; these are shown in Appendix C.

2.2.3. Relaxation time

In fibrous tissues, relaxation occurs when an external force is applied and the fibers within the tissue reorder in such a way that the total stress is minimized [43, 44]. This is possible because collagenous fibers can adopt a wavy pattern when no deformation is present and tend to uncrimp depending on the magnitude of the deformation [28-30]. The characteristic time in which tissue stops the fiber rearrangement after a force is applied depends mainly on the content and orientation of collagen fibers [28]. Nevertheless we can estimate the order of magnitude of such a parameter by probing several samples. Force and time data can be used to study relaxation effects in bovine pericardium; these measurements can also provide evidence of the shortest time needed to wait for the fibers to rearrange when a fixed deformation is applied. Using the load frame described in the previous sections, a fixed uniaxial deformation was applied to the bovine pericardium samples. Once the elongation was applied, the force in the load cell was registered in steps of 0.5 seconds during 1 minute. Figure 2.6 shows some of the results of these preliminary experiments.

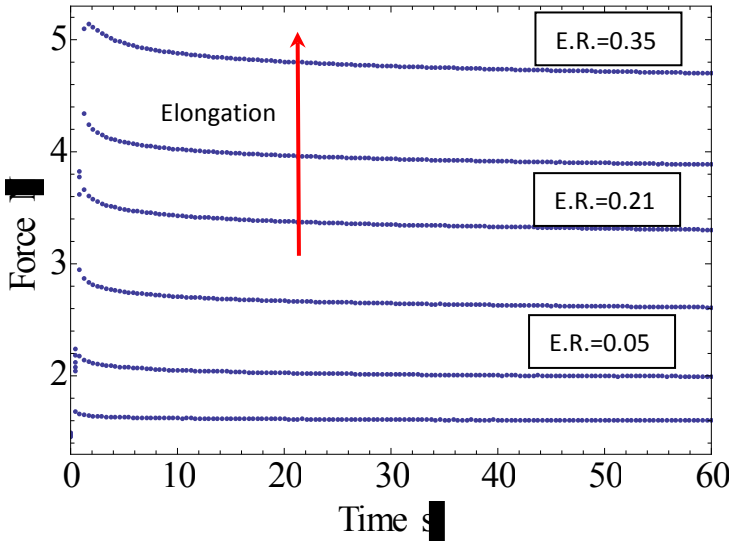

Figure 2.6. Relaxation curves for different elongation ratios (E.R.). The curves with higher force correspond to longer elongation ratios. As can be seen from the curves, the most significant changes occur during the first 30 seconds.

Each curve in Figure 2.6 corresponds to a fixed elongation applied to the same pericardium sample and illustrates the relaxation process registered with the load cell. At first, short elongations in the sample were applied and a 5 minutes waiting period was set between loadings. In all cases, the curves show an exponential decay in time. For the more elongated tests we observed a longer relaxation time. Despite this behavior, the relaxation time was shorter than 30 seconds for all tests in this preliminary stage. Due to the dependence on different samples and fiber orientation, a waiting period of at least 2 minutes was set as a standard for acquiring any optical measurements in subsequent experiments.

2.2.4. Virtual Instrument

Automatic control of experimental devices such as sensors, actuators and cameras allow executing highly repeatable tests. Moreover, when using pulsed lasers as illumination source of images, timing and synchronization become critical. With the exception of the circular polarizers, a custom designed computer program automatically

controlled all the devices used in these experiments. *LabVIEW* was used to control the experimental setup to record the measurements and images of the tests via a commercial PC. Several Virtual Instruments were developed following a sequential linear programming approach, in which each of them acts as a single module that can be incorporated to subsequent modules. Each module was programmed and tested individually as well as after joining with the other modules thus forming the final Virtual Instrument controlling the complete experiment. This approach allowed programming specific tasks at a time and further generates less processor jitter dependency in the final Virtual Instrument. Low level triggering was used to control synchronization between the laser pulses and image acquisition. Figure 2.7 shows the flow diagram summarizing the sequence controlled by the Virtual Instrument.

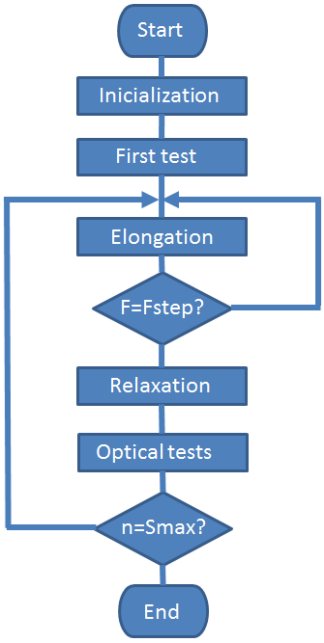

Figure 2.7. Flow diagram of the Virtual Instrument (VI) used in the experiments. The program was developed in LabVIEW following a sequential linear programming approach in which each stage is tested as a single VI.

In the initialization process all the devices are initialized and set in stand-by mode. The variables of the test such as microstep elongation length, number of steps, and number of pulses per polarizer position are defined in this stage. Then, the optical tests (enhanced backscattering and Müller matrix imaging, both described in subsequent sections) are

performed with no deformation in the sample; this provides the appropriate reference when no load is applied. After this first test, the actuator elongates the sample with a microstep elongation defined typically as 20 μm.

The load cell registers the applied force and the elongation is repeated until the registered force is higher than the one defined before for this test cycle (F_{step}). When this value is reached, the load frame maintains the position of the actuator fixed and waits a period of time larger than the relaxation time found in the section 2.2.3. This holding time can be set by the user before the test and the typical value for these experiments is 2 minutes. Once the holding time has passed, the enhanced backscattering and Müller matrix imaging are performed. Once this is done, a test cycle is finally concluded. The number of test cycles is also set at the beginning of the test and 6 or 7 cycles were typically carried out in these experiments. If the number of cycles has not been completed, the Virtual Instrument starts the elongation again in order to probe the sample at higher deformations. Finally, when the number of cycles is reached the test finishes, all data is then summarized and the Virtual Instrument releases the devices from its stand-by mode.

2.2.5. Image and data analysis

The virtual instrument described in the previous section acquires force, position and time data during the tensile test. Additionally, the virtual instrument records several images corresponding to each of the 16 positions for the circular polarizers, with both, white light and laser illumination for DIC and enhanced backscattering images, respectively. Adequate processing is needed in order to obtain useful information from all acquired data. Figure 2.8 shows schematically the way in which data from the tensile test is handled. In general, all post-processing was done using notebooks written in *Mathematica*.

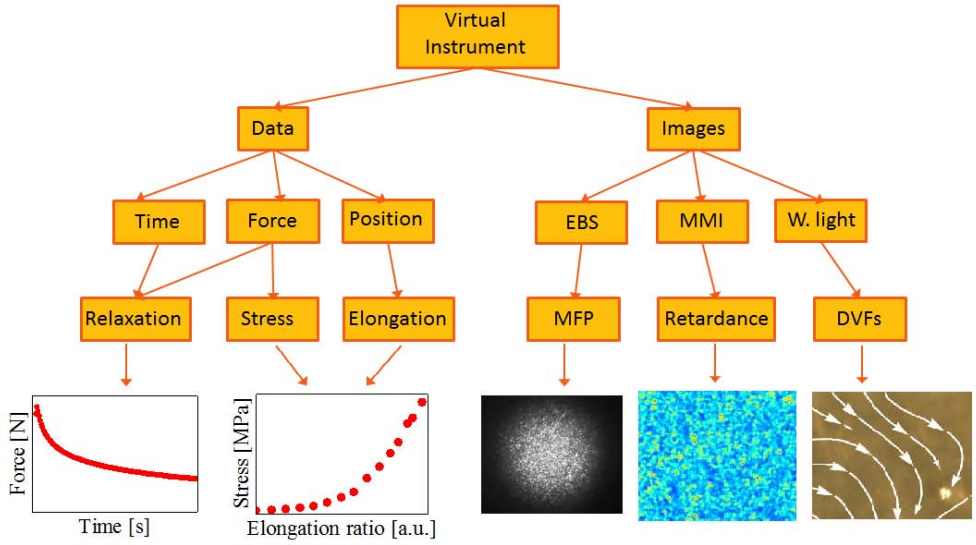

Figure 2.8. Block diagram of data acquisition and processing. The images acquired by the VI are for enhanced backscattering (EBS), Müller matrix imaging (MMI) and white light illumination. Subsequent data processing provides the mean free path (MFP), retardance and the displacement vector fields for the tissue sample.

Images recorded with white light illumination were used to obtain displacement vector fields. As described later, by correlating two consecutive images we are able to obtain the displacement along the image area. Displacement vector fields in bovine pericardium during tensile tests have shown to be useful to give information at the micrometric scale [31]. In our case, these vector fields will be compared with the retardance images, which give information about the birefringence of the sample [45]. The retardance images are obtained by means of Müller matrix imaging based on a 16x16x pixel matrix system constructed with the images obtained with laser illumination. Similarly, enhanced backscattering (EBS) images are analyzed in order to obtain the mean free path, which correspond to the mean distance between scattering events and is a measure of the optical turbidity of the sample [41, 46, 47]. The analysis of EBS images is described in the corresponding section; EBS provides information about the scattering ensemble and is sensitive to small changes in the concentration of scatterers within the sample [41, 46]. Since the mean free path is a representative measure of the whole scattering ensemble (i.e., collagen fibers), these measurements can be compared with the

stress-elongation ratio curve, which is also an average measure of the behavior of the fibers [48] during the tensile tests.

Using the force and position data recorded by the Virtual Instrument, the stress-elongation ratio curve can be readily constructed, as described in the following sections. This curve gives information about the macromechanical of the sample such as alignment and viscoelastic properties. Stress-elongation ratio curve is a standard in characterization of soft thin tissue because they reveal the elastic nature of such materials [48]. Comparison of the stress-elongation ratio curve with the mean free path during the tensile test is an important feature of this work, because relating an optical non-invasive technique such as enhanced backscattering with a standard mechanical test could lead to new characterization methods of soft tissue.

2.3. RESULTS AND DISCUSSION

2.3.1. Macromechanical behavior

The stress on the sample during the test was obtained with the force measurement registered by the load cell and the transversal area of the sample (i.e. perpendicular to the force applied). While the force was recorded with the Virtual Instrument, the transversal area was considered to be constant during the test. The deformation of the samples is described in terms of the elongation ratio as:

$$\text{Elongation Ratio} = \lambda - \lambda^{-2} \qquad 2.1$$

With:

$$\lambda = \varepsilon + 1 \qquad 2.2$$

Where ε is the engineering strain. The stress-elongation ratio curves for different bovine pericardium samples under uniaxial tension are presented in Figure 2.9.

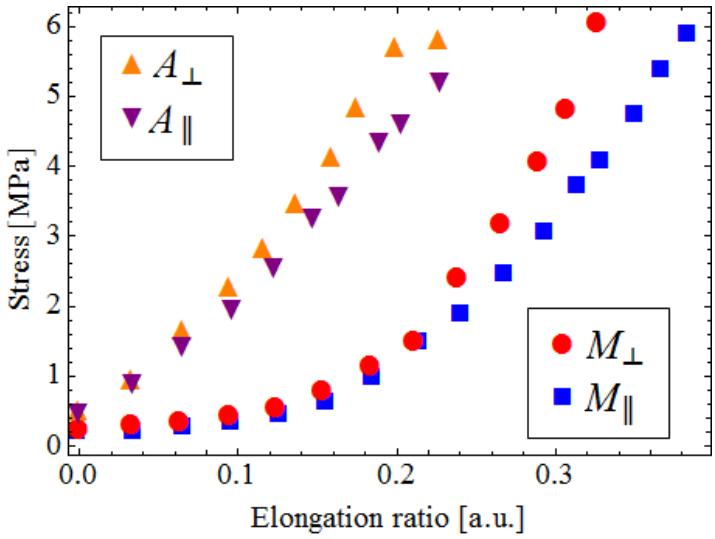

Figure 2.9. Stress-elongation ratio curves obtained for 4 different bovine pericardium samples. $A_\perp$: Apical sample cut perpendicular to the apex axis; $A_\parallel$: Apical sample cut in the direction of apex axis; $M_\perp$: Medial sample cut perpendicular to the apex axis; $M_\parallel$: Medial sample cut in the direction of apex axis (see Fig. 2.1 for location within the pericardium sac).

Figure 2.9 shows different stress-elongation ratio curves corresponding to four different samples tested in these experiments. The samples correspond in turn to different cuts from the pericardium sac; the curve of the medial sample cut perpendicular to the apex axis ($M_\perp$) is marked with red circles, blue squares represent the curve for the medial sample cut along the apex axis ($M_\parallel$), the curve of the apical sample cut perpendicular to the apex axis ($A_\perp$) is represented with orange triangles and inverted purple triangles plots the corresponding curve of apical sample cut parallel to the apex axis ($A_\parallel$). Although the samples were cut either parallel or perpendicular to the apex axis, the collagen fibers within the tissue are, in general, randomly oriented [17, 37]. This means that the orientation in which the samples were cut does not necessary correlate with a dominant orientation of the collagen fibers with respect to the longitudinal axis of the tensile sample. The most notorious change in the trends of the curves is that of the apical and medial samples. Apical samples needed more force to be elongated by the same ratio than the medial samples. This is expected as fiber concentration increases in the apical zone and higher fiber content results in a higher resistance to loading [49].

Another interesting feature observed in Figure 2.9 is that a non-linear behavior is more evident for the medial samples, while apical samples show a more linear tendency. The non-linear behavior has been widely reported in literature [49]. Nonetheless, apical samples are not reported frequently because the apical zone is avoided when cutting pericardium valves [33]. However, we study both zones as our goal is to relate the microstructure of the tissue with the results obtained from the optomechanical tests. Three main regions have been identified during tensile tests of collagen based tissue [31]. In the first region fibers are recruited from its wavy conformation and low loads are necessary to generate large deformations; after a certain threshold some fibers start aligning and a transition region is observed before a third region occurs when most of the fibers are aligned and a more linear behavior appears [31].

A slighter change is observed between perpendicular and parallel samples in Figure 2.9, where perpendicular samples exhibit higher stress for the same elongation ratio than the parallel samples. Such a different behavior between perpendicular and parallel samples is more evident for the samples cut in the medial zone. This implies that a less wavy conformation of individual fibers and a more disordered orientation of collagen fiber ensemble may be found in the apical zone than in the medial zone. Notice that all the samples used for the experimental results shown in Figure 2.9, were taken from the same pericardium sac, albeit being cut along different directions. This allows for a comparison between the different pericardium zones thus avoiding variations among several sacs specimens.

2.3.2. Enhanced backscattering measurements

According to enhanced backscattering theory, when light interacts with multiple scattering media a twofold enhancement in the intensity with respect to the intensity predicted by diffusion approximation appears in the exact backward direction. The factor of two arises from photons going over time-reversed paths, which constructively interfere in the direction of backscattering [46]. These time-reversed paths are schematically

represented in Figure 2.10a. Out from the exact backscattering direction, the enhancement decreases inversely proportional to the mean free path, forming an angular distribution intensity that decays to the value predicted by diffusion theory. For non-absorbing media, the intensity α near the backscattering direction as a function of the solid angle θ is given by [47]:

$$\alpha(\theta) = \frac{3}{8\pi}\left[1 + \frac{2z_0}{l} + \frac{1}{(1+ql)^2}\left(1 + \frac{1-e^{-2qz_0}}{ql}\right)\right] \qquad 2.3$$

In the above expression, $q=2\pi\theta/\lambda$, l is the photon mean free path and z_0 is given by the boundary conditions and in a plane geometry $z_0 \sim 0.7l$ [47]. Equation 2.3 shows that once the boundary conditions and wavelength λ are fixed, the shape of the enhanced backscattering cone is fully described by the mean free path, which in turn is a measure of the turbidity of the sample. This allows for obtaining an experimental measurement of the mean free path of a sample by studying the width of the angular distribution of the backscattered intensity. In this study, the enhanced backscattering images were recorded by means of the experimental setup described in the previous sections. A beam splitter is used to illuminate the sample at the same time that a CCD camera is recording the backscattering intensity. A circular polarizer is placed in front of the sample to filter single scattering events that do not contribute to the enhanced backscattering cone. Single scattering paths do not contribute with the EBS cone because time-reverse paths are not defined for these cases (see Figure 2.10a). Synchronization between the pulsed laser and the CCD was handled by the Virtual Instrument, and the recorded images were subsequently processed to obtain a normalized intensity in a gray scale. The intensity recorded in each pixel of the CCD was mapped to the scattering angle θ by taking into account the pixel width and the focal length as in [41]. Then, a fitting to Equation 2.3 was used to calculate the mean free path in terms of the wavelength. Figure 2.10b shows a representative experimental enhanced backscattering cone along with its fitting curve.

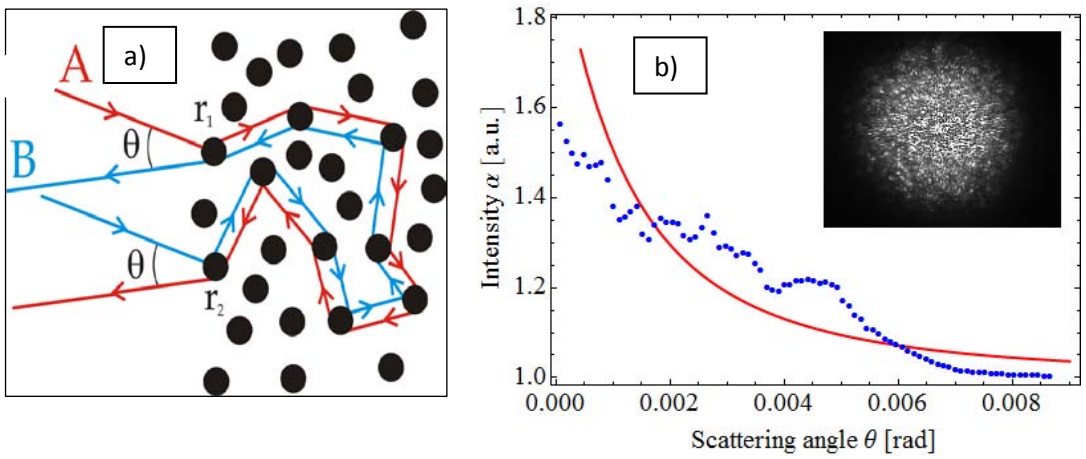

Figure 2.10. a) Schematic representation of time-reverse paths in a multiple scattering medium. b) Experimental enhanced backscattering curve (blue points) and Equation 2.5 fitting (red solid line). The inset shows an actual image of enhanced backscattering as recorded by the CCD camera.

The inset of Figure 2.10b is the actual image of the enhanced backscattering cone taken with the CCD camera. Equation 2.3 implies that the enhanced backscattering cone becomes wider as the mean free path decreases. The enhanced backscattering cone is usually normalized to the intensity given by diffuse theory; this is the first term in Equation 2.3. With this normalization, the highest value of the intensity is 2, as the lasts terms in Equation 2.3 tends to $3/8\pi$ when $q=0$ (i.e. the exact backscattering direction). Nevertheless, it has been shown that finite thickness of the sample, finite size of the illumination area, and optical absorption causes a decrease in the twofold factor lowering it to experimental values of 1.8-1.4 [50, 51]. The mean free path measured in several steps during the tensile test for different pericardium samples are plotted in Figure 2.11. Solid lines in Figure 2.11 are merely a guide to the eye.

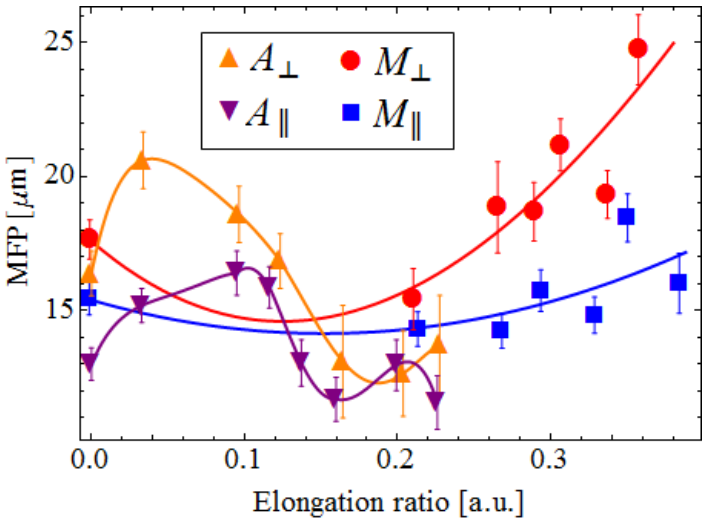

Figure 2.11. Mean free path as function of elongation ratio for the 4 different samples tested. $A^{\perp}$: Apical sample cut perpendicular to the apex axis; $A_{\parallel}$: Apical sample cut in the direction of apex axis. $M^{\perp}$: Medial sample cut perpendicular to the apex axis; $M_{\parallel}$: Medial sample cut in the direction of apex axis. Solid lines are merely a guide to the eye.

Labeling in Figure 2.11 is the same as that in Figure 2.10; "*A*" stand for apical samples, "*M*" for medial samples, the symbol $\perp$ correspond to samples cut perpendicular to the apex axis and the symbol $\parallel$ correspond to the samples cut along the apex axis. Figure 2.11 show a notorious difference between the behavior in mean free path of samples cut in the apical and in the medial zone. The difference between apical and medial curves is more evident than the difference observed in Figure 2.9, where the characteristic feature of apical samples was a more linear behavior in the first part of the test. As Figure 2.11 shows, mean free path exhibits a maximum during the test for the apical samples. In contrast, a minimum in mean free path is observed for the medial samples of Figure 2.11. In order to contrast these results with the mechanical measurements of the test, the resulting stress and mean free path are plotted together and shown in Figure 2.12.

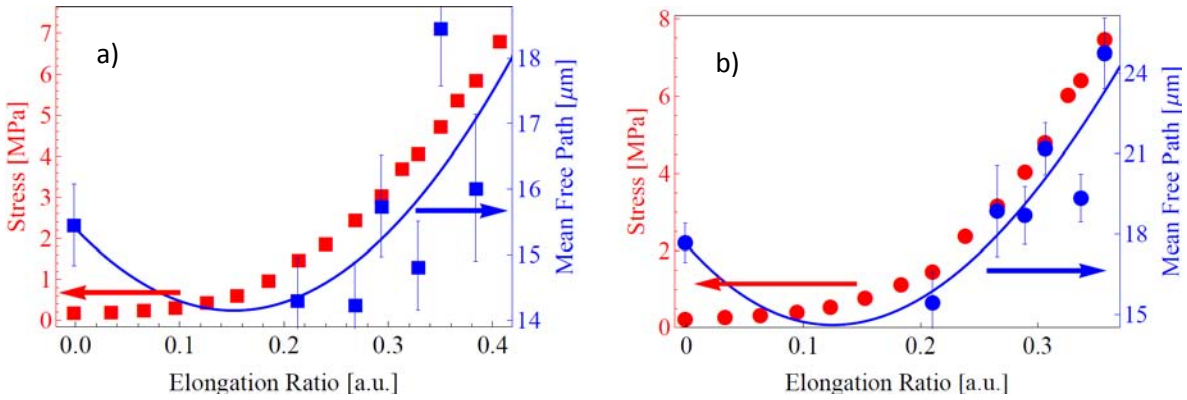

Figure 2.12. Mean free path and stress as a function of elongation ratio for medial samples cut along the apex axis $M_{\parallel}$ (a), and perpendicular to the apex axis $M^{\perp}$ (b). Solid blue lines correspond to the polynomial fitting of experimental data. In both curves, the right axis corresponds to the mean free path and was set to match the stress values registered during the test.

Figure 2.12 shows that the mean free path of medial samples behaves in a similar fashion as their corresponding fitting lines (solid blue lines). Notice also that these have a slope comparable to that of the stress-elongation curve. It is also clear from Figure 2.12 that the optical and mechanical slopes are similar only for the linear region of the stress-elongation curve. In other words, the correlation of the mean free path and the mechanical stress is more evident when the fibers are uncrimped and alignment takes places. In general, the mean free path for medial samples exhibits a tendency to increase as the elongation ratio increases. This has been previously reported and has been related to a change in scatterer concentration within the tissue [19]. Uniaxial tension in fibrous tissue tends to align the collagen fibers along the tension axis. This in turn can increase the number of scatterers per unit volume by increasing the fiber packing. In general, as the scatterer concentration increases, the scattering events per photons path (i.e. the total walk of the photons inside the material) also increases leading to longer residence times of photons inside the random material. Nevertheless, it has been shown that this behavior is maintained until a certain saturated concentration is reached [22]. This saturated concentration depends on the wavelength and the geometry of the scatterers. When this scatterer concentration is reached, the scattering force is high enough to reduce drastically the penetration component of photon paths leading to a more superficial penetration and shorter mean free paths. This matches with the higher fiber concentrations in apical

samples discussed above and shown in Figure 2.9 as a higher resistance to load in the stress-elongation ratio curves. More abrupt changes are observed in the fitting curves for apical samples, while the medial samples are associated to smoother fitting curves. This therefore provides clear evidence that optical methods such as enhanced backscattering are sensitive to microstructural changes in tissue.

2.3.3. Müller matrix imaging

A Müller matrix represents the polarization properties of a material by means of a 4x4 array [42]. This can be seen as the transformation operator between two polarization states in the Stokes vector space. In other words, the incident Stokes vector to an optical device is related to the output vector by a 4x4 matrix called the Müller matrix of the device, i.e.:

$$\mathbf{S}_{out} = \mathbf{M}\mathbf{S}_{in} \qquad 2.4$$

Here $\mathbf{S}_{in}$ and $\mathbf{S}_{out}$ represent the polarization states of a monochromatic wave before and after the interaction with the device of Müller matrix $\mathbf{M}$. Vectors $\mathbf{S}_{in}$ and $\mathbf{S}_{out}$ contain the Stokes parameters for each polarization state. It is common in literature to find a normalize Stokes vectors in which the Stokes vector is divided by the total intensity I letting the parameters to be independent of intensity.

Although Müller calculus is a well-established technique for homogeneous transparent media, when dealing with inhomogeneous materials such as tissue, the elements of the experimental Müller matrix can mislead to non-physical results. A method to model scattering, depolarization and inhomogeneity in the material is needed to extract the physical parameters from the experimental Müller matrix. Basically, two methods are used in literature aiming at solving this difficulty: the so-called polar decomposition [52], and the differential matrix formalism [53]. We have chosen the extension of the differential matrix formalism for depolarizing anisotropic media as described in [54].

The differential matrix formalism describes the media under study as transversally homogeneous but longitudinally inhomogeneous, in which the spatial derivative of the Müller matrix along the propagation axis obeys the following relation [54]:

$$\frac{d\mathbf{M}(z)}{dz} = \mathbf{m}\mathbf{M}(z) \qquad 2.5$$

Where $\mathbf{M}(z)$ is the position dependent Müller matrix and $\mathbf{m}$ is the so-called differential matrix. Equation 2.5 implies that the optical effect caused by the material scales with sample thickness. For the boundary condition $\mathbf{M}(z=0)=\mathbf{I}$, where $\mathbf{I}$ is the identity matrix, the solution of Equation 2.5 has the form $\mathbf{M}=\exp(d\mathbf{m})$, in which d is the path traveled by the light. The mean values of the elementary properties and their uncertainties can be obtained by decomposing the logarithm matrix ($\mathbf{L}=\ln\mathbf{M}$) into the sum of the G-antisymmetric ($\mathbf{L}_m$) and G-symmetric ($\mathbf{L}_u$) components according to:

$$\mathbf{L}_m = \frac{1}{2}\left(\mathbf{L} - \mathbf{G}\mathbf{L}^T\mathbf{G}\right) \qquad 2.6$$

$$\mathbf{L}_u = \frac{1}{2}\left(\mathbf{L} + \mathbf{G}\mathbf{L}^T\mathbf{G}\right) \qquad 2.7$$

Here, $\mathbf{G}=\mathrm{diag}(1,-1,-1,-1)$ is the Minkowski metric tensor. In general, the experimental Müller matrices can be non-diagonalizable, and one is forced to use a decomposition method such as Jordan decomposition in order to calculate the logarithm matrix by having a set of diagonalizable matrices.

We start the polarization study by obtaining the Müller matrices of the beam splitter and *Infinitube* system described in the experimental setup section. These were obtained using the circular polarizers described in the experimental setup section. Briefly, we have shone the element under test (i.e. tissue samples) with the pulsed laser and we captured the light with a CCD camera. Before the light interacts with the device, the beam goes through the circular polarizer that allows obtaining a known polarization state. After the beam interacts with the device, an analyzing circular polarizer is allocated in front of the CCD

camera; this in turn allows knowing the intensity recorded in the CCD camera as a function of the Stokes vector of the output beam. We used *Mathematica* to perform the calculation of the 16x16 system. The resulting Müller matrices of the beam splitter and the *Infinitube* system are:

$$\mathbf{M}_{BS} = \begin{bmatrix} 0.210 & -0.429 & -0.095 & -0.185 \\ -0.119 & 0.514 & 0.040 & 0.145 \\ 0.060 & 0.139 & -0.101 & 0.311 \\ 0.017 & 0.105 & -0.040 & 0.080 \end{bmatrix} \qquad 2.8$$

$$\mathbf{M}_{INFINI} = \begin{bmatrix} 0.646 & 0.354 & -0.049 & -0.081 \\ 0.463 & 0.920 & 0.048 & 0.043 \\ -0.150 & -0.343 & 0.532 & 0.127 \\ -0.179 & -0.300 & -0.278 & -0.722 \end{bmatrix} \qquad 2.9$$

Both matrices are non-ideal Müller matrices owing to the real and imperfect nature of the experimental devices. Nevertheless, notice that the values are below unity, and also the highest values are found in the main diagonals of the matrices, which indicate that these devices do not exhibit overpolarizing features [42]. Notice also that the signs of the elements M_{11}, M_{12}, M_{21}, and M_{22} of Equation 2.8 correspond to a Müller matrix of the reflection arm of an ideal beam splitter [55]:

$$\frac{1}{2}\begin{bmatrix} 1 & -1 & 0 & 0 \\ -1 & 1 & 0 & 0 \\ 0 & 0 & 0 & 0 \\ 0 & 0 & 0 & 0 \end{bmatrix}$$

This shows that although a beam splitter cube can effectively separate the intensity into to regular beams, the polarization states can deviate from totally linear polarized states. The deviation of Equation 2.8 from an ideal beam splitter behavior may arise from absorption and dichroism effects; scattering events due to imperfections and angular dependence on the Müller matrix of the device [55]. Nevertheless, as the beam splitter and the pump laser were maintained in a fixed position during all these experiments, the same behavior (i.e. Müller matrix) of the device is expected. On the other hand, Müller matrix

from Equation 2.9 corresponds to a more complex situation because it accounts for the Müller matrix of the complete *Infinitube* system. The *Infinitube* system used here (see section 2.2.2) comprises several lenses, filters and a beam splitter cube which is impossible to study separately without disassembling the imaging apparatus. In order to calibrate the optical response of the experimental setup, a Müller matrix without sample was calculated as follows:

$$\mathbf{S}_{out} = \mathbf{CP_2} * \mathbf{M}_{INFINI} * \mathbf{M}_{ns} * \mathbf{M}_{BS} * \mathbf{CP}_1 * \mathbf{S}_{laser} \qquad 2.10$$

Here, $\mathbf{CP}_1$ and $\mathbf{CP}_2$ stand for the Müller matrices of the circular polarizers, $\mathbf{M}_{ns}$ is the Müller matrix of the experimental setup without sample; and $\mathbf{S}_{laser}$ and $\mathbf{S}_{out}$ are the Stokes vectors of the illumination laser and the output beam, respectively. In order to account for the non-ideal factors in the experimental arrangement, a calibration Müller matrix must hold the following relation:

$$\mathbf{M}_{ns} * \mathbf{M}_{cal} = \mathbf{I} \qquad 2.11$$

Where **I** is the identity matrix. In other words, the calibration matrix is the inverse of the matrix without sample. With this approach one can obtain an experimental identity matrix with low deviation in comparison with the ideal identity matrix. In our case the resulting experimental identity matrix is:

$$\mathbf{I}_{exp} = \begin{bmatrix} 1 & -3.89*10^{-15} & 1.40*10^{-14} & -1.05*10^{-14} \\ -7.80*10^{-15} & 1 & -9.22*10^{-15} & 8.82*10^{-15} \\ -6.80*10^{-15} & 1.76*10^{-15} & 1 & 8.68*10^{-15} \\ 1.43*10^{-15} & 1.17*10^{-17} & 8.29*10^{-16} & 1 \end{bmatrix} \qquad 2.12$$

All the calibrations were done before the mechanical test of the bovine pericardium. During the tensile tests, the virtual instrument recorded 10 images for each of the 16 position combinations of the circular polarizer. After the tests, each set of 10 images is averaged to obtain one single averaged image. A 1/5 reescalation of the 1392x1040 pixels images is done to obtain images of 278x208 pixels. Without this reescalation, the computer requirements to perform the data processing surpass the specifications of a conventional personal computer and the *Mathematica* kernel aborts evaluation. After the reescalation, a

16x16 matrix system per each pixel is solved according to Equation 2.10 replacing the Müller matrix without sample to the corresponding Müller matrix for each deformation step (i.e. the so called Müller matrix imaging). All the calculations were performed by means of *Mathematica*. We obtained a set of Müller matrices per each pixel in each step of the test in which the virtual instrument waits for the fiber relaxation process to end. After calculation of the experimental Müller matrices, the differential matrix decomposition was performed in order to have the mean values of the 16 elements of the matrices. Then, the results were plotted in a false color scale images of the important parameters of the Müller matrices. In particular, we selected the linear retardance δ ($\mathbf{L}_m(2,4)$), the angle of orientation of the axis of linear retardance θ, the optical rotation Ψ and the net depolarization Δ, as defined in reference [56]:

$$\theta = \frac{1}{2}\tan^{-1}\frac{[\mathbf{L}_m(2,4)]}{[\mathbf{L}_m(3,4)]} \qquad 2.13$$

$$\Psi = \frac{1}{2}\mathbf{L}_m(2,3) \qquad 2.14$$

$$\Delta = \frac{1}{3}\left|[\mathbf{L}_m(2,2)]+[\mathbf{L}_m(3,3)]+[\mathbf{L}_m(4,4)]\right| \qquad 2.15$$

Here, $\mathbf{L}_m$ corresponds to the logarithm matrix from the differential matrix formalism. Additionally, a spatial correlation was performed using a Gaussian kernel of 3 pixels of diameter with the built-in image filters of *Mathematica*. This allows minimizing the CCD bias noise in the Müller matrix images by spatially averaging the images. With this optical arrangement and the imaging post-processing, the final resolution of the Müller matrix images is 30 μm per pixel. The original images consisted in 1392 x 1040 pixels imaging an area of ~3mm^2 which gives a resolution of about 2μm per pixel. These original images were escalated to 1/5 to its original resolution; giving images of 278 x 208 pixels in the same imaging area which correspond to a final resolution of about 10 μm per pixel. The results of the Müller matrix imaging in the tensile tests can be observed in Figures 2.13-2.16.

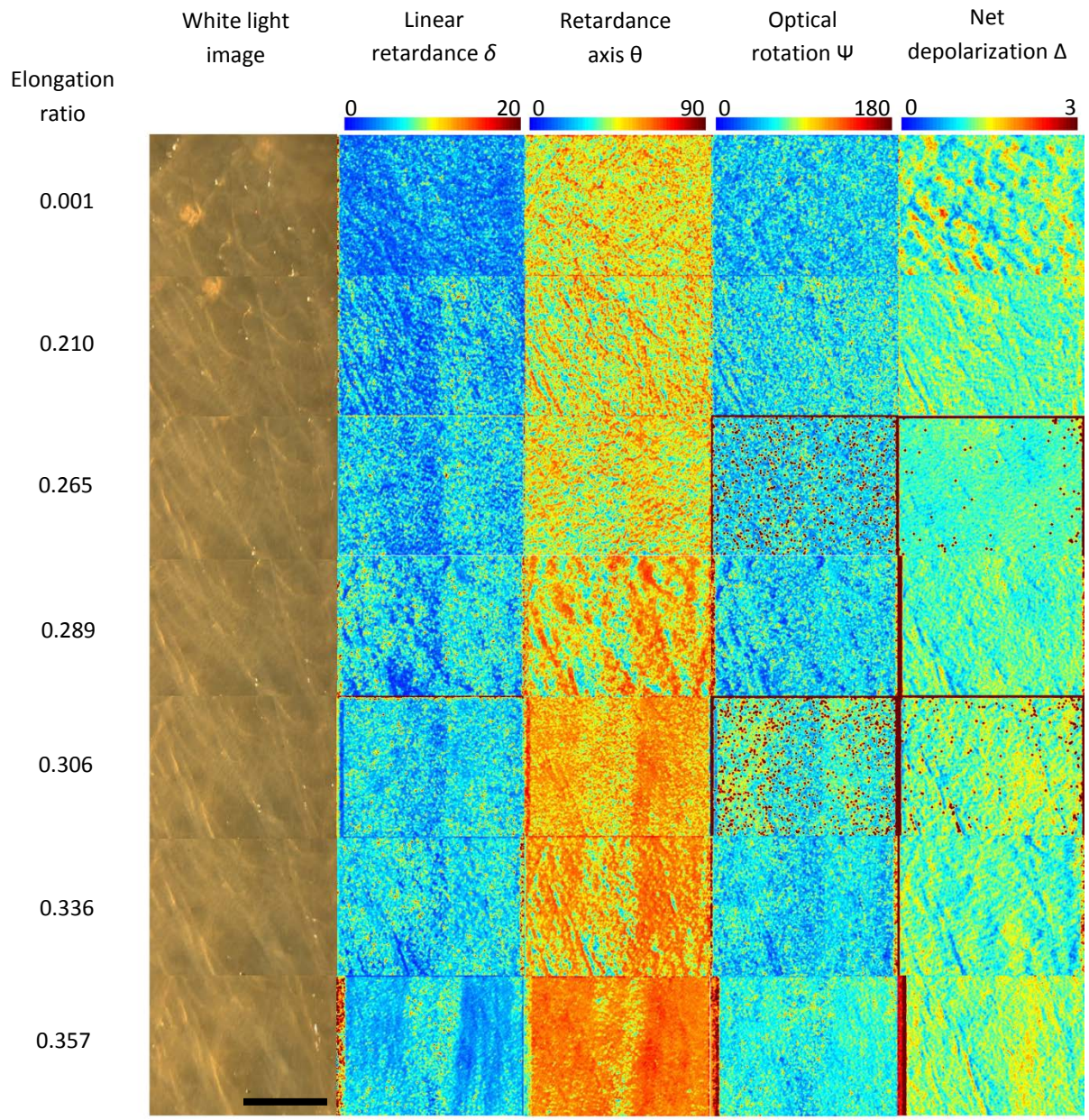

Figure 2.13. White light images and Müller matrix imaging during the tensile test for the $M_{\parallel}$ sample. The scale bar in the last white light image corresponds to 1mm.

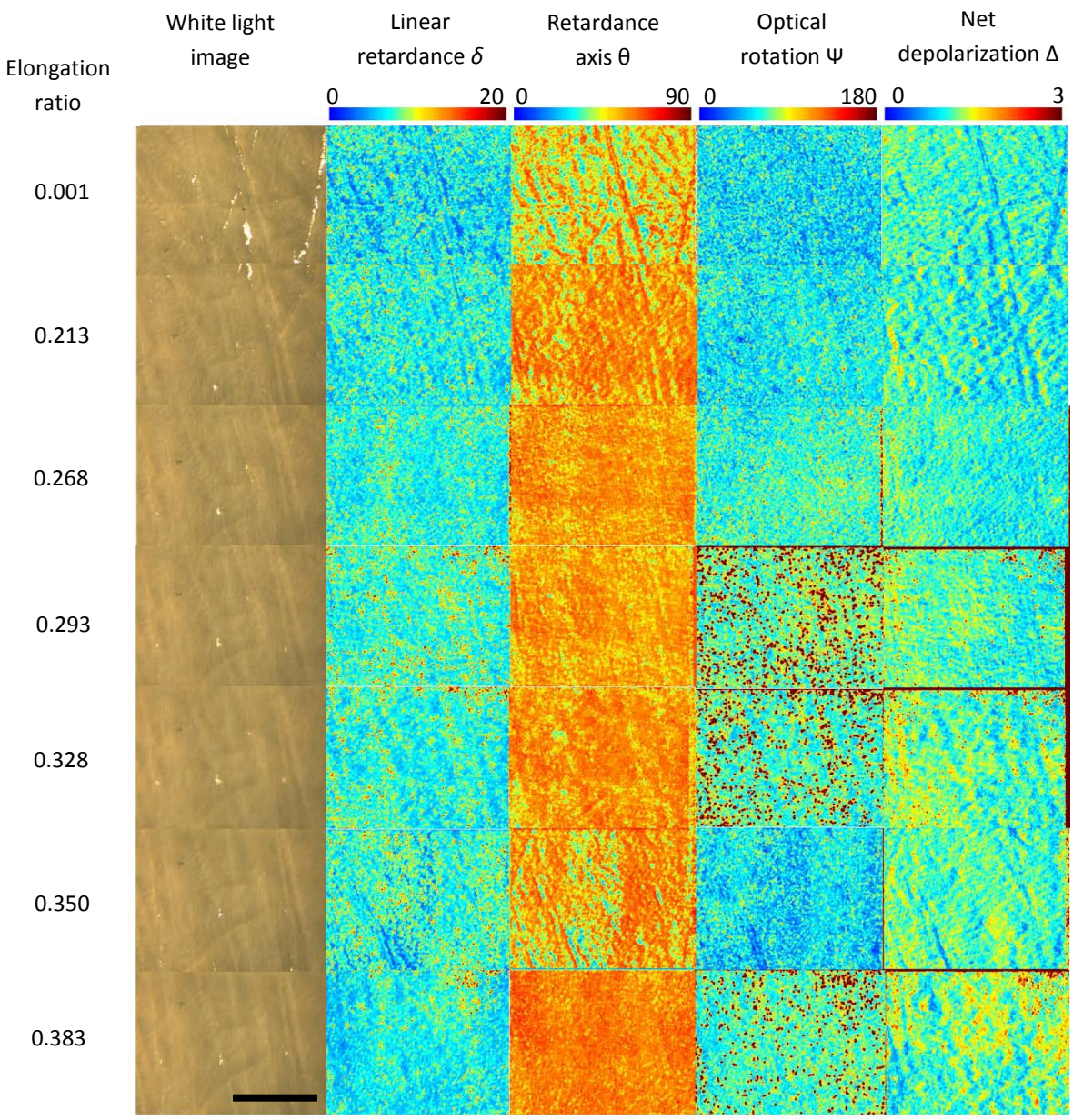

Figure 2.14. White light images and Müller matrix imaging during the tensile test for the $M^{\perp}$ sample. The scale bar in the last white light image corresponds to 1mm.

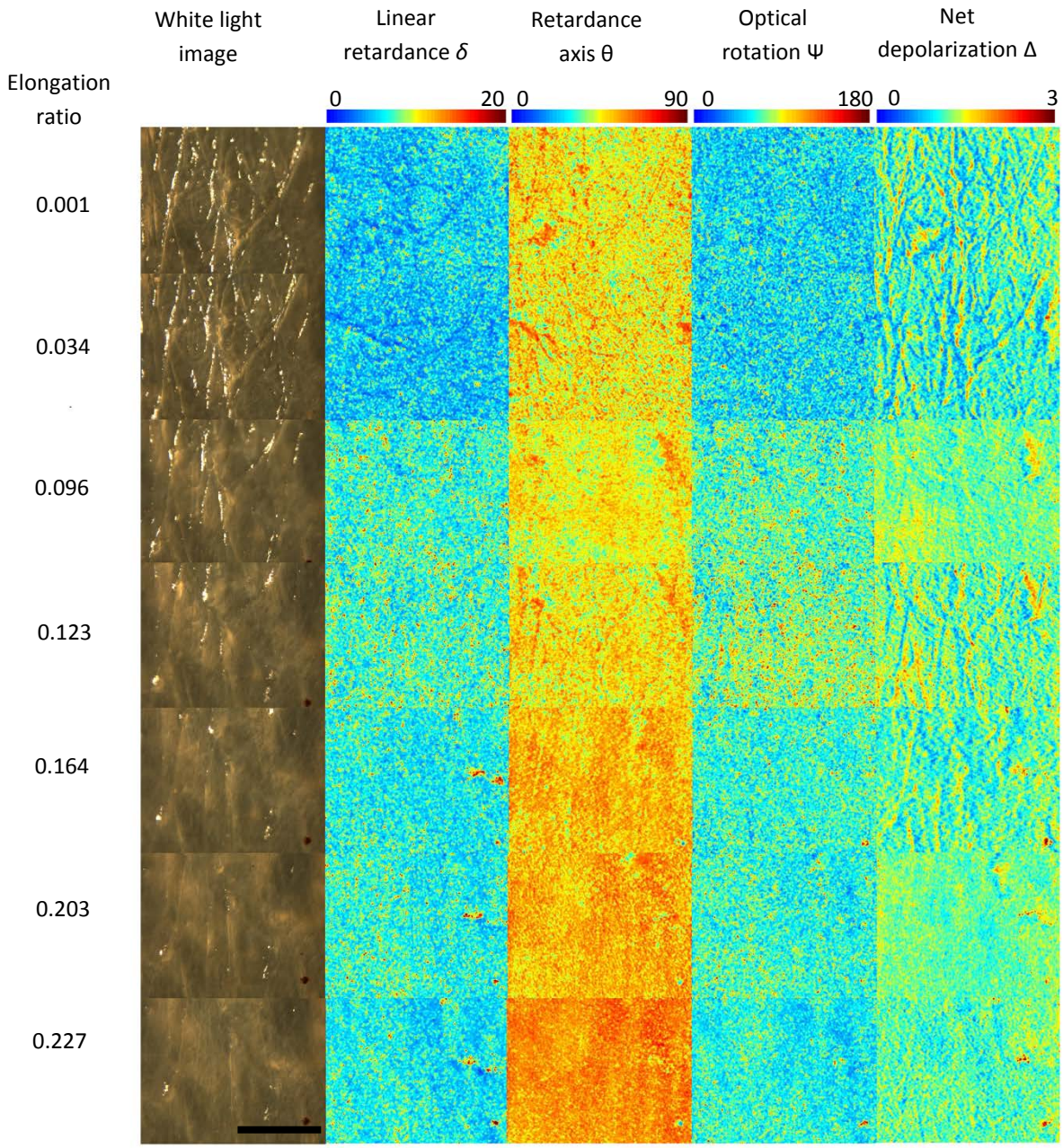

Figure 2.15. White light images and Müller matrix imaging during the tensile test for the $A_{\parallel}$ sample. The scale bar in the last white light image corresponds to 1mm.

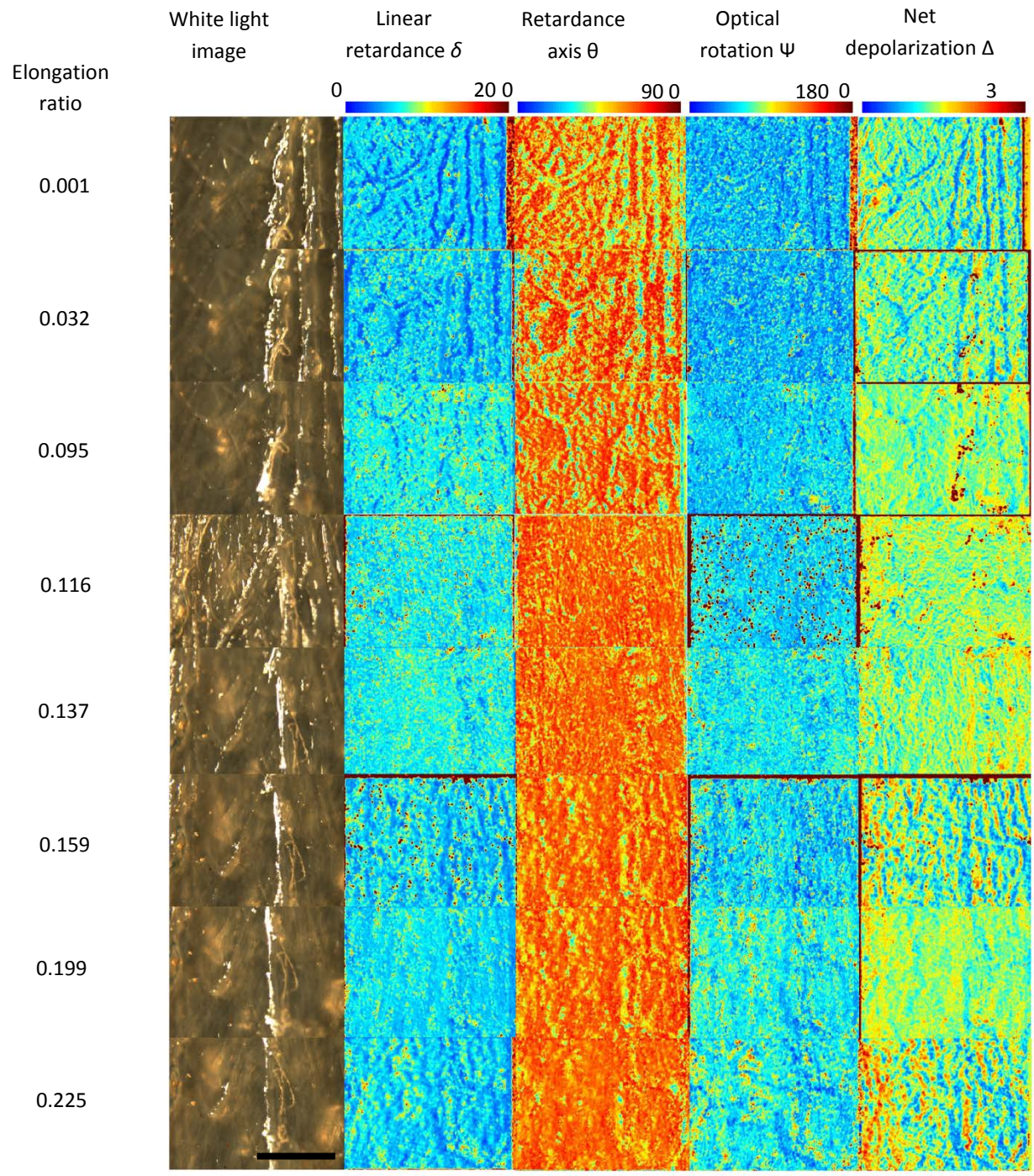

Figure 2.16. White light images and Müller matrix imaging during the tensile test for the $A^{\perp}$ sample. The scale bar in the last white light image corresponds to 1mm.

In general, the images shown in figures 2.13-2.16 have very different features, as each figure corresponds to a different pericardium sample. Furthermore, the images show particular optical textures that depend on each sample. This emphasizes the fact that we are probing a relative large area in a material with a complex structure. The tissue microstructure is so complex that two samples that have been cut from the same pericardium sac can give rise to totally different optical textures. It is important to note that Müller matrix images are different to white light images because the light recorded in the former is the light that interacts with the superficial layers of the sample; in contrast, Müller matrix imaging is a transmission method based on recording and analyzing the light that has traversed the sample. In this sense, Müller matrix imaging contains information about the whole thickness of the tissue sample.

Examining closely each set of images in figures 2.13-2.16 we can identify distinctive features for each of them. In general, the retardance axis shows an increasing trend as the elongation ratio increases. The retardance axis is the arctangent of the ratio of linear retardances of the X/Y axis to the 45°/-45° axis (see Equation 2.13). This parameter gives information about the preferred orientation of the slow axis, analogous to the birefringence axis in a birefringent homogeneous bulk material. As seen in figures 2.13-2.16, the images of the retardance axis start with a high contrast texture for low elongation ratios. When the elongation ratio increases, the images tend to have less color contrast and more homogeneous color images are obtained, changing from yellow-blue spots to yellow-red spread areas. According to the color scale bars in figures 2.13-2.16, the red-black color corresponds to a 90° value; this coincides with the experimental Y-axis, along which the load is exerted. This means that uniaxial deformation tends to align the fibers along the longitudinal axis over the whole area of the sample. As microfibers align towards the Y-axis, the refractive index in that direction also increases, setting a preferred slow axis in the direction of the applied load. This description is in concordance to the results of the stress-elongation ratio curves shown in previous sections, in which the linear behavior of the curves is attributed to an alignment process within the tissue.

The optical rotation is also known as circular retardance because it represents the difference in refractive indices for right and left circularly polarized light. A large difference between these indices implies a higher optical rotation. A linearly polarized beam can be obtained with the combination of a right and left handed circularly polarized beams, hence the optical rotation is also a measure of the rotation of a linearly polarized beam. Typically, optical rotation is used to find the concentration of chiral molecules, such as sugar in liquid solutions [57, 58]. The optical rotation images obtained in these experiments demonstrate a high presence of chiral molecules as the typical value range lies between 30 and 90 degrees (blue-yellow in the color pattern). This is to be expected as collagen is intrinsically chiral due to its helical structure [49].

In general, the evolution of optical rotation images as function of elongation ratio is highly dependent on the tissue sample probed. Although the samples from images 2.13-2.16 were cut from the same pericardium sacs, the different layout of the fiber ensemble in each sample generates different color patterns in the optical rotation images. For all samples the first two optical rotation images (first and second row) show very low changes. After these first two deformation steps, the optical rotation images can exhibits abrupt changes from consecutive steps. Notice for example the evolution of optical rotation from second to third row in Figure 2.13 in which a blue-green dominant pattern changes to an image with red-black points spread over all the imaged area. In general, for some elongation ratios, an evolution in optical rotation is apparent from the changes registered in the color patterns; this suggests that the optical rotation increases for some loading conditions. Figures 2.13-2.16 show also that optical rotation is correlates more with the net depolarization than with the retardance as the change in color pattern of the optical rotation during the test seem to match with the behavior of the net depolarization. In literature [58] these two effects (optical rotation and depolarization) have been associated with diffusive scattering modeling an optical turbid media as an optical rotator coupled with a depolarizing element which imposes an angle of rotation α and linear and circular depolarization βl, βc respectively. Apparently, during the complete mechanical tests no specific trend in the optical rotation arises. Nevertheless, the images corresponding to the last steps in the tests tend to show a green-yellow pattern, which indicates higher values of

optical rotation than the blue-green from the start of the tests. This can be explained as an increase in concentration of chiral molecules (collagen) along the transversal direction of the sample due to lateral compression during the test. In general, the optical rotation images of figures 2.13-2.16 show that with a further proper calibration, this technique can be useful to give information about the distribution of collagen content in small tissue areas.

In contrast to optical rotation, in which the main factor to induce this parameter is chiral molecules concentration, average depolarization in tissue appears mainly due to multiple scattering. When multiple scattering is present, the polarization of a beam randomizes as the pathlengths get scrambled. The change from a totally polarized state to a partially polarized or a non-polarized state is called depolarization. The images corresponding to average depolarization in Figures 2.13-2.16 show in general that some fiber features appear in different loading conditions (see for instance Figure 2.16 rows 1, 2, 6 and 8). For other deformation conditions, the contrast decreases and more homogenous images around an intermediate value of depolarization are observed (Figure 2.16 rows 3, 4, 5 and 7). This suggests that for some of the deformation conditions probed here, most of the scattering events occur within the macrofibers. This is more evident in the images obtained for high elongation ratios. Notice that the red-black spots that appear in the optical rotation images appear also in the average depolarization images in the same row of figures 2.13 and 2.14. This is another clue pointing at localized scattering zones as a plausible explanation for the appearance of the red-black spots.

One of the most important parameters obtained from the Müller matrix analysis is the linear retardance δ. This is a measure of the birefringence character of the sample, and from the resulting images shown in the figures, the linear retardance range between the values of 0-20 deg. Some high retardance features coincide with the fibers observed in the white light images. However, some other fiber-like features in the retardance images do not correspond to the observed macrofibers in their corresponding white light images. This is because Müller matrix imaging provides information about more internal fibers than

those obtained with white light images. The optical retardance images of Figures 2.13-2.16 show in general an increase when the elongation ratio increases. Previous reports on this kind of tissue have shown the presence of alignment and compression effects when samples are subjected to uniaxial tension [31]. Alignment to the elongation axis and compression in the perpendicular axis of elongation can effectively explain the increase of birefringence as more collagen fibers interact with the probe beam in a vertical fashion. With more content of fibers in the vertical direction the net difference of refraction index in the vertical and horizontal axis increases and so the retardance. Interestingly, some high retardance spots can be seen and can also be associated with high elongation ratios in Figures 2.13-2.16. This can be related to a high shear stress into fiber-fiber cross-link sites generated by the glutaraldehyde treatment. This can be a possible scenario owning to the matching of the system resolution (30 μm) with the diameter of the macrofibers (30 – 50 μm) [49]. Furthermore, high retardance spots have been reported before as a consequence of the cross-linking effect in collagen based tissues [59]. As we will see in next sections, linear retardance can also be related to the mechanical properties of the tissue, and in this case our retardance images correlate well with the micromechanical behavior of the tissue.

A full description of all the parameters of the Müller matrix needs a rigorous treatment and is beyond the scope of this work. The main objective of this technique in this context is to give a general idea of the polarization features of the tissue samples subjected to uniaxial tension. This analysis will also help to compare the results with the features of random laser emission when Rhodamine 6G is incorporated in the tissue samples (Chapter 3 and Chapter 4).

2.4.4. Digital image correlation

Digital image correlation is a full-field and non-contact technique to measure displacement/strain vector fields (DVFs) on the surface of materials. With the series of white light illumination images acquired during the mechanical tests, the DVFs $\boldsymbol{u}_k(x_k, y_k)$ and $\boldsymbol{v}_k(x_k, y_k)$ between pair of images were calculated by using the Willert and Gharib algorithm [60]. Here $\boldsymbol{u}$ and $\boldsymbol{v}$ represent the displacement vectors of the object or region of

interest in the x and y directions, respectively [61, 62]. The position coordinates in each image are represented by x and y and the subindex k indicate the corresponding object/region of interest, which is defined as an area of 64×64 pixels. Hence, a full image is divided in subimages (64×64 pixels) used to perform the DIC analysis yielding the DVF for the full image and for a given loading condition. The in-plane strains in the sample were evaluated by minimizing the errors of a six parameters linear model (typically used in linear elasticity theory) and previously used in other materials including bovine pericardium [62]. This minimization yields the values for the normal strain in the x and y directions (ε_x and ε_y), translation, shear strain (ε_{xy}), and in-plane rotation within the analyzed region of the sample.

We selected three pairs of images of the set corresponding to the $M_{\parallel}$ sample. These correspond in turn to the three characteristic stages of the tensile test as described in section 2.3.1. The left column of Figure 2.17 shows the images obtained using white light illumination of the bovine pericardium sample together with the corresponding displacement vector fields (superimposed white lines with arrow heads). The displacement vector fields are obtained with DIC upon comparing subsequent images for different loading condition. The figure shows three sets of vectors, one for each of the stages of the tensile test; the DVFs for each region were obtained from image pairs acquired during the elongation test. For this particular case, the selected images correspond to elongation ratios of 0.001 (Figure 2.17a), 0.21 (Figure 2.17b) and 0.35 (Figure 2.17b). For comparison, the corresponding images for the linear retardance δ in degrees, calculated through differential matrix decomposition, are shown in the right column of the same figure. The linear retardance for each pixel is represented in an arbitrary color scale and is shown together with the corresponding displacement vector fields.

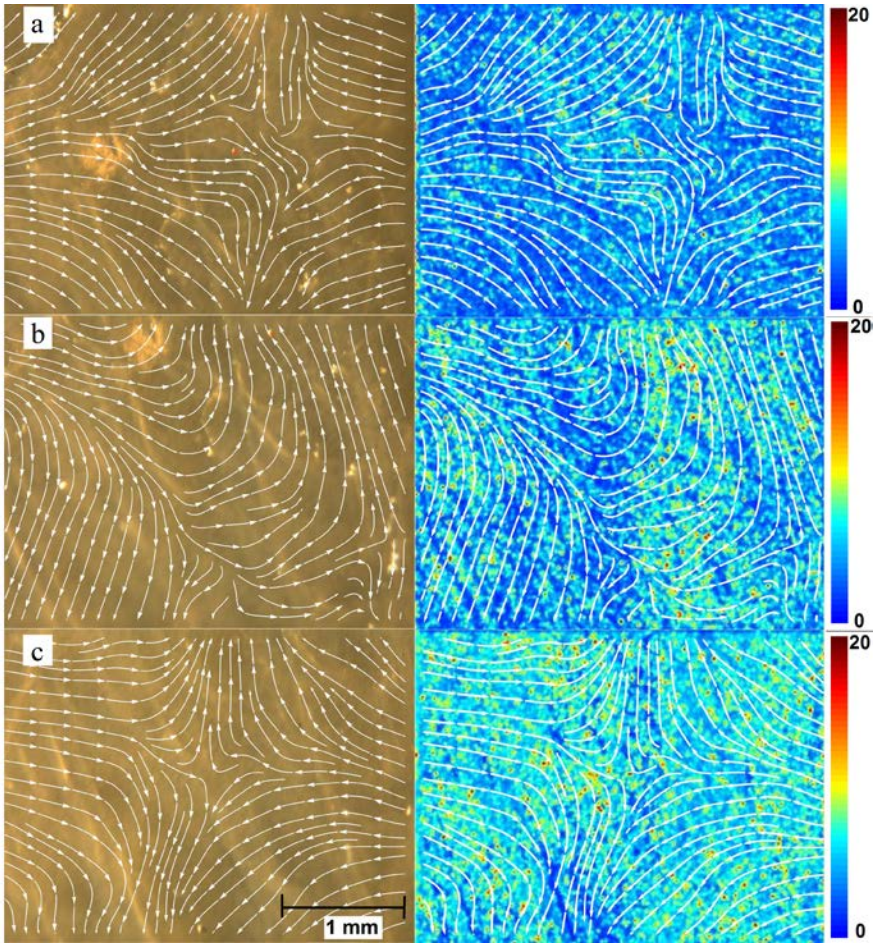

Figure 2.17. First column: white light images of the bovine overlapped with its corresponding displacement vector fields. Second column: retardance images obtained from Müller matrix imaging overlapped with its corresponding displacement vector fields. The scales for the retardance images are in degrees. Each row is associated with different elongation ratios during the tensile test (see text).

The displacement vector fields in Figure 2.17a display a larger displacement component along the perpendicular axis to the applied load. Since Figure 2.17a corresponds to elongation conditions in which the fibers are not aligned, some compression is to be expected owing to fiber displacement during the initial elongation. The retardance image for the initial conditions (right column of Figure 2.17a) shows a relatively regular distribution of low retardance. This is a consequence of the highly isotropic orientation of the fibers for this loading condition, where alignment is not yet achieved. Notice also that the zones with highest retardance in Figure 2.17a tend to match the elongation components

of the displacement vector fields, suggesting that the vectors are attracted to the zones with higher retardance. For elongation ratios beyond 0.2, the displacement vector fields exhibit a clear change as the predominant component is aligned towards the loading axis, as seen in Figure 2.17b. This alignment is associated with the appearance of high retardance zones increasing the contrast of the image. In general, the displacement vector field in Figure 2.17b tends to run from high retardance zones to lower retardance zones as in Figure 2.17a. Finally, the displacement vector fields of Figure 2.17c shows the characteristic hyperbolic pattern of an aligned ensemble of fibers, as expected within the linear region of the tensile test [61, 62]. In this case the retardance image displays a spread of higher retardance zones, owing to an increased interaction among the microfibers within the tissue [59]. In general, high retardance zones tend to spread as the elongation ratio increases. Notice however that for larger loading conditions, some of the zones with low retardance seem to attract the displacement vector fields (see lower part of Figure 2.17c). This may be attributed to buckling in the central part of the image, which has been previously reported to appear in bovine pericardium tissue samples under high stress conditions [31].

Another interesting feature of the retardance images is the localized points of high retardance. These localized points reach the maximum values of the color scale and become more evident as the load increases (see Figure 2.17c). An increase in collagen fiber interactions typically leads to the rupture of cross-links between adjacent fibers [49]. Mechanical testing of bovine pericardium tissue has shown to generate cross-linking rupture creating localized zones of high shear stress [31]. This condition is achieved under the loading conditions shown in Figure 2.17b and leads to changes in birefringence appearing as localized zones with high retardance (Figure 2.17c). Similar conditions have been observed when studying collagen cross-linking effects in corneal tissue using polarization sensitive OCT [59]. Finally it is important to note that in order to perform the Müller matrix imaging, several images with fixed position of the sample are required. On the other hand, the displacement vector fields are obtained by correlating two images with different elongation conditions. In other words, the Müller matrix imaging is a static technique (i.e. fixed elongation ratio) while digital image correlation is a dynamic technique (i.e. two elongation ratios are probed). Furthermore, the two elongation ratios

probed to obtain the displacement vector fields observed in Figure 2.17 are the one corresponding to the Müller matrix test and the corresponding to the next microstep of the test. Therefore, the results shown in Figure 2.17 suggest that for small deformations, the retardance images may predict the response of the sample to a uniaxial stress. This in turn is attainable as the orientation and concentration of collagen fibers mainly determine the mechanical behavior of the sample and optical retardance gives information about orientation and concentration of collagen fibers within the pericardium samples.

These results demonstrate that several optical passive measurements can be incorporated into tensile tests of bovine pericardium tissue in order to elicit complementary information regarding the mesoscopic and microscopic structure of the tissue samples. In particular digital image correlation, Müller matrix imaging and enhanced backscattering were adapted to perform simultaneously with the tensile tests. The proposed experimental arrangement is thus capable to provide information at different scales during a single mechanical test. In particular, the mean free path of medial samples showed an increase as elongation ratio increases. Longer mean free paths in these samples are associated to the linear region of the tensile test, where fibrils are in a more compact and aligned arrangement. Furthermore, the typical values of mean free paths are in the order of tens of microns which is a length shorter than the macrofibers mean diameter (0.1 mm) and larger than the mean fibril diameter (100 nm). This indicates that the scattering events inside the macrofibers (i.e. intrafibrillar) dominate the mean free path measurements. On the other hand, the spatial resolution of the imaging apparatus used here is in the order of the mean free path and Müller matrix imaging is unable to resolve the intrafibrillar features. This in turn means that the main contribution of the color contrasts in Müller matrix images is the structure and interaction of macrofibers (i.e. interfibrillar).

In these kinds of experiments, digital image correlation provides information related to the interaction between the tissue matrix and the collagen fibers [31]. The displacement vector fields obtained by digital image correlation show a good correlation with the retardance images calculated by means of Müller matrix imaging. These observations

suggest that displacement vector fields tend to run from low retardance zones to high retardance zones, where more fiber interaction is present. Similar trends in changes of tissue structure during mechanical tests have been reported using more elaborated techniques such as OCT and SAXs [35, 59]. We therefore believe that incorporation of these optical tools for tissue characterization represents a promising approach for elucidating mechanical properties of materials used for biological prosthetic devices. Additionally, these efforts will help to compare the results of random laser emission from the same kind of tissue. This will be explored in the following chapters.

CHAPTER 3

RANDOM LASER ACTION IN BOVINE PERICARDIUM TENSILE TESTS

Presumably, random laser emission can extract structural information high resolution, capable to resolve the extraction of a few scatterers form the whole scattering ensemble. Although random lasers are a novel and intriguing kind of light sources, their applications have been in stand-by since their appearance in the late 90s. We expect that this work on random laser based on the comparison with scattering techniques will help to develop new applications in the field of tissue diagnosis by means of optical methods.

Several scattering and polarization features of bovine pericardium obtained during tensile tests were presented in the previous chapter. In particular, data analysis allowed for relating the mean free path with the stress-elongation ratio curve, and the optical retardance with the displacement vector field. This was possible due to the use of techniques such as enhanced backscattering and Müller matrix imaging. Both techniques rely in the fact that no optical absorption takes place within the material, and optical scattering is the main mechanism of interaction between light and tissue. Nevertheless, when an active (luminescent) agent is added to highly scattering media, random laser emission can be achieved. As briefly described in Chapter 1, this intriguing effect has been reported in a variety of materials. When the size of the scatterers is in the order of magnitude of the wavelength of the fluorescence spectrum, and the scattering strength is high enough, random laser action is achievable [3, 7, 13]. The scattering strength depends mainly on the geometry of the scatterers, the volume fraction and the refractive index contrast [3, 21]. As the scattering strength modifies the way light travels within the disordered media, the spectral features of random laser emission are also changed.

In this chapter, we study the light emitted by an organic dye within bovine

pericardium subjected to uniaxial tension. The main idea is obtaining laser light by means of the random laser effect due to the collagen structure of tissue, which as described in the previous chapter, exhibits scattering properties in the visible region of the optical spectrum. We expect different characteristics in the random laser emission during the tensile test because mechanical deformation changes the internal configuration of the ensemble of collagen fibers. These changes should be related to the macroscopic characteristics of the tissue such as stiffness and elasticity, because the spectral features of random laser emission depend on the scattering ensemble. We begin with the characterization of the active media in order to obtain an optimal concentration of the dye in glycerin that will provide maximum fluorescence. Then, we describe the sample preparation procedure and the experimental setup. Finally, we present an analysis of the random laser emission and a discussion about the experimental results.

3.1. CHARACTERIZATION OF THE ACTIVE MEDIUM: RHODAMINE 6G IN GLYCERIN

The active medium selected for these experiments was Rhodamine 6G (R6G) and the choice was made based on our previous experience in SiO_2 nanoparticles random lasers [13, 24]. Rhodamine 6G provides a very efficient active medium with large fluorescence lifetimes (~4 ns); it can be dissolved in a variety of solvents such as methanol, ethanol or water. R6G with a purity of 96% was acquired from *Sigma-Aldrich* in order to perform the random laser emission experiments. The absorption of this dye lies in the green region of the optical spectrum and exhibits a fluorescence intensity centered around 550 nm when is dissolved in methanol [39, 40]. Although methanol is the most common solvent used to achieve random laser action with R6G as active media, the rapid evaporation of alcohol based solutions leads to quick drying of the tissue samples making them brittle. In order to maintain the tissue moistened during the mechanical test, a solution of R6G and glycerin was chosen as the active medium for these experiments. The glycerin-based solution allows also to "freezing" the dye molecules during the pump pulse, minimizing additional disorder features due to Brownian motion [40]. A typical intensity spectrum of R6G-glycerin solution pumped with a 532 nm pulsed laser is shown in Figure 3.1.

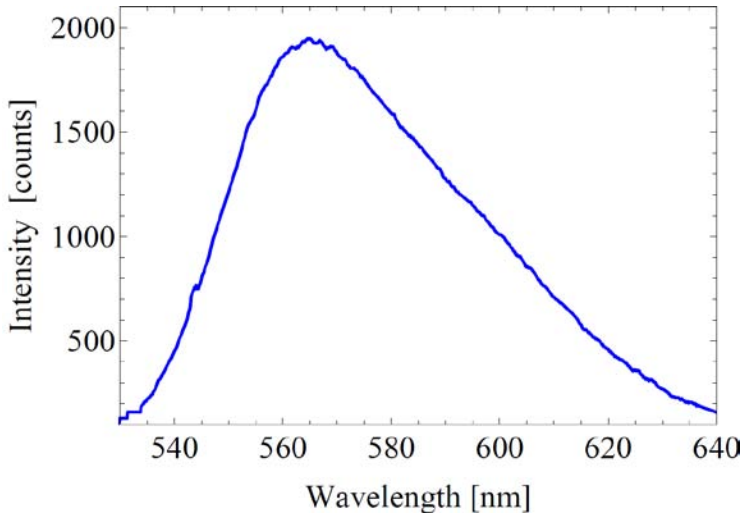

Figure 3.1. Fluorescent spectrum of Rhodamine 6G dissolved in glycerin. The solution was allocated in a quartz cuvette and pumped with a Nd:YAG pulsed laser. The measurement was performed with a fiber-coupled solid spectrometer (Ocean Optics HR4000).

In general, the fluorescence properties of dyes depend on the matrix in which they are dissolved. Hence, a characterization of the emission spectrum for the R6G-glycering mixture was carried out. Figure 3.1 shows the spectral width (full width at half maximum ~ 60 nm), which is a characteristic of fluorescent emission. The maximum intensity was located at ~565 nm. As we will see in next subsections, these spectral features change dramatically when the dye solution is incorporated into the tissue samples. Another important experimental parameter for this work is the concentration in which the R6G is dissolved in the solvent matrix. In order to find the optimal concentration of R6G in glycerin, we pumped different mixtures with different concentrations from 0.5 to 2 g/l with the same energy per pulse (7mJ). Subsequently, the integral of the intensity spectrum was calculated in order to find the spectral energy density as function of R6G concentration; this is shown in Figure 3.2.

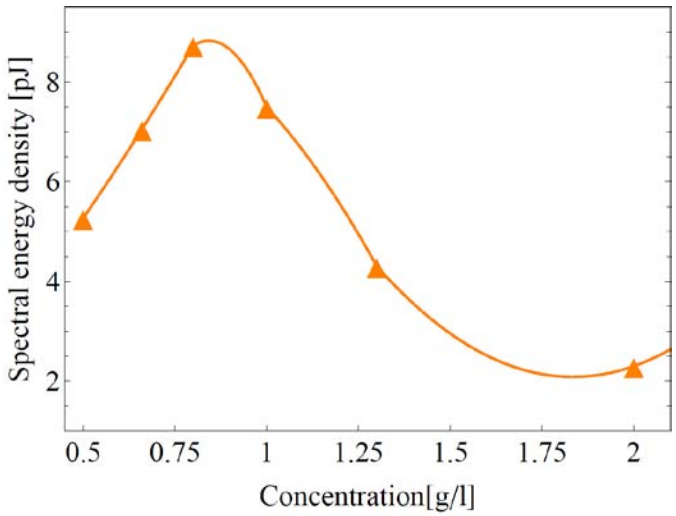

Figure 3.2. Spectral energy density as function of R6G concentration for the fluorescent emission of the glycerin-R6G solution.

The spectral energy density curve (Figure 3.2) shows a maximum near a concentration value of 0.8 g/l. This optimum concentration is slightly different from those reported for ethanol based solutions [64]. Nevertheless, figures 3.1 and 3.2 show that R6G-glycerin solutions are suitable as an active medium for random lasers because the fluorescent emission is comparable with alcohol-based solutions. Based on this finding, we choose the concentration of 0.8 g/l R6G in glycerin to study the random laser emission from bovine pericardium samples. Another important issue regarding the solution R6G-glycerin is the possible degradation of the dye after a given number of pump pulses. In general, dye molecules can exhibit degradation due to the interaction with the pump beam ceasing the fluorescent emission. The susceptibility of a dye molecule to present photodegradation depends on the matrix in which the molecule is dissolved. A decrease in fluorescence effectively reduces the net gain in a laser and modifies its behavior. In order to corroborate that photodegradation does not affect significantly in the range of energy pulses used for these experiments, a photodegradation test was performed and the results are shown in Appendix D. After 35 pulses at 10 mJ, the variation in the energy captured by the spectrometer was less than 0.01%. This indicates that photodegradation will not play a significant role in the experiments shown in next sections.

3.2. SAMPLE PREPARATION

In order to compare the results from random laser experiments with those shown in Chapter 2 (i.e., with no dye incorporated in the pericardium tissue), sample preparation must be very similar. As in the previous experiments, pericardial sacs specimens were collected from a local slaughterhouse and washed with a phosphate buffered saline solution right after the death of the bovine. The fixation process was carried out during 24 hours at 4°C, using 0.5% glutaraldehyde in 0.1 M phosphate buffered saline solution with a pH of 7.4, in a custom-built frame as described in Chapter 2. The protocol used in these experiments is shown in Table 3.1.

Bovine death.	t=0
PBS washing.	t<1hr
GA fixing (PBS+ 0.5%GA).	t<4hr
Sample cutting.	t<1 day
Glycerin-R6G immersing	t<2 days
Optomechanical tests.	t<2.5 days
Material disposing.	t<3 days

Table 3.1. Sample preparation protocol from the death of the animal to the material disposing

After the fixation process, different samples from the same pericardial sac were cut. The cuts were done parallel and perpendicular to the apex axis (see Chapter 2, subsection 2.2). As before, these samples from different sections of the sac will help studying the effects of the orientation of the collagen fibers on the mechanical behavior of the tissue, as well as the contribution from the anisotropy of the complex material prevails.

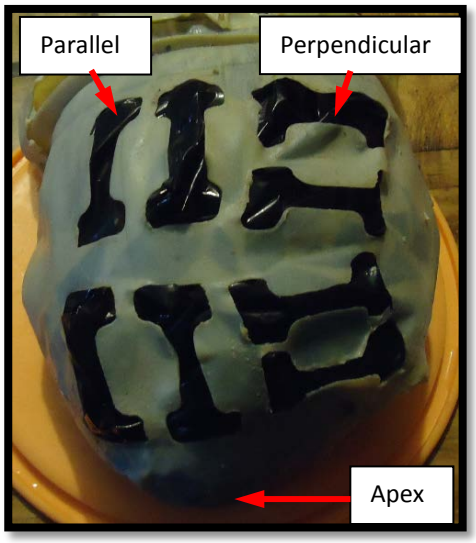

Figure 3.3. Photograph of a bovine pericardial sac after sample cutting. The photograph shows different cuts along the base-apex axis and other cuts done perpendicular to the base-apex axis.

Figure 3.3 shows a photograph of the actual bovine pericardial sac illustrating the cuts near the apex (apical samples) and in the medial zone (medial samples). After the samples are cut, they are immersed in a solution of R6G in glycerin at 0.8 g/l during 24 hours. Finally, the optomechanical tests are performed in a time lapse of a couple of hours before disposal. With this protocol, the tissue is disposed within the first 72 hours, counted from the death of the bovine. This sample preparation protocol is very similar to that presented in Chapter 2; as seen upon comparing Table 2.1 and Table 3.1, the only change between both protocols is the incorporation of R6G in glycerin before the optomechanical tests. This in turn will help to compare both sets of results (Chapter 2 and Chapter 3) and associate the scattering properties of the tissue with the spectral features of the random laser emission.

3.3. EXPERIMENTAL SETUP

3.3.1. Load frame

The mechanical testing device used in this set of experiments is the same as that

described in subsection 2.2.1, Chapter 2. Briefly, a mechanical actuator provides displacement in the vertical axis while a load cell coupled to the end of the actuator allows for monitoring the force exerted by the actuator. A displacement sensor (a linear variable differential transformer, LVDT) completes the sensor scheme of the load frame by registering the position at the end of the actuator (see Figure 2.3, Chapter 2). A set of grips specifically designed to avoid damage in the tissue samples are used to hold the tissue samples. The load frame is held together by stainless steel beam and data acquisition was carried out using *LabVIEW* to operate the electronic devices.

3.3.2. Illumination and optics

Incorporation of R6G into the tissue turns the samples into an active medium. In general, an experimental setup involving active media requires a pump source and adequate blocking of residual pump energy. In these experiments, the pump energy was provided by the same Nd:YAG pulsed laser described in previous sections and the residual pump was blocked was done by notch filters (*Thorlabs* NF533-17, > 90% blocking efficiency at 532 nm, 17 nm spectral width). These filters were required in order to prevent CCD saturation in the cameras. Finally, the pump beam was directed towards the samples using a silver coated mirror and a 50-50 beam splitter, as depicted in Figure 3.4.

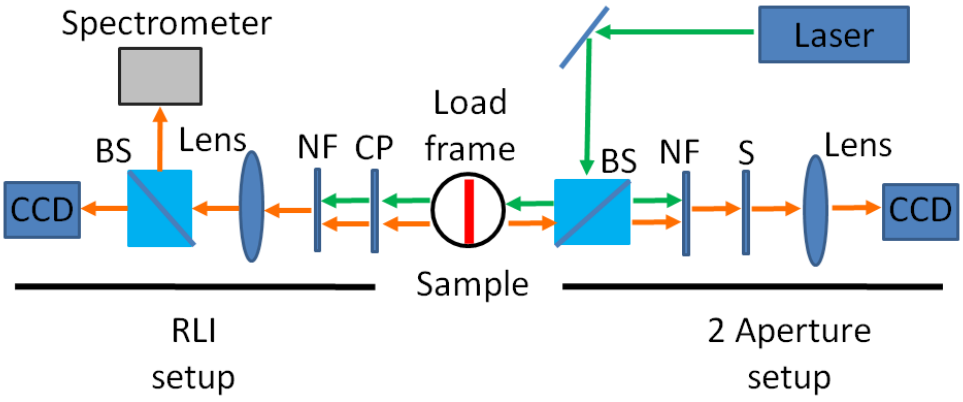

Figure 3.4. Schematic representation of the experimental setup. The experimental arrangement can be subdivided in two setups: random laser imaging (RLI) and two apertures setup. NF: Notch filter. CP: Circular polarizer. BS: Beam splitter. S: Custom made two apertures slit.

As shown in Figure 3.4, the experimental arrangement can be described in terms of two setups; one for imaging the random laser emission (RLI) and the other to probe the coherence features of this emission by means of a custom-made two apertures slit. While the random laser imaging setup collects the light that is emitted from the samples in a forward direction, the backward emission is collected by the two apertures setup. The latter is intended for studying the degree of spatial coherence by observing the interference patterns generated after the slits. Calibration and details about the fabrication of the custom made slit are included in Appendix E. The RLI setup is comprised by a circular polarizer as a polarization analyzer, an infinity-corrected microscope tube from *Infinitube*, a 5x *Mitutoyo* objective, a *Pixelink* CCD camera and a high resolution spectrometer (*Ocean Optics* HR4000). This experimental setup allows visualizing the random laser emission at the same time that its spectral features are analyzed with the solid state spectrometer.

As it can be seen in Figure 3.4, in this experimental setup no CP is used to control the polarization of the pump beam. In contrast to the experimental setup described in Chapter 2 where two CPs are used, the present experimental setup uses only one CP between the imaging device and the sample. The experimental setup schematically shown in Figure 3.4 allows analyzing the polarization state of the random laser emission but lacks in the polarization control of the pump beam. The reason of avoiding placing a CP to control the polarization of the pump beam relies in a possible damage of the device at high energy pumping. In previous papers, random laser action in bovine pericardium with pump energies in the order of 10mJ per pulse has been reported [26]. These energies are above the safe operation region of the available polarizers at the moment. This in turn fixed the pump polarization to the native polarization of the Nd:YAG laser. In general, this experimental setup shares characteristics with the visualization scheme described in Chapter 2. Features such as magnification, field of view and the CCD cameras are the same for both cases, hence allowing for subsequent image comparison from the two sets of experiments.

3.3.3. Virtual Instrument

In order to automatically control the electronic devices of the experimental setup we designed a virtual instrument written in *LabVIEW*. The virtual instrument registers force, displacement and time and acquires images of the random laser emission. The approach to develop this virtual instrument was the same of the one described in section 2.3.2, namely, a sequential linear programming in which several sub-virtual instruments are written and tested one by one. In general, the structure of the virtual instrument from section 2.2.4 is maintained (see figure 2.7) with the exception of the optical tests.

Data acquisition follows a similar approach to that used for the scattering measurements. After the first optical test with no elongation, the virtual instrument starts elongating the sample in steps of 20 μm until a preset value (F_{step}) is reached. Once this is reached, the VI stops the elongation and waits for the sample relaxation process to finish. The relaxation time for bovine pericardium samples was determined by a separated tests which is described in a following section. While the sample is relaxing, the virtual instrument launches 10 laser pulses with a fixed energy to observe the evolution of the spectral features during the relaxation process. Once the 10 laser pulses are lunched and spectra are register, the virtual instrument starts the next optical test by recording 10 images for each of the 4 different position of the CP. As in the first test with no elongation, 7 different pump energies are used to irradiate the sample in order to have enough information to calculate the emission threshold. Additionally, the VI acquires images of the two apertures slit for each of the pumping conditions. When the optical test is finished, the virtual instrument completes a cycle and starts the elongation again. A typical test comprises around 6 and 7 cycles and is mostly limited by the force that can be recorded by the load cell (8 N). When the test finishes, all the acquired data are recorded in a PC to subsequent analysis.

3.4. DATA ANALYSIS

Data analysis was performed in *Mathematica*. Mechanical data (force and displacement) were used to construct the stress-elongation ratio curve using the same procedure described in the previous chapter (see subsection 2.2.1). These curves give information about the macroscopic behavior of the tissue and are an important guide to understand the microscopic behavior of the samples. The spectra recorded allowed us to calculate the width of the random laser emission and the spectral energy density. Another important parameter analyzed during the tests was the peak wavelength of the emission, which was extracted from the recorded spectra and plotted as function either of the pump energy or the elongation ratio. Figure 3.5 shows a block diagram of the procedure followed for data analysis.

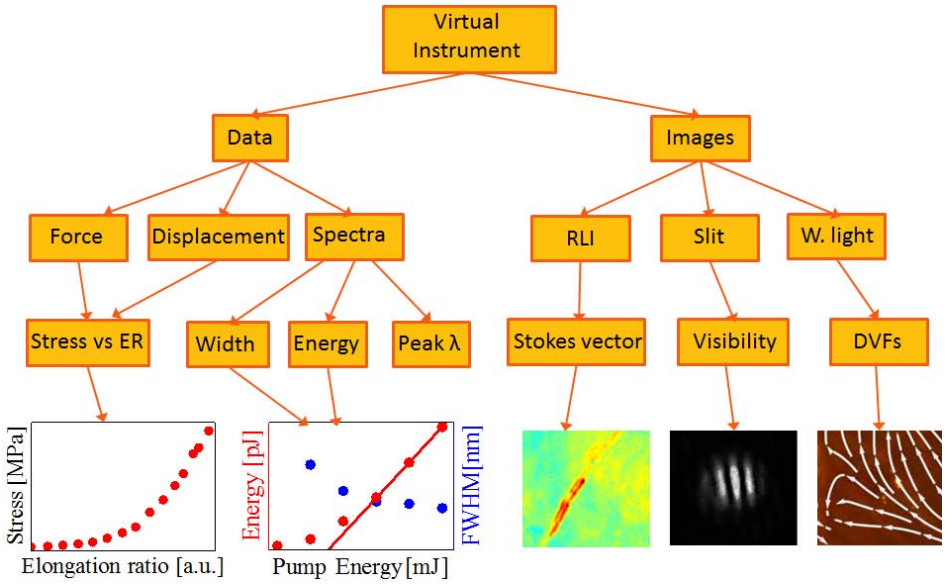

Figure 3.5. Block diagram of data acquisition and processing. The virtual instrument acquires images of the random laser emission (random laser imaging, RLI), custom-made two apertures slit and of the tissue with white light illumination. With the data recorded from the test, one can extract information such as elongation ratio, stress, width of the random laser emission, spectral energy density and peak wavelength.

Images of the random laser emission for 4 different positions of the CP were acquired in order to construct the Stokes vector of each pixel. In general, the Stokes vector provides information about the polarization features of the random laser emission, and the application of this technique in the field of biological based random lasers has not been explored up to date. The *Mathematica* notebook written for this purpose solves 1024 systems of 4x4 per each of the pump energies probed during each of the elongation cycles of the test. A detailed description of this calculation is presented in Chapter 4. Similarly, images of the slit were recorded for different pump energies and several elongation ratios. These images are acquired by a CCD camera separated 4.3 cm from a 5 x *Mitutoyo* objective. As we will discuss later, the main idea of the slits images is to obtain information about the degree of coherence of the random laser emission. Finally, white light illumination images were acquired in order to obtain the displacement vector fields in the same manner as reported in Chapter 2. We focus in this chapter on the results of the mechanical test along with the spectral analysis; in Chapter 4, we present the results concerning the Stokes vector analysis, digital image correlations and images from the custom made 2 apertures slit.

3.5. RANDOM LASER EMISSION IN BOVINE PERICARDIUM

Although the mechanism responsible for laser action in disordered materials is still subject of controversy, at least two descriptions explaining random laser action can be found in the literature. One of them points out that multiple scattering by itself can localize the light in random spatial cavities, which sustain random laser action [21]. These kinds of random lasers have been known in literature as coherent random lasers. Andreasen *et al* have shown in theoretical studies that multiple scattering disordered 2D materials sustain localized modes [21]. On the other hand, other authors explain random laser action as the result of an increase in the path length of spontaneously emitted photons within the active media due to multiple scattering [23]. This approach neglects the possibility of any degree of localization and is more related with the amplification of spontaneous emission (ASE).

In general, random lasers in which scattering cannot sustain localization have been known as incoherent random lasers.

A theoretical study of random lasers exceeds the scope of this work. Nevertheless, we have found two key features in the light collected from R6G immersed pericardium samples that lead us to consider the emission as random laser light: spectral narrowing and threshold behavior. In conventional lasers, the width of the laser line is mostly a function of the quality of the optical cavity. Commercial lasers can achieve laser linewidths of tenths of nanometer. Compared to this, light from R6G immersed pericardium samples is spectrally wide. However, when comparing with the photoluminescence spectrum of the R6G solution, the spectral narrowing is evident. Figure 3.7 shows intensity spectra for samples of R6G-glycerin solution and R6G immersed bovine pericardium.

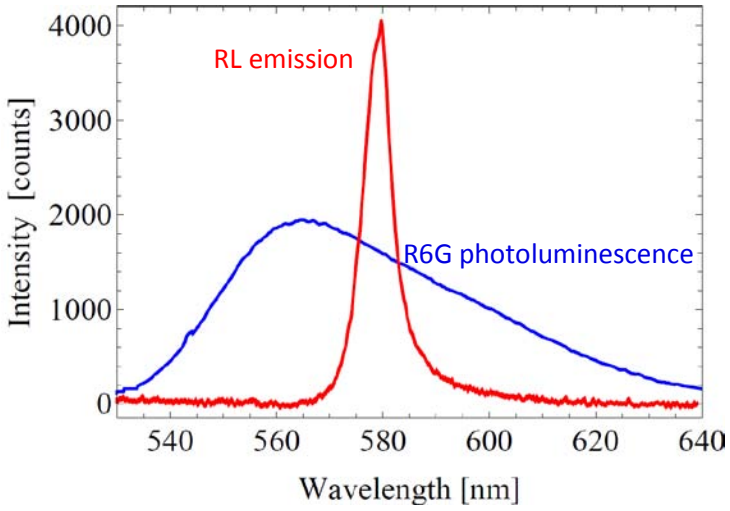

Figure 3.7. Blue line: photoluminescence spectra of R6G dissolved in glycerin. Red line: random laser emission spectra from a R6G immersed bovine pericardium sample.

The photoluminescence spectrum shown in Figure 3.7 is the same from Figure 3.1 and was acquired in a standard fluorescent measurement. The random laser spectrum was obtained from a sample prepared as detailed in section 3.3, and by pumping it with the same energy used to obtain the photoluminescence spectrum. As can be noticed in the

figure, the random laser spectrum is about ten times narrower than the photoluminescence spectrum. It is important to emphasize that no mirror or cavity were used in the setup to obtain the random laser spectrum. Moreover, the R6G solution from which the photoluminescence spectrum was recorded is the same solution in which tissue samples were immersed. In the visible region of the spectrum, collagen-based tissue acts predominantly as a scattering material [65]. Therefore, the dramatic change in the spectral width shown in Figure 3.7 is due to the incorporation of the active media into the scattering ensemble. Notice that the spectra of Figure 3.7 differ not only in width but also in the spectral energy content and in their peak wavelength. This in turn indicates that this narrowing effect is different than that observed in ASE, in which the spectral narrowing is centered at the same peak wavelength of the photoluminescence spectrum. As basically no other effect but scattering is present in the tissue-active media arrangement, we believe that the spectral narrowing can be associated with a feedback mechanism provided by the multiple scattering generated by the tissue.

In addition to spectral narrowing, a threshold-like behavior was also observed in the samples when pumped with different energies. As in any other laser system, the appearance of a threshold indicates that a certain amount of pump energy is needed to surpass the losses within the medium and start laser light emission. Above threshold, the relation between the pump energy and the emitted light remains linear until saturation is reached. Figure 3.8 shows the light emitted from the pericardium sample with R6G for different pump powers; notice that a linear behavior can be identified for the highest pump powers used for these measurements.

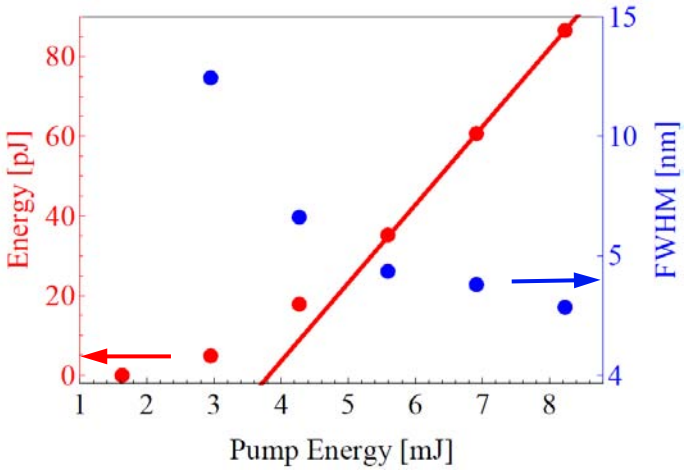

Figure 3.8. Emission energy as a function of pump energy obtained from a R6G immersed bovine pericardium sample. A threshold energy (3.8mJ for this case) after which a linear relation is obtained can be identified from linear fitting (red line). Blue points indicate the full width at half maximum (FWHM) showing the spectral narrowing of pericardium samples near the threshold.

Figure 3.8 shows a red solid line corresponding to a linear fitting from which a threshold of 3.8 mJ is obtained. Below this value, a non-linear behavior is observed in the curve; in contrast, for energies above the threshold a linear behavior is observed. Figure 3.8 further shows the full width at half maximum (FWHM) for each of the spectra recorded for the different pump energies. As can be seen in the figure, the FWHM decreases near the threshold reaching a minimum of approximately 4.5 nm with 8 mJ of pump energy. Notice that a FWHM of 4.5 nm represents a spectrum 10 times narrower compared to the fluorescence spectrum of the R6G showed in section 3.1. In general, the threshold-like behavior observed in these measurements is another key feature of the light emitted from pericardium samples that lead us to consider this effect as random laser action.

3.6. TENSILE TESTS AND SPECTRAL ANALYSIS

Once the key features of the emission from R6G immersed pericardium samples have been described, we analyze the spectral changes observed on these during the tensile tests. The main idea is to correlate the changes within the tissue induced by deformation with the spectral features of the random laser light. We started describing the

macromechanical behavior as registered by means of the load cell and LVDT. We then analyze the spectral features of the emission such as FWHM, peak wavelength and threshold energy.

3.6.1. Macromechanical behavior

The macromechanical behavior of the samples of bovine pericardium is given by the stress-elongation ratio curve. As in Chapter 2, we used equations 2.1 and 2.2 to calculate the elongation ratio for each sample. Four different samples were tested in these experiments: two were cut from the apical zone and two from the medial zone of the pericardium (see Figure 2.1). One of the apical samples was cut parallel to the base-apex axis ($A_{\parallel}$), while the other apical sample was cut perpendicular to the base-apex axis ($A_{\perp}$). Similarly, one medial sample was cut parallel to the base-apex axis ($M_{\parallel}$), and the other on perpendicular to the base-apex axis ($M_{\perp}$). The elongation-ratio curves corresponding to the four samples of these set of experiments are shown in Figure 3.9.

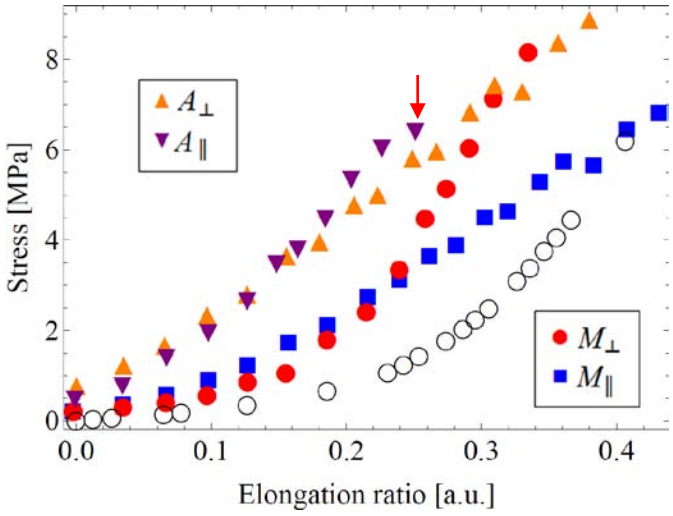

Figure 3.9. Stress-elongation ratio curves for different bovine pericardium samples. $A_{\perp}$: Apical sample cut perpendicular to the apex axis, $A_{\parallel}$: Apical sample cut in the direction of apex axis. $M_{\perp}$: Medial sample cut perpendicular to the apex axis, $M_{\parallel}$: Medial sample cut in the direction of apex axis. The red arrow indicates the point after which this particular sample presented rupture. The open black circles correspond to the bovine pericardium tensile test reported in reference [26].

Additionally to the tests performed in these experiments, Figure 3.9 also shows the test reported in reference [26] as open black circles. It is important to note that the test labeled with open black circles in Figure 3.9 correspond to a sample cut from a different pericardial sac. In subsequent sections, these data will help to compare the results of the data obtained in the present work. Figure 3.6 shows that for similar elongation ratios, apical samples registered higher stress values than medial samples. This is related to a more compact arrangement of fibers in the apical zone, and is also consistent with the results presented in section 2.3.1. (see Figure 2.9). Perpendicular and parallel samples from the apical zone showed a similar evolution as the elongation ratio increased; this behavior was sustained until reaching an elongation ratio of about 0.25 at which the parallel sample presented rupture (indicated with a red arrow in Figure 3.6) thus finishing the tests. On the other hand, medial samples exhibited a clearer distinction between the behavior of the parallel and perpendicular samples. After elongation ratios of approximately 0.24, the parallel sample registered higher stresses as the elongation ratio was increased. This behavior was also observed in the curves for the medial samples reported in the previous chapter and shown in Figure 2.9. Nevertheless, the differences between the stresses in the parallel and the perpendicular samples are larger in the medial curves shown in Figure 3.6. As pointed out previously, the samples used in the set of experiments of Chapter 2 and the samples for the R6G immersed tissue (Chapter 3) were cut from the same pericardium sac. Hence, the differences between figures 2.9 and 3.6 are the result of sample-to-sample variation present in the same tissue specimen.

In general, the medial samples cut parallel to the apex axis experienced less stress for similar elongation ratios than any other sample during the tensile test. These samples also supported the largest elongation ratios during the tests. This indicates that among the studied samples, the medial parallel samples minimize the energy needed to deform the tissue. Moreover, these results can help to obtain an insight of the collagen fiber alignment and the content of crimped fibers within the tissue. For elastomeric materials (such as pericardium), the stress-elongation ratio curve is a good mean to estimate the Young modulus (E) of the material by calculating the slope (G) of the linear region in the stress-elongation ratio curve (E=3G) [49, 66]. In collagen fiber based tissues, the slope in the

stress-elongation ratio curve is related with the alignment of collagen fibers in the loading direction [44, 50]. The region I in these kinds of curves also provides information because the values of elongation ratio in which the sample start the linear tendency is function of the content of wavy fibers within the tissue [45]. Wavy fibers uncrimp with low stress values allowing large deformations in the first region of the stress-elongation ratio curve [50].

Comparing the results of the 4 samples studied here with the data from the mechanical test of reference [26] (open circles in Figure 3.9), the curve may corresponds to a medial sample because the curve exhibits large elongation ratios associated to small changes in stress. The pericardium sample of reference [26] needed less stress than any of the four samples studied here to sustain similar elongation ratios. For these complex materials, a different microstructure (i.e. bovines of different ages) can lead to a dramatic difference in the mechanical behavior and thus in the optical properties of the tissue. In the next sections we will investigate the influence of the mechanical tests in the spectral features of the random laser emission generated within the pericardium tissue samples.

3.6.2. Spectral features of the random laser emission from the tissue samples

The spectral information was extracted from data recorded by a solid-state, high-resolution (0.2 nm) spectrometer (*Ocean Optics HR4000*) and controlled by means of the virtual instrument. Adjustments on the spectrometer settings were made using 8 mJ pump pulses prior the tests in order to avoid saturation of the CCD array of the spectrometer. Spectra for different pump powers and elongation ratios were recorded during the tests; representative spectra for each sample are shown in Figure 3.10.

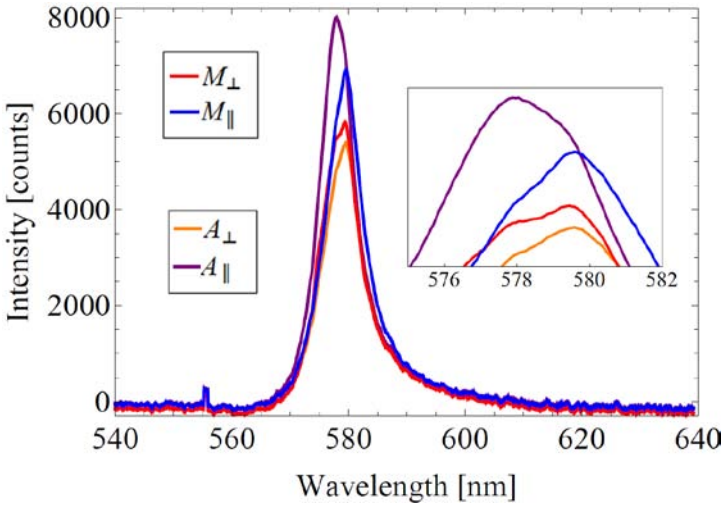

Figure 3.10. Representative spectra of the laser emission obtained from the pericardium samples. The labeling of the curves is the same as that for Figure 3.9. The inset shows details of the peaks of the spectra in a narrower scale.

Although the spectra shown in Figure 3.10 seem to be very similar, the intensity, FWHM and peak wavelength are different for each curve. The spectra shown in the figure correspond to different samples under no elongation and for a pumping energy well above the threshold. For each acquired spectrum, the peak wavelength, spectral width (FWHM) and the spectral energy density are analyzed under different elongation ratios. In conventional lasers, these parameters give information about the cavity length, losses and the quality of the mirrors. However, in random laser theory is not yet clear what is the relation between the peak wavelength and the width of the emission with the scattering particle density and the intrinsic losses. In this section, we aim to relate qualitatively the spectral features of random laser emission with the mechanical properties of the tissue; a theoretical formalism is beyond the scope of this work.

We start by plotting the FWHM of the samples as function of the elongation ratio in Figure 3.11. This parameter is commonly used in conventional lasers as a standard for measuring their spectral width; typically, commercial lasers have a FWHM of tenths of nanometer.

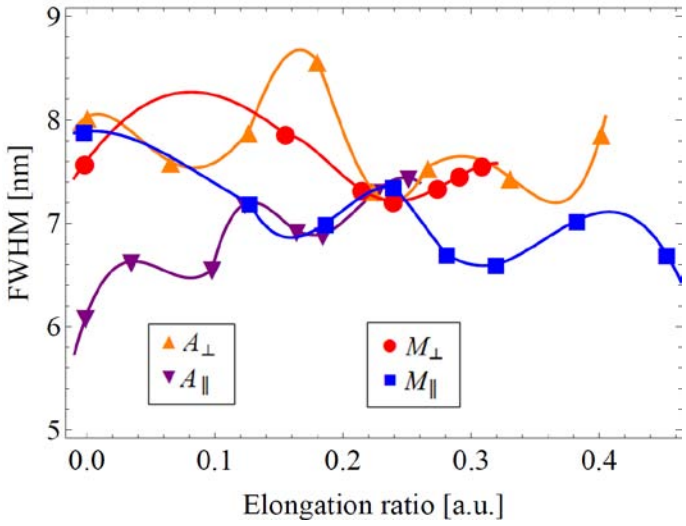

Figure 3.11. FWHM as a function of elongation ratio obtained from the emission of the tissue samples. Circles, squares and triangles represent experimental data; solid lines are included as a guide to the eye.

As in previous figures, $A_\perp$ corresponds to an apical sample cut in the perpendicular axis, $A_\parallel$ correspond to an apical sample cut in the parallel axis; while $M_\perp$ and $M_\parallel$ correspond to medial samples cut along the perpendicular and parallel axes, respectively. Figure 3.11 shows that all values oscillate between 6 and 9 nm, furthermore, no clear tendency can be distinguished for the FWHM as the elongation ratio increases. In general, the change in FWHM does not exceed 2 nm in any of the samples. This is a very low variation range comparing compared with to previous reports in bovine pericardium random lasers [26]. During the mechanical test reported in reference [26], the FWHM change from 4nm at the beginning of the test to 16nm at the end of the test. This range of FWHM spans out the scale of Figure 3.11 indicating the differences in microsctructure between both pericardium specimens. The structural difference between samples is also evident from stress-elongation curves (see Figure 2.9). Nonetheless, several differences between the experiments in reference [26] and those reported here can be pointed out. First, the thicknesses of the samples are very different (0.41 mm in reference [26]-0.26 mm in the present samples). Sample manipulation was also different; while the samples presented here were stored for no more than 36 hours, the samples used in reference [26] were stored at least 6 months before the tests. More importantly, the collection of the light

emitted from the samples was also different for both sets of experiments. For the experiments reported in this work, the light was collected via a microscope objective in a forward direction, while in reference [26] the light was collected in an oblique fashion by means of an optical fiber. It has been demonstrated that the spectral features of random laser light strongly depend on the angular position of the collection device [24]. Even though this was not an expected result, the relative invariance of FWHM over elongation ratio presented in all samples could help to advance in the understanding of the inner tissue structure responsible for random laser emission.

Another important parameter in the spectral features of a random laser is the peak wavelength. In order to analyze the change in peak wavelength during the mechanical test, we defined a normalized shift as:

$$Normalized\_Shift = \frac{\lambda_{peakN} - \lambda_{peak0}}{FWHM_N} \qquad 3.1$$

Here, λ_{peakN} is the peak wavelength of the spectrum under analysis, λ_{peak0} is the peak wavelength of the reference spectrum, obtained from the same sample but with no deformation applied, and $FWHM_N$ is the spectral width. Thus, the normalized shift is the number of widths (FWHM) that a spectrum deviates from the spectrum recorded with the tissue sample subjected to no elongation. For all cases, special care was taken to analyze a spectrum for pump energies above the threshold for each elongation ratio. Further discussion regarding the random laser threshold is included in the last paragraphs of this section. Figure 3.12 shows the normalized shift as function of elongation ratio for the different tissue samples.

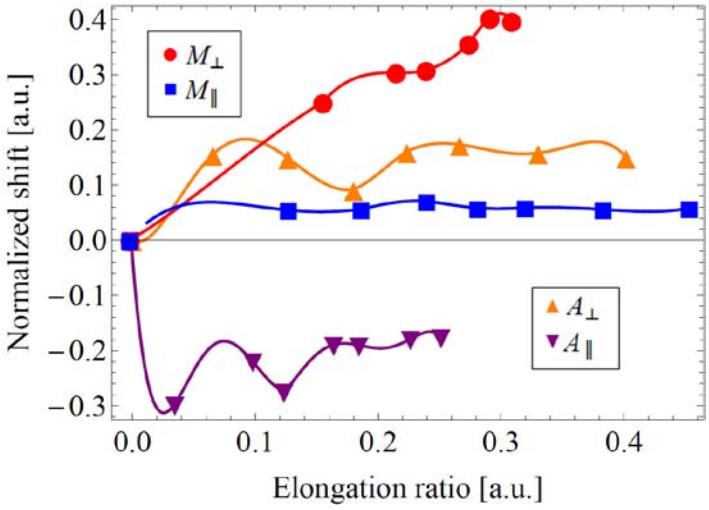

Figure 3.12. Normalized peak wavelength shift calculated as in expression 3.1 versus elongation ratio for the apical and medial pericardium samples. Solid lines are merely a guide to the eye.

Tunability is an effect that has been previously observed in random lasers [3, 4, 67, 68]. The mechanisms used to adjust the peak wavelength include temperature, liquid crystal ordering and mechanical deformation, among others. In particular, reference [67] reports a tunable range of ~10 nm, which also matches the tuning capabilities obtained by means of scatterer density variations in SiO_2 based random lasers [69]. A tuning range of approximately 10 nm corresponds to 2 units of the normalized shift as defined in Equation. 3.1. Hence, the tuning range presented in Figure 3.12 is very small compared to those reported previously [67, 69]. As seen in the plots, 3 of the 4 samples experienced shifts of about 0.2 during the tests. Noticeably, the medial sample ($M\perp$) presented the highest shift reaching a value of 0.4. This sample also showed a tendency to increase the shift as the elongation ratio was increased. In contrast, the remaining three samples showed a plateau that is reached in the first steps of the tests. After reaching the plateau, only very small changes in the peak wavelength were registered as the elongation ratio increased.

These results along with the information of the spectral widths would lead to the affirmation that no changes in scatterer density occur during the bovine pericardium tensile tests. Nevertheless, it is clear from the results of Chapter 2 that changes in the scattering

features are observed when the tissue samples are subjected to uniaxial tension. Furthermore, it is well known that uniaxial tension in collagen-based tissue tend to align collagen fibers [27, 30, 31, 35, 37, 50]. This fiber alignment has been related with an alteration in the volumetric scatterer density [19, 26]. The reason for these unexpected results might be underlain in the hierarchy structure of collagen.

The mean free paths (MFP) registered in the experiments of Chapter 2 are in the order of 10-25 μm, which may reasonably represent the mean separation between collagen fibers as these superstructures have diameters ranging from 100 μm to 1 mm [50]. Nevertheless, the inner structure of fibers is a compact arrange of fibrils of tenths of microns [28, 50]. If the elongation ratio changes the MFP of the EBS test, but does not provide tuning in the random laser emission, could lead us to assume that the laser emission is generated primordially inside the collagen fibers, and not among the fibers as we first had expected. Random laser emission can be sustained inside collagen fibers because they are made of structures with an adequate size to exhibit high scattering effects in the visible region. Moreover, the main mechanisms in fiber reordering in collagen-based tissues are fiber uncrimping and fiber aligning [50]. The structural (inner) change in collagen fibers appears under high deformation conditions, when most of the fibers are already aligned. This would explain not only the plateau observed in Figure 3.12, but would also suggest that the peak wavelength of each sample is an indicator of the mean diameter of the collagen fibers, where random laser modes would predominantly appear. If this is the case, the scenario would be much more complex than an ensemble of cylindrical scatterers being aligned as the elongation ratio increases. This will give rise to a distribution of random laser modes along each fiber. Instead of being determined by the degree of anisotropy between the collagen fibers, these modes would be characterized by the density and diameter of the fibers. According to this description, the random modes corresponding to different fiber diameters would overlap in the laser output giving rise to a multimode spectrum that cannot be resolved with the actual experimental setup. Moreover, if the random laser action can be sustained inside individual collagen fibers, several volumetric modes may arise in each collagen fiber. A rough estimation on the number of modes in a collagen fiber can be computed using the Rayleigh–Jeans formula [70].

$$N = 4\pi \frac{V}{\lambda_{peak}^4} FWHM \qquad 3.2$$

In Equation 3.2, $FWHM$ is the spectral width of the emission, λ_{peak} is the central wavelength of the emission, and V is the pumped volume of the gain medium. Considering a single pumped fiber with a diameter of 20 μm and 10 mm long, (which are representative values for collagen fibers in collagen based tissue [50]) and taking into account the spectral features observed experimentally in this work, the number of modes in such a fiber would be:

$$N = 4\pi \frac{\pi(10\times10^{-6})^2 \times 10\times10^{-3}}{(580\times10^{-9})^4} 10\times10^{-9} \approx 1\times10^{6}$$

A fiber of 0.2 x 5 mm lies within the pumped area of the laser spot (~1 cm diameter). All of the 10^6 modes along with the corresponding modes of the rest of the collagen fibers pumped would lase in a spectral width of ~10 nm, making impossible the task of identifying each lasing mode with the current experimental setup. A consequence of this enormous number of modes in a random laser would be a low coherence because one fiber usually interacts with a close vicinity of adjacent fibers [50]. A corroboration of this statement is presented in Chapter 4.

Another parameter of the random laser emission that is strongly linked with the density of scatterers in a disordered medium is the emission threshold. This indicates the pump energy required to overcome the losses and start laser action. In conventional lasers, the losses are a function of the cavity efficiency, which means that any scattering event inside the cavity leads to a detrimental perturbation in the laser emission. Despite the lack of a formalism linking the threshold with the scattering properties, it is clear that both are related, because for random lasers the scattering is the feedback mechanism. We analyzed the changes in the laser threshold during the tensile test for each of the pericardium samples; the results are summarized in Figure 3.13.

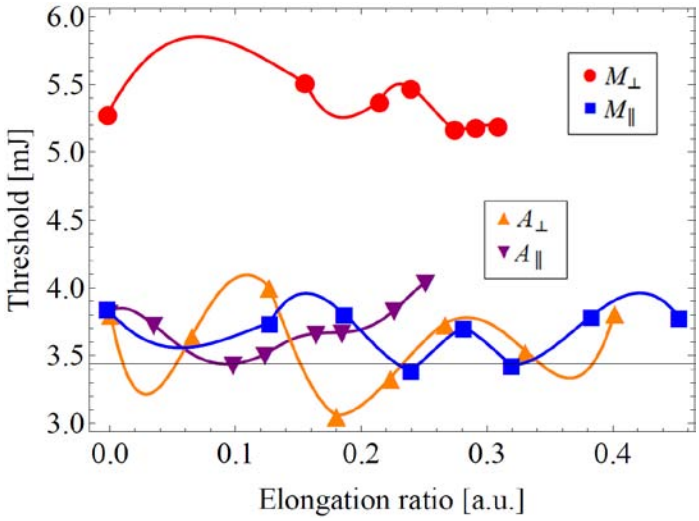

Figure 3.13. Threshold for the random laser emission as function of elongation ratio for the pericardium tissue samples. Solid lines are merely a guide to the eye.

The thresholds shown in Figure 3.13 were calculated using a linear fit for the last points of the output energy as a function of pump energy (see Figure 3.8). From the fitting expression, the crossing with the pump energy axis can be readily obtained and this value provides an estimate for the threshold for laser emission. As seen in Figure 3.13, the threshold did not exhibit a clear tendency as the elongation ratio was increased. Three of the four samples exhibited thresholds between 3 and 4 mJ during the tests. The medial sample cut perpendicular to the apex axis showed a higher threshold (~5.3 mJ) than those obtained for the other samples. Interestingly, this sample is the same showing the highest normalized shift (see Figure 3.12).

Notice that in all cases, the threshold remained relatively invariant during the tensile tests. This further supports the assumption that the random laser emission for these samples is generated inside the collagen fibers. Because the elongation ratio has a small effect on the inner structure of the collagen fibers, the losses for the random laser modes due to scattering will remain constant as the elongation ratio increases. Following this reasoning, higher thresholds would indicate a smaller concentration of fibrils inside the collagen fibers, as less scattering leads to less localization of random laser modes [21].

Higher thresholds may also be explained by a high content of wavy fibers, such as for the $M_{\perp}$ sample. Wavy or crimped fibers are less dense fibers, which can fold in order to form helical, sinusoid or zig-zag structures [50]. As seen in Figure 3.9, the $M_{\perp}$ sample presented a more pronounced non-linear behavior; this is a macroscopic indicator of the wavy fiber content in the sample, because uncrimping of these fibers is the first mechanism of fiber interaction when a collagen based tissue is deformed [50]. This would also explain the tendency seen in Figure 3.12, where an increase in elongation ratio results in a small increase in the normalized shift for the $M_{\perp}$ sample. Hence, this could also indicate that a portion of the wavy fibers is being straightened in the load direction. Nevertheless, this small proportion of elongated wavy fibers is even smaller when compared to the overall number of fibers, and does not affect substantially the emission threshold as elongation ratio increases.

A less tight arrangement of fibrils allows for the fiber to curl and form several 3D super structures [27, 44]. These kinds of fibers can straighten with low values of load and return to the crimped formation giving elastic properties to the tissue at the microscale. The determination of the proportion of wavy and straight fibers in each section of a tissue, such as the bovine pericardium, would require extensive work with microscopy techniques such as SEM and TEM. In general, the super structures formed by wavy fibers are difficult to observe even with these techniques because the sample preparation procedure (dehydration and vacuum conditions) usually collapses the fibers from its original arrangement [36, 44].

3.6.3. Spectral evolution during sample relaxation

When a collagen-based tissue is subjected to a tensile deformation, the collagen fibers tend to reorder in such a way to minimize the stress applied to sustain the deformation [41, 45]. The time lapse in which the fibers stop reordering is known as relaxation time and depends mostly on the predominant collagen type of the tissue, the mesh structure of the collagen fibers and the amount of stress applied [28, 30]. The virtual instrument programmed for these experiments acquire random laser data during the

relaxation process of the samples. 10 Pump pulses were launched every 15 seconds after stopping the elongation of the samples. For each pulse and for each step of the test, the resulting emission spectrum was acquired and stored for subsequent analysis. The pump energy selected for these measurements was close to the threshold value because the FWHM and the energy density are typically more sensitive to fluctuations under these pumping conditions. Figure 3.14 shows the set of spectra of the $A_{\parallel}$ sample after being subjected to an elongation ratio of 0.19.

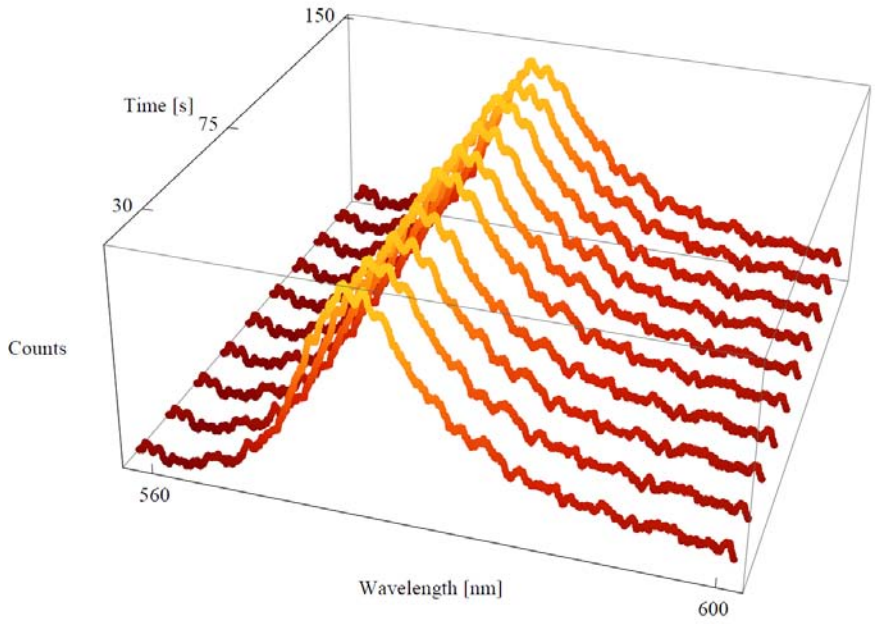

Figure 3.14. Time evolution of the emission spectrum of the random laser emission obtained from the $A_{\parallel}$ sample. The plots show spectral changes during sample relaxation after being subjected to a 0.19 elongation ratio.

Figure 3.14 shows very similar spectral features for different times. Comparing with Figure 3.10, Figure 3.14 shows wider spectra and more spectral features within the peak wavelength. This is because the pumping conditions for both set experiments are different: while Figure 3.10 was obtained for pump powers well above the threshold, spectra from Figure 3.14 correspond to a pumping energy near threshold. The spectral features around the peak wavelength can be related to mode competition among the ensemble of several random modes inside the tissue samples.

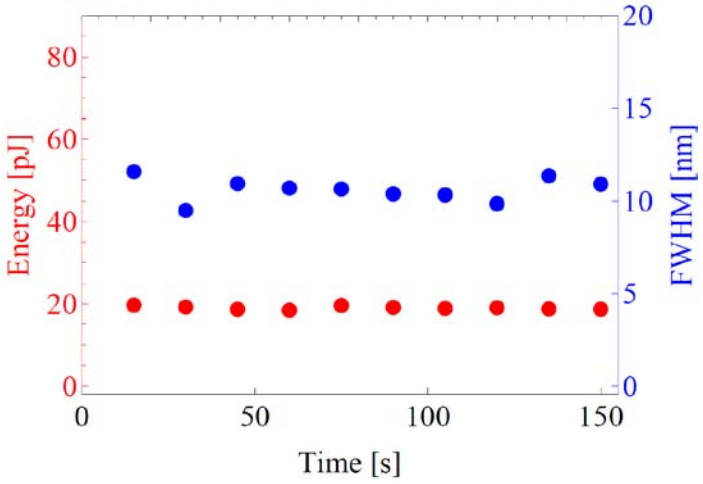

Figure 3.15. FWHM and energy density of spectra from Figure 3.14 as function of time.

From the spectra shown in Figure 3.14, the evolution of the FWHM and the energy density during the relaxation process can be plotted as function of the time. As seen in Figure 3.15, the FWHM and the energy density remained almost constant during relaxation of the sample. This also supports the assumption that random laser emission generates primarily inside the collagen fibers. Similar results were obtained during relaxation when the samples were subjected to higher elongation ratios.

All the experimental results provide evidence to consider the light emitted from the bovine pericardium samples as random laser light. The main spectral features of the light emitted from the samples showed an almost constant behavior in terms of the elongation ratio. These features seem to suggest that the emission is generated from inside the collagen fibers themselves. In the following chapter, the images recorded in this set of experiments are analyzed by means of polarization analysis (Stokes vector imaging) and digital image correlation. The main idea is to correlate the spatial features of the random laser emission with the information of the displacement vector fields obtained by digital image correlation. This provides complementary information to the macromechanical behavior and the spectral features of the random laser emission.

CHAPTER 4

IMAGE ANALYSIS OF RANDOM LASER EMISSION

In what follows we show the results of applying imaging methods on the random laser emission from the tissue samples during the tensile test. We further analyze consecutive white light images yielding the displacement vector fields on the tissue resulting from the tensile test. The alternation of white/laser light along with the notch filters made possible to acquire white light images and random laser light images during the same tensile test. As we will see in the following subsections, this lead us to identify zones of high intensity of random laser emission associated with specific fibers seen in the white light images. The displacement vector fields confirm again the hyperbolic pattern characteristic of these kinds of tissues undergoing uniaxial tension and show some degree of correlation with the random laser emission.

4.1. STOKES VECTOR IMAGING OF RANDOM LASER EMISSION

The Stokes vector representation of a light beam associates four real numbers with the intensity of the different polarization components of the beam. Under this representation, the polarization ellipse is described in terms of intensities, which are observable quantities and allows for measuring the vector components by means of adequate polarizers. The derivation from the polarization ellipse to the Stokes vectors can be found elsewhere [43]. In particular the four components of the Stokes vector can be defined as follows:

$$S_0 = E_{0x}^2 + E_{0y}^2 \quad 4.1$$

$$S_1 = E_{0x}^2 - E_{0y}^2 \quad 4.2$$

$$S_2 = 2E_{0x}E_{0y}\cos\delta \quad 4.3$$

$$S_3 = 2E_{0x}E_{0y}\sin\delta \qquad 4.4$$

Here, E_{0x} and E_{0y} are the intensities in the x and y axes, respectively, and δ represent the phase difference between the x and y component of the beam. The first component, S_0, is the total intensity of the beam. The second component, S_1, describes the contribution of the horizontal or vertical linear polarizations. The third component, S_2, stands for the amount of linearly polarized light, oriented either at +45 or -45 degrees. Finally, S_3 describes the amount of right or left circularly polarized light. Additionally, these 4 components satisfy the relation:

$$S_0^2 \geq S_1^2 + S_2^2 + S_3^2 \qquad 4.5$$

The equality sign applies for fully polarized light and the inequality sign applies for partially polarized or unpolarized light. These 4 parameters describe completely the state of polarization of a light beam and can be measured by different methods involving polarizers and wave plates. In particular, the circular polarizer method is adopted as described in [43] to analyze the polarization of random laser emission. One of the circular polarizers used in previous experiments (see chapter 2) was used as a polarization analyzer. The circular polarizer is positioned between the imaging apparatus and the sample, as shown in Figure 4.1 a notch filters is also used to block residual pump.

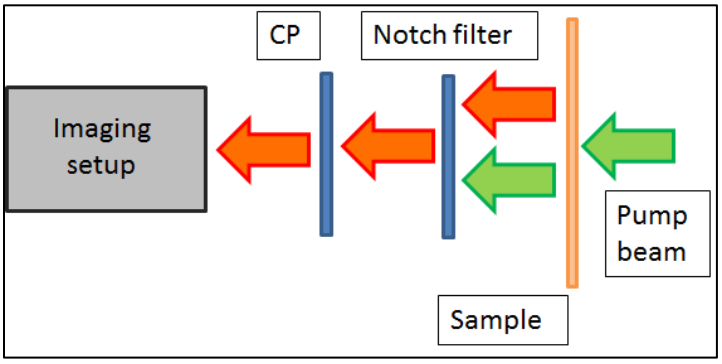

Figure 4.1. Schematic representation of the experimental setup (detail). A 532 nm pump beam illuminates the sample. Residual pump and the random laser emission at 580 nm reach the notch filter, but the residual pump is blocked by the notch filter. The circular polarizer (CP) is used to analyze the polarization of the random laser emission.

The polarization state of the input beam $\mathbf{S_{in}}=[S_{0in}, S_{1in}, S_{2in}, S_{3in}]^T$ multiplied by the Müller matrix of the circular polarizer yields the output state of polarization, i.e. :

$$\mathbf{S_{out}} = \mathbf{CP_n} * \mathbf{S_{in}} \qquad 4.6$$

Here, $\mathbf{CP_n}$ stands for the Müller matrix of the circular polarizer in one of the 4 positions used in these experiments. With this procedure one can relate the total intensity of the output state of polarization with a function of the 4 Stokes components of the original beam generated inside the tissue sample: $S_{0out}\ (S_{0in}, S_{1in}, S_{2in}, S_{3in})$. Upon adjusting the circular polarizer, one can obtain three additional expressions and solve a 4 x 4 system for each pixel of the CCD camera. As pointed out in previous sections, the computational calculations were performed with *Mathematica.*. The Stokes parameters (S_1, S_2, S_3) were normalized with respect to the total intensity S_0 and were obtained for different pumping conditions and different elongation ratios. It is important to note that the polarization of the pump beam was fixed for all the experiments, as no polarization optics were used at the output of the pump laser. Figures 4.2 to 4.5 resumes the results of Stokes vector imaging for the 4 samples studied with a fixed and null elongation ratio (step zero of the test) and different pump energies.

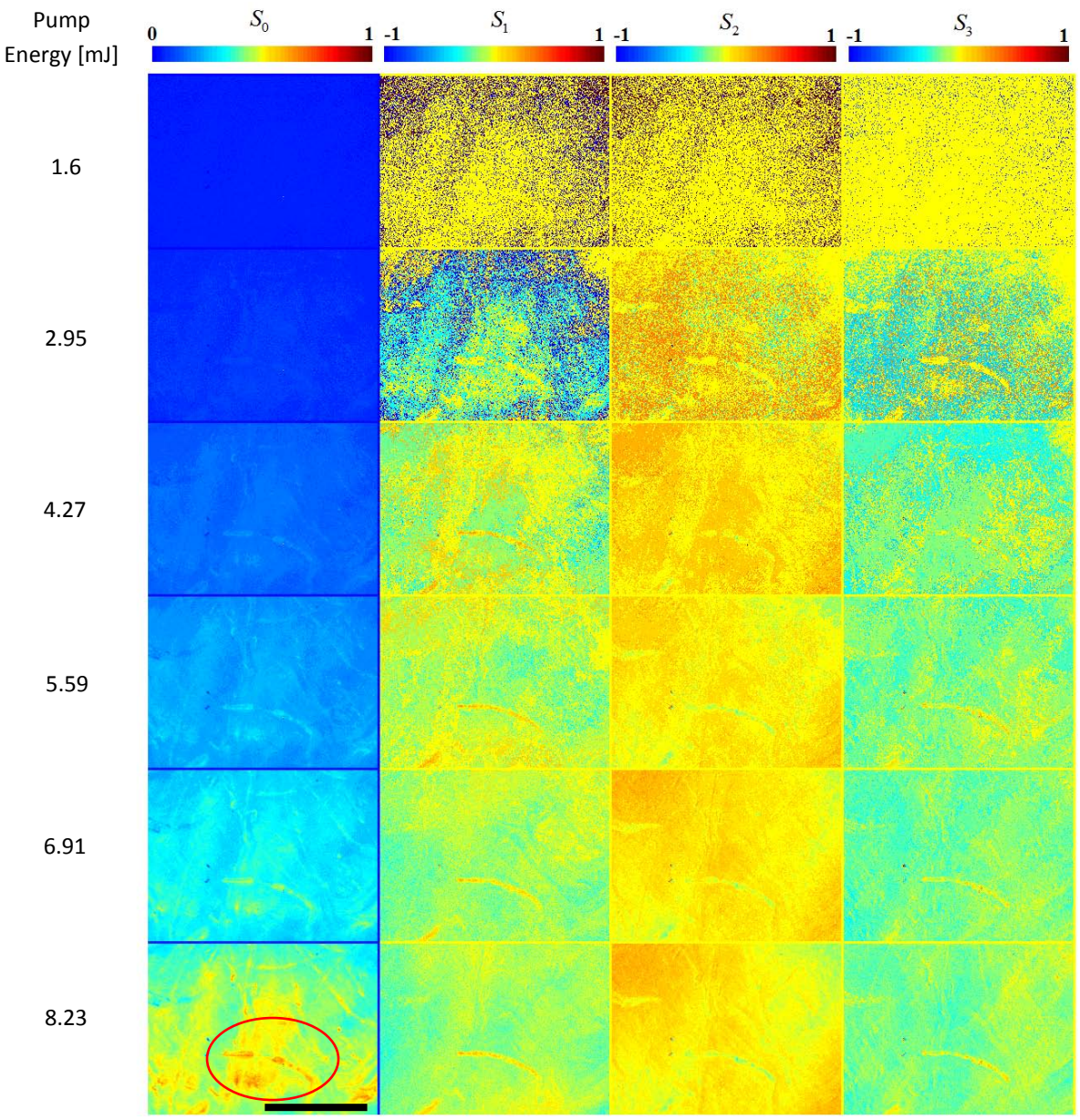

Figure 4.2. Stokes vector imaging for the $A_{\parallel}$ sample without deformation. The columns correspond to the 4 Stokes parameters and each row corresponds to different pumping conditions. The upper row corresponds to the lowest pump energy while lower row correspond to the highest pump energy. The red solid line indicates the laser threshold energy. The red oval in the bottom left images indicates some fiber-like features (see text for details). The scale bar corresponds to 1mm.

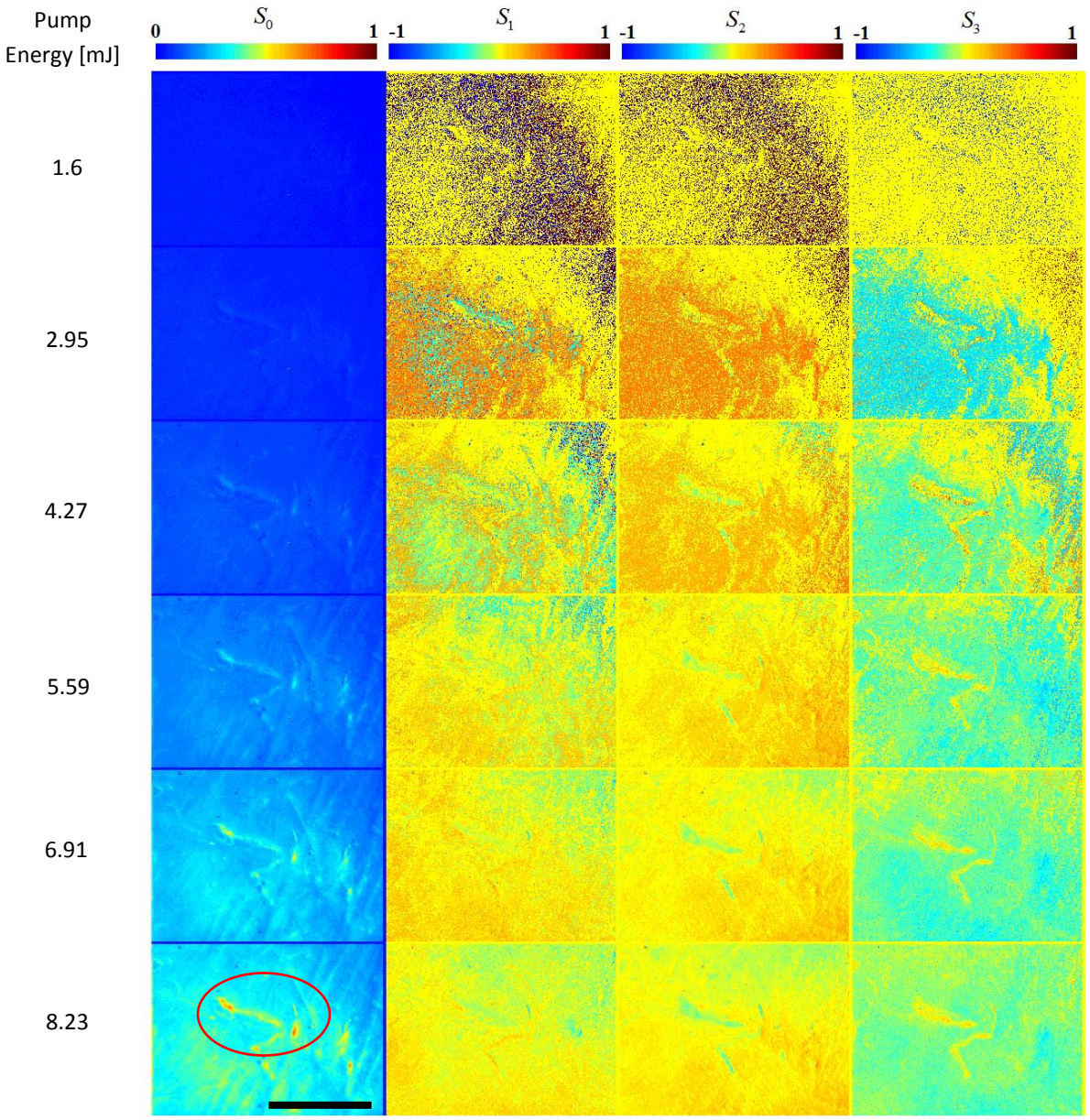

Figure 4.3. Stokes vector imaging for the $A_{\perp}$ sample without deformation. The columns correspond to the 4 Stokes parameters and each row corresponds to different pumping conditions. The upper row corresponds to the lowest pump energy while lower row correspond to the highest pump energy. The red solid line indicates the laser threshold energy. The red oval in the bottom left images indicates some fiber-like features (see text for details). The scale bar corresponds to 1mm.

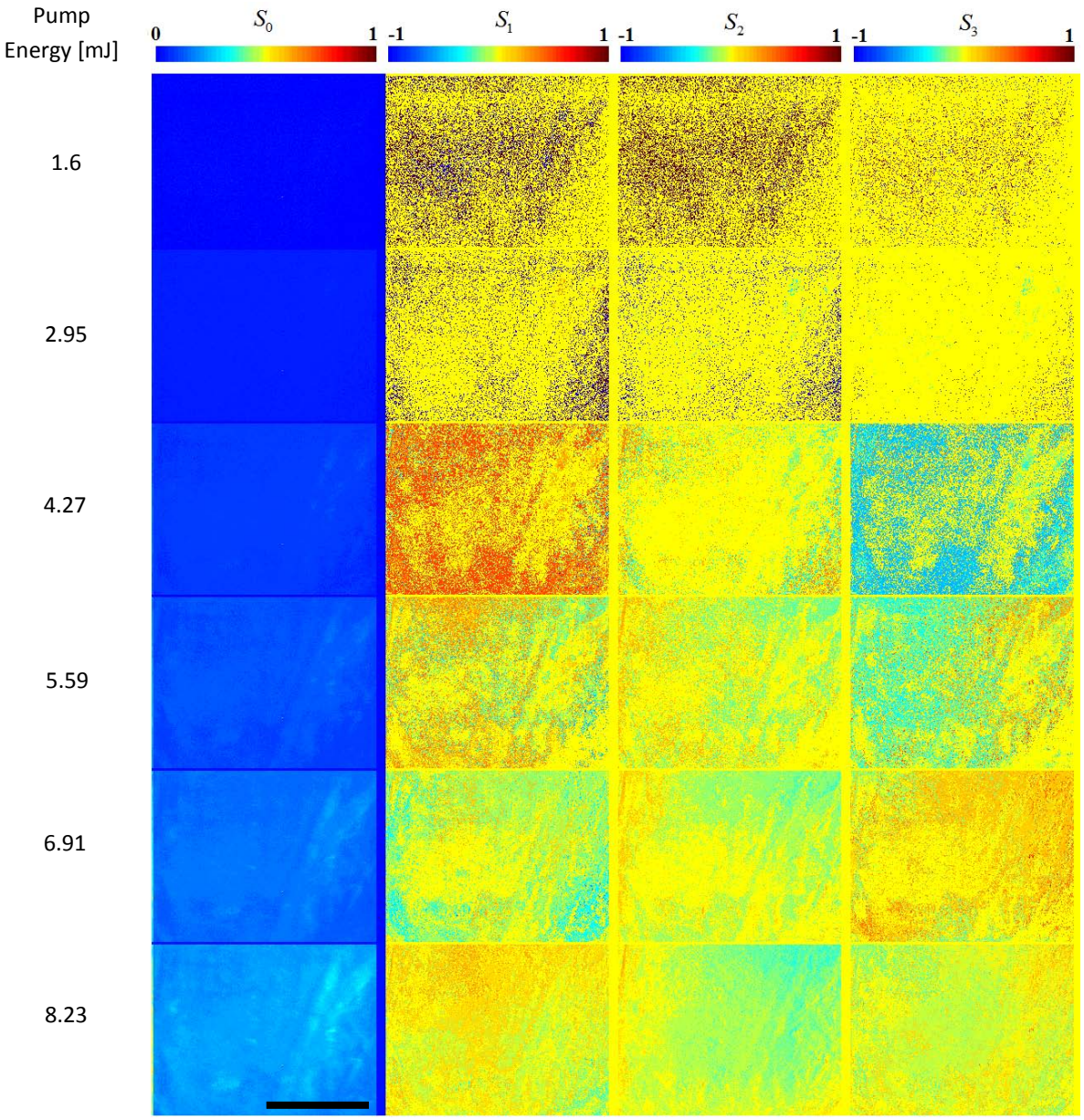

Figure 4.4. Stokes vector imaging for the $M_{\parallel}$ sample without deformation. The columns correspond to the 4 Stokes parameters and each row corresponds to different pumping conditions. The upper row corresponds to the lowest pump energy while the lower row corresponds to the highest pump energy. The red solid line indicates the laser threshold energy. The scale bar corresponds to 1 mm.

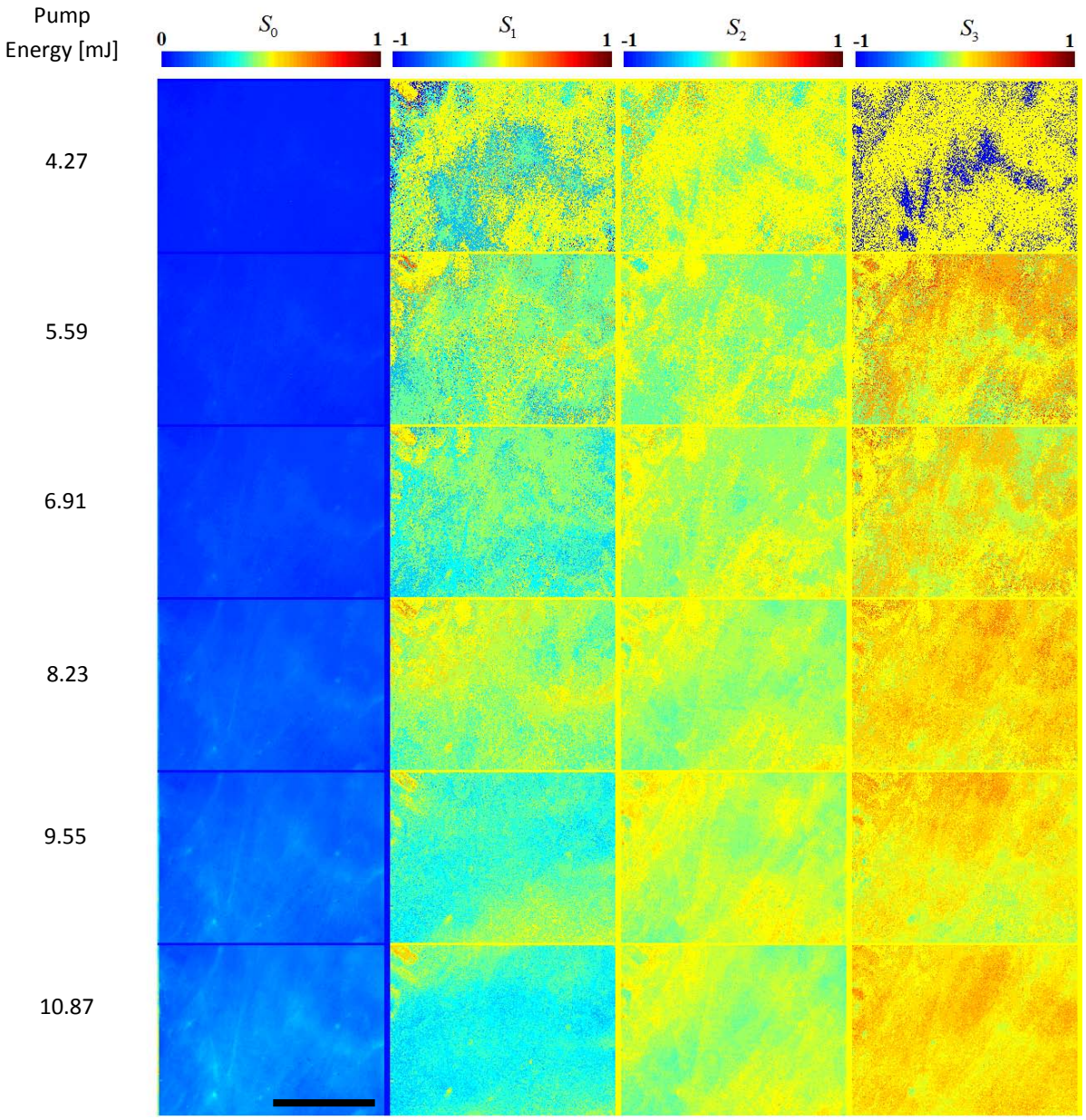

Figure 4.5. Stokes vector imaging for the M⊥ sample without deformation. The columns correspond to the 4 Stokes parameters and each row corresponds to different pumping conditions. The upper row corresponds to the lowest pump energy while the lower row corresponds to the highest pump energy. The red solid line indicates the laser threshold energy. The scale bar corresponds to 1 mm.

In general, figures 4.2 to 4.5 show a changing tendency for all the Stokes parameters; these seem to evolve from a noisy-like behavior for low pump energies to more

homogeneous and defined images for higher pump energies. In particular, this change is more evident for the images obtained before and after reaching the emission threshold. Once the threshold is reached, the changes in the Stokes parameters are less abrupt. Notice that figures 4.2 to 4.5 collect the information of the four samples with no elongation. Similar images were obtained for all samples, each of them under different elongation conditions. A similar evolution, from noisy to better-defined images can also be observed for the rest of the elongation conditions. This is expected since below threshold, the dominant emission process is spontaneous emission, which is in general randomly polarized; once the threshold energy is surpassed, stimulated emission dominates the radiative process. The evolution of randomly polarized light with low pump energies to a more defined map of polarized light with higher pump energies provides further evidence of the random laser emission obtained from these samples. As in the Müller matrix images shown in Chapter 2, the images in figures 4.2 to 4.5 exhibit borders with a fixed zero value. These zero values are observed in the images as dark blue margins in the upper and right borders in the case of the S_0 images; and as bright yellow margins in the upper and right borders in the case of the S_1, S_2 and S_3 images. The zero value margins were used as a numerical and visual reference in the subsequent analysis. The margin was also useful when spatially shifted images needed a manual center to fit the field of view used in previous images.

The bottom left corner of Figure 4.2 shows the total intensity (S_0) for the condition of highest pump energy for the $A_{\parallel}$ sample. This image shows that the highest intensity is detected in elongated curves that resemble the shape of a superficial fiber. Furthermore, similar fiber-like structures can also be seen in the S_0 parameter of the bottom left corner image in figures 4.2. Fiber-like features in the total intensity images of the random laser emission represent the ultimate evidence that stimulated emission within these samples is being generated inside the collagen fibers. This further support our previous suppositions based on the spectral information obtained from the light emitted from the samples. The bottom left corners of figures 4.2 to 4.5 also show that the highest intensity distribution is obtained for the apical samples, and the lowest intensity distribution correspond to the $M_{\perp}$ sample. This sample in turn, is the sample with the highest emission threshold (see Figure

3.12), further corroborating that in terms of laser operation, the $M_{\perp}$ sample is the less efficient light emitter.

Figures 4.2 and 4.3 show a tendency for the apical samples to exhibit linearly polarized states (see the second and third columns) and lower components of circularly polarized light (see the fourth column). On the other hand, a higher proportion of circularly polarized light is observed in the medial samples, particularly in the $M_{\perp}$ sample. This can be attributed to a higher content of less dense and more disordered microfibers in medial samples, which will tend to maintain the chiral nature of the collagen molecule [28, 59]. It is important to note that this work constitutes the first systematic study of random laser emission in collagen fiber based tissue, and is difficult to understand the influence of all the variables involved in such a complex system. Nevertheless, all the information gathered from our experimental results can serve as a starting point for advancing in the understanding of random laser emission in biological tissue.

In order to study the effects of the deformation imposed by the tensile test on the polarization features of random laser emission, the images corresponding to the highest energies for each step of the mechanical test were compared. The selection of the results for the highest energy guaranties that the random laser emission is above the threshold and thus laser noise fluctuations are minimized. Figures 4.6 to 4.9 show the Stokes vector images for the highest energies probed in each step of the tensile test for all the tissue samples.

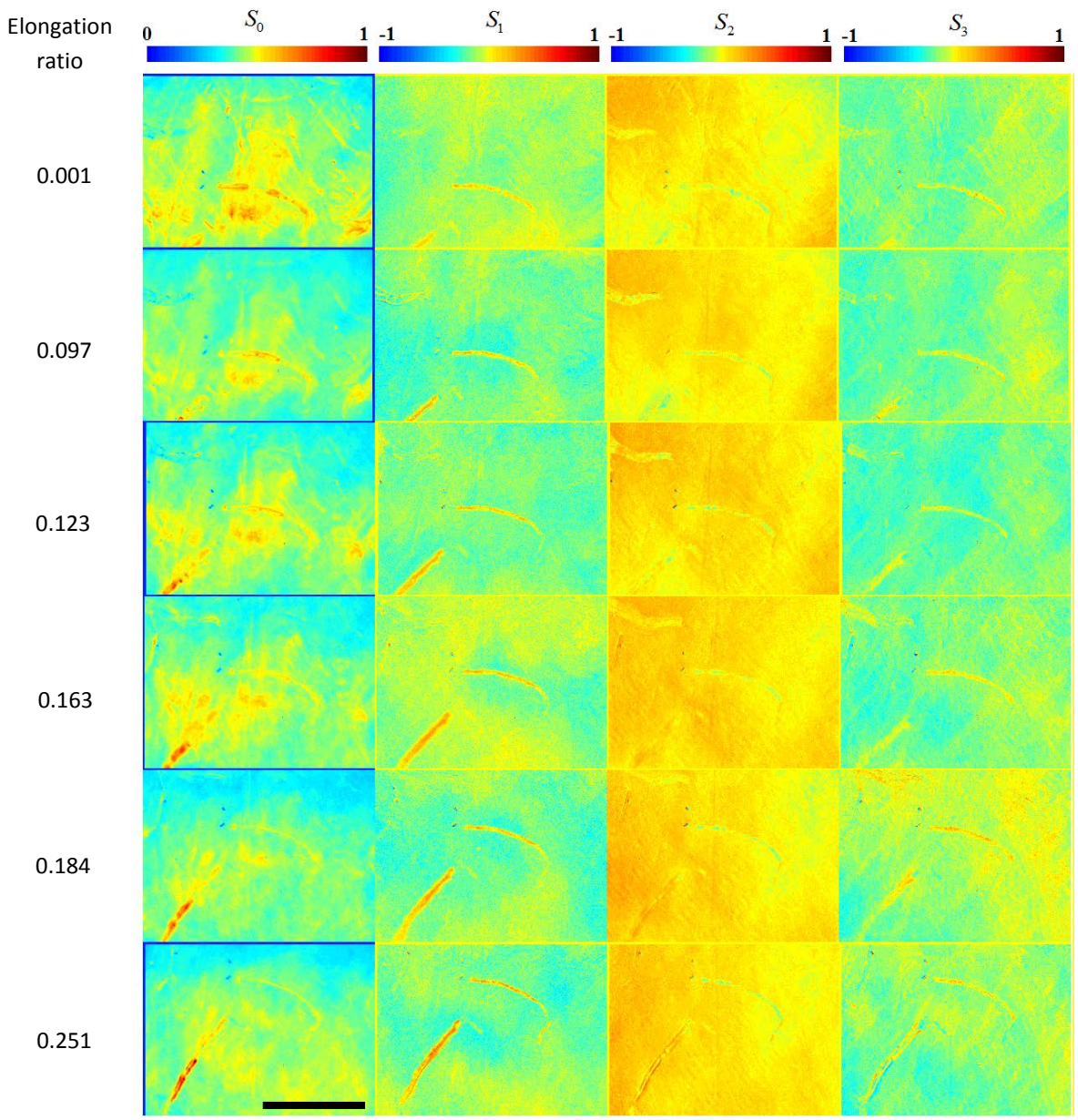

Figure 4.6. Stokes vector imaging for the $A_{\parallel}$ sample for the highest energies probed and for different elongation conditions. The columns correspond to the 4 Stokes parameters and each row corresponds to different elongation conditions. The pump energy was 8.23 mJ for all rows. The scale bar corresponds to 1 mm.

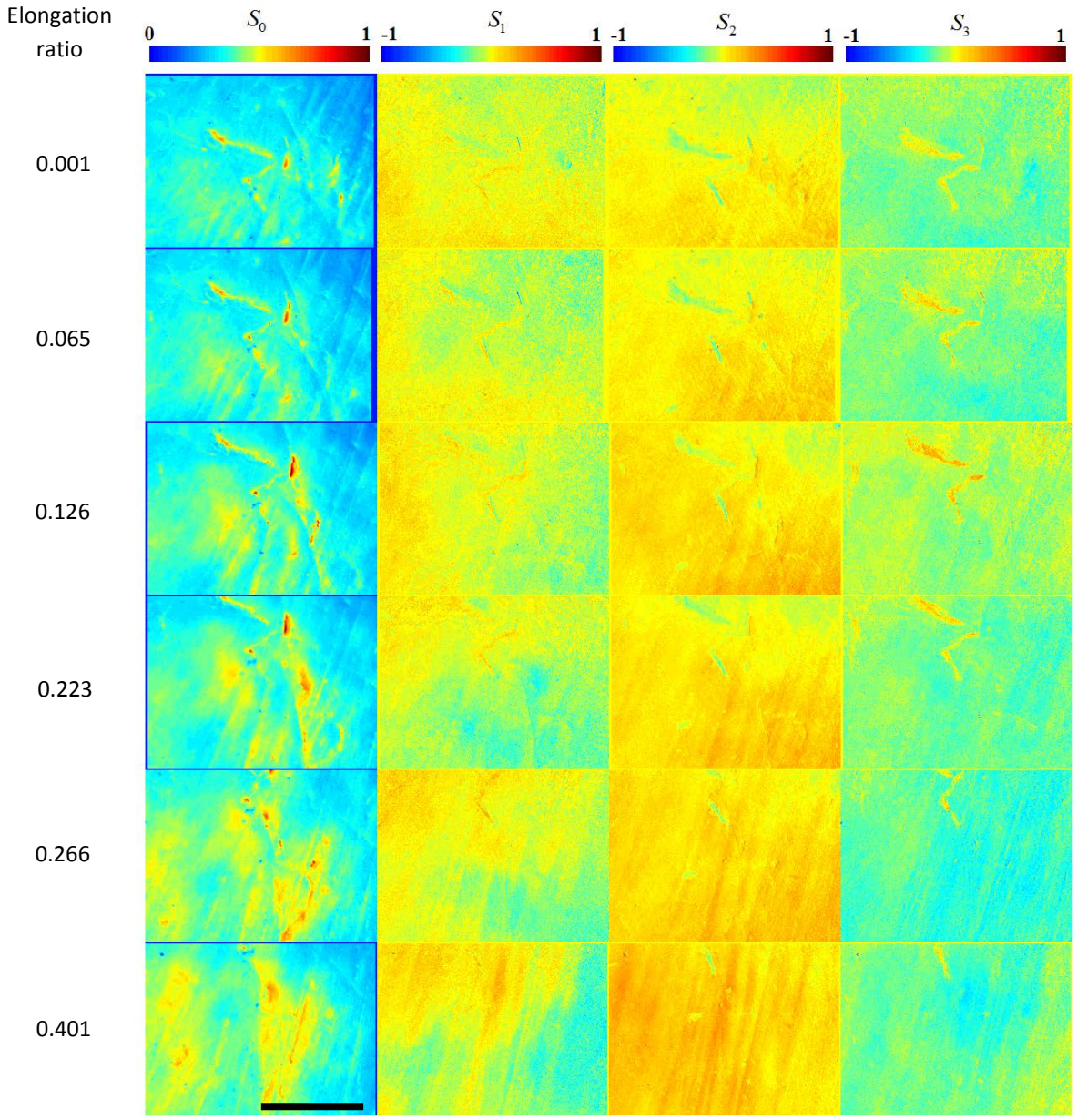

Figure 4.7. Stokes vector imaging for the $A_{\perp}$ sample for the highest energies probed in each step. The columns correspond to the 4 Stokes parameters and each row corresponds to different elongation conditions. The pump energy was 8.23 mJ for all rows. The scale bar corresponds to 1mm.

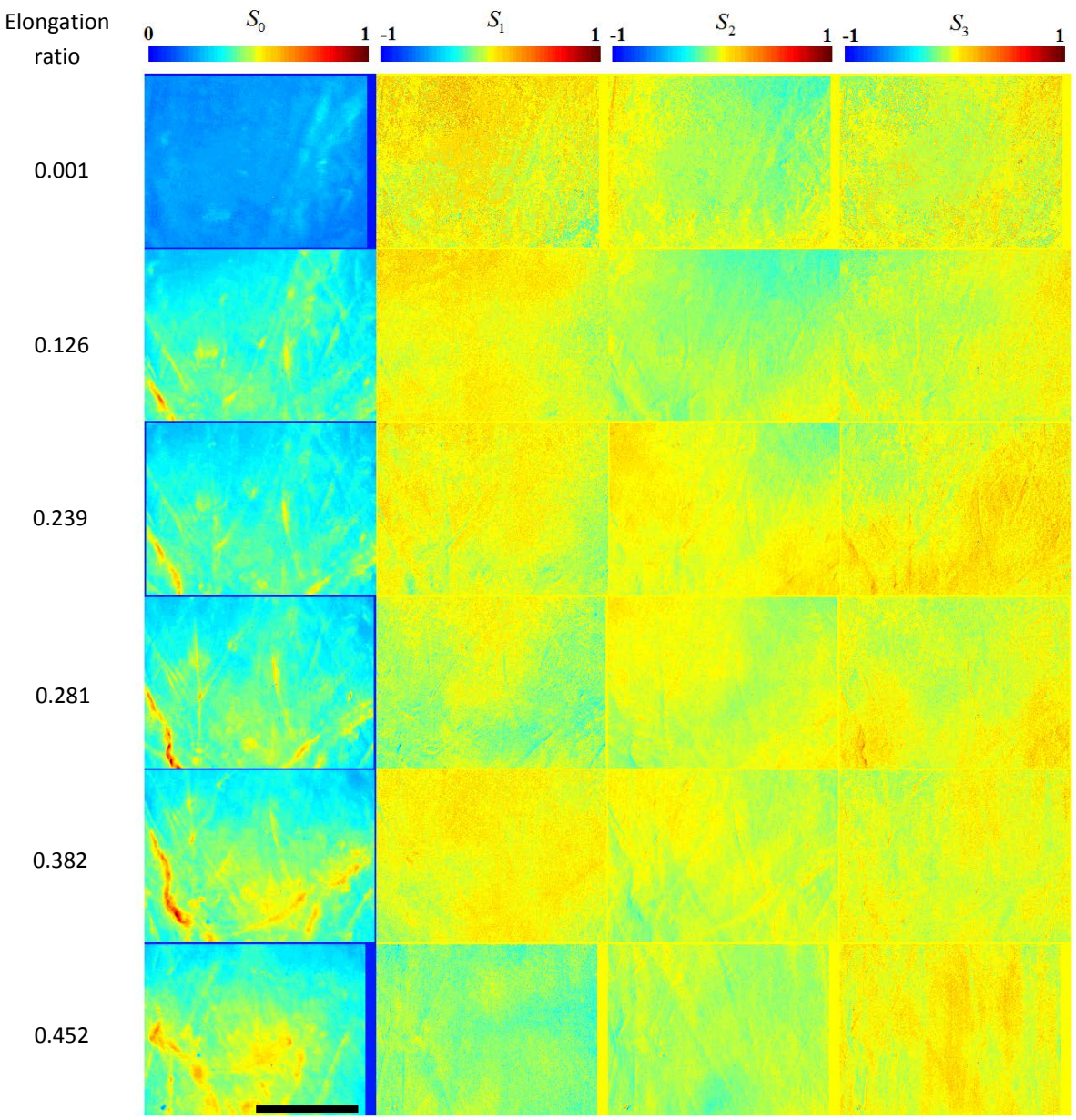

Figure 4.8. Stokes vector imaging for the $M_{\parallel}$ sample for the highest energies probed in each step. The columns correspond to the 4 Stokes parameters and each row corresponds to different elongation conditions. The pump energy was 8.23 mJ for all rows. The scale bar corresponds to 1mm.

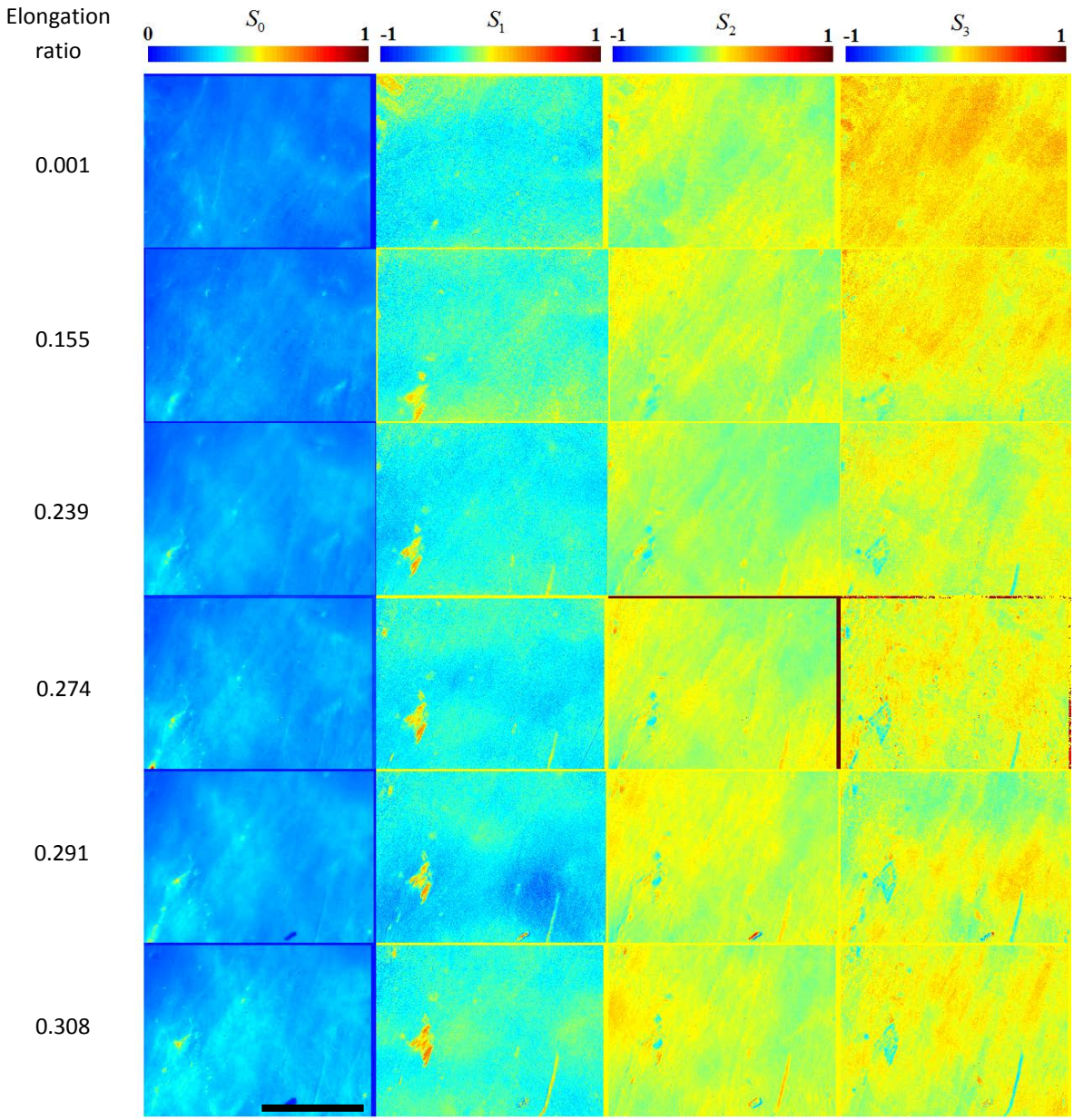

Figure 4.9. Stokes vector imaging for the M⊥ sample for the highest energies probed in each step. The columns correspond to the 4 Stokes parameters and each row corresponds to different elongation conditions. The pump energy was 10.87 mJ for all rows. The scale bar corresponds to 1 mm.

The images of the total intensity S_0 (figures 4.6 to 4.9) show a tendency to increase in the fiber-like features observed in the vertical direction as the elongation ratio increases. Particularly, for the sample shown in Figure 4.6, horizontal fiber-like features are observed

in the images of total intensity (S_0, first column) at zero elongation. As the mechanical test progresses, i.e., for higher elongation ratios, these features seem to change orientation, turning predominantly into vertically oriented features. The $A_{\perp}$ sample also shows a tendency towards the end of the mechanical test to present fiber-like features along the vertical direction (see Figure 4.7). These results suggest that the intensity of the random laser emission for individual fibers correlates with the amount of stress applied to the individual fibers. With the exception of $M_{\perp}$, the samples showed fiber-like features that increase the local intensity of random laser emission as the elongation ratio increases (see figures 4.6 to 4.8). This is a remarkable finding as it can be used as a microstress indicator which cannot be extracted from conventional mechanical tests. Even though the small change in the microstructure of the collagen fibers is not detectable by white light imaging or conventional mechanical tests, the random laser effect seems to be sensitive to such changes because an adequate variation of scatterer density can lead to drastic changes in the amount of random laser emission [3-5]. The only sample that did not exhibit this behavior was the $M_{\perp}$, probably because the content of straightened fibers is less than in the other samples as stated in previous subsections.

Figures 4.5 and 4.6 show a higher proportion of linear polarization (S_1, S_2) for the apical samples. As the test progresses, the fiber like features of S_1 images tend to have higher intensities as the elongation ratio increases, showing an increase of linearly polarized components oriented vertically inside the loading fibers. Figures 4.5 and 4.6 show that the dominant polarization component over the sampled area is linear oblique (45°) polarization for the case of the apical samples. The corresponding images for this polarization component (S_2) show a regular and spread color as the test progress. This effect is very similar to the evolution of the linear retardance shown in Chapter 2, in which a spreading of high values of retardance is observed as the elongation ratio increases. In particular, Figure 3.18 shows the appearance of fiber like features and its alignment as the tests progresses. Nevertheless, this behavior appears only in the apical samples. Medial samples do not exhibit a clear tendency in the S_2 component and in general, a higher content of S_3 components is clearly seen in the medial samples. Notice that the sample

yielding the least amount of total intensity was the $M_{\perp}$ sample, in agreement with the previous results placing this as the sample with the highest laser emission threshold.

Müller imaging analysis of the random laser emission from the samples seems to allow discriminating samples obtained from different regions of the pericardium sac. In contrast, this analysis does not seem to provide a clear distinction of the orientation at which the samples were cut. These results suggest that the pericardium can indeed be considered as a highly isotropic material, with fiber orientation, density and diameters that will vary with the position relative to the apex. The exact relation between the fiber features and the polarization properties of the random laser emission are still not clear. Nevertheless, the reported parameters such as emission threshold and peak wavelength can be used as a fingerprint of each sample, as these remain without substantial changes during the tensile test. The results further suggest that these changes are more related to the inner structure of the collagen fibers. Some features of the fiber ensemble can be inferred upon studying the dynamic evolution of a small area of the sample during the test. This can be done through analysis of consecutive images acquired during the test using digital image correlation (DIC) [61-63]. The results of such a technique will be helpful to compare the optical parameters obtained in this section with the mechanical features os the samples observed at different scales.

4.2. DIGITAL IMAGE CORRELATION RESULTS

The implementation of digital image correlation allows studying the behavior of a thin and soft material at the microscale. The details and general procedure of the technique have been referred previously in Chapter 2. In summary, the acquired images are sectioned in smaller subimages in order to perform the Willert and Gharib algorithm [61], obtaining the displacement vector fields on the region of interest over the sampled area. Figure 4.10 shows the white light images and the corresponding images for the Stoke's vector component S_0. The latter also shows the displacement vector field overlapped on the image for different values of the elongation ratio.

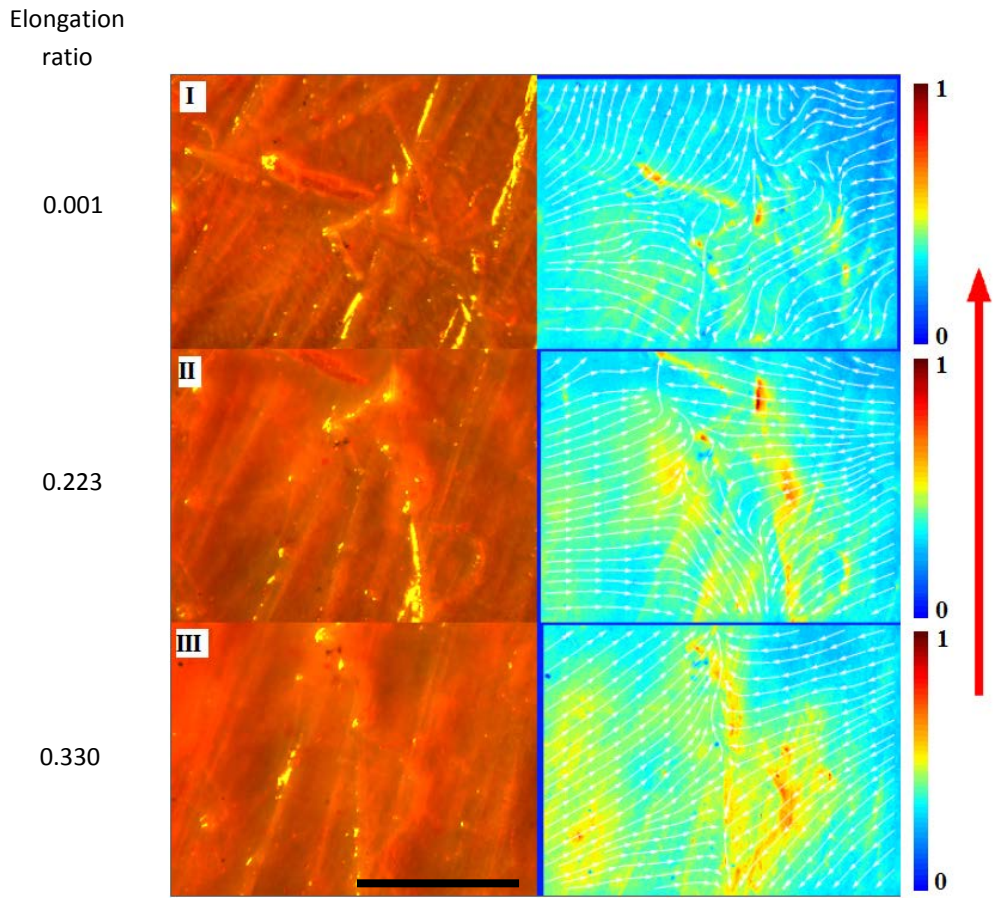

Figure 4.10. First column: white light images of the A⊥ sample; the brightness of the original images was modified in order to facilitate observation. Second column: S_0 images overlapped with their corresponding displacement vector fields. The color scale was normalized to the maximum intensity registered in the test. Each row is associated with different elongation ratios during the tensile test (see text). The red arrow on the right indicates the direction of the load during the uniaxial tension test.

The images shown in Figure 4.10 have been selected in order to fit the same criteria of Figure 2.17 (see Chapter 2). Therefore, the rows of Figure 4.8 labeled as I, II and III correspond to the regions of the stress-elongation ratio curve. These regions of the stress-elongation ratio curve have been reported in previous studies of bovine pericardium [26, 71]. Figure 4.11 shows the stress-elongation ratio curve for the $A\perp$ sample (same sample from Figure 4.10).

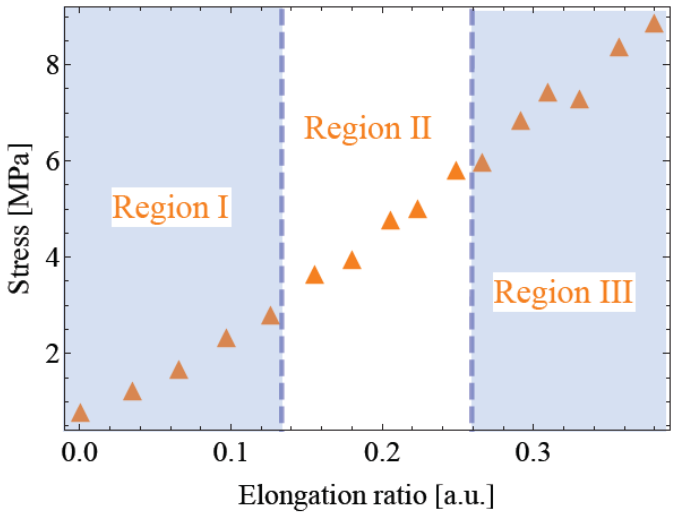

Figure 4.11. Stress-elongation ratio curve for A⊥ sample. The curve has been separated in 3 regions according to [26, 71]. Each region is related with a row of images in Figure 4.10.

The first row of Figure 4.10, which corresponds to the first step of the test, shows a displacement vector field that clearly deviates from the hyperbolic behavior seen in the rows II and III. This is expected because at this stage of the test the fibers start to align along the direction of the applied load. The displacement vector field of row II shows a more defined hyperbolic pattern with horizontal compression and vertical tension. The appearance of high intensity zones along the vertical direction seems to correlate with the more defined hyperbolic pattern on the displacement vector field. As confirmed by the white light images, the zones of highest random laser intensity correspond to the zones where superficial macro fibers of the tissue are clearly observed. Moreover, some of the fibers that exhibit high intensity of random laser emission in row II are present in the white light images of row I; however, for this stress level, the fibers do not exhibit high intensity in the random laser emission. This suggests a direct correlation between the intensity of the random laser emission and the applied stress on the individual fibers.

For the case of row III, the displacement vector field shows a well-defined hyperbolic pattern. This case corresponds to the last step of the test when, most of the fibers are already aligned. The axial tension in the middle of the image coincides with a high intensity zone in the S_0 image. As the white light image shows, the high intensity zone

in the middle of the image corresponds in turn to a fiber with the same orientation that the tension component of the displacement vector field. This confirms that the random laser emission is enhanced in those fibers whose orientation coincides with the tension component of the displacement vector fields. Hence, random laser emission is selectively improved within the fibers with more applied stress. Evidently, the fiber observed in the white light image is not the only fiber that will coincide with the direction of elongation. Furthermore, because the tissue sample is made out of an extremely large number of fibers, several of them will be pumped, but their individual emission will be impossible to resolve with the imaging set ups used in these experiments. The random laser emission from the inner fibers will experience multiple scattering events before being captured by the imaging arrangement. The fact that the fibers observed in the white light images are superficial fibers allows for the direct association with the high intensity zones on the random laser emission. In general, this kind of analysis may lead to local measurements of the stress experienced by individual collagen fibers within the tissue during tensile tests.

4.3. VISIBILITY MEASUREMENTS IN BOVINE PERICARDIUM BASED RANDOM LASERS

The spatial coherence of the random laser emission collected from the samples was studied by means of a custom-made two circular apertures slit. When partially coherent light passes through a slit of appropriate dimensions, an interference patterns appears on the imaged intensity [72]. Appendix E details the construction and characterization of the slit used in these experiments. The generation of interference fringes is a very convenient method for qualitatively probe the coherence of a light beam because optical coherence manifestly reveals when the fringes are formed [73]. In general, studying the fringes generated by an optical beam passing through an aperture or obstacle lies in the area of the optical coherence theory. In particular, the visibility V is a measure of the quality of the fringes generated by an interferometric system and is defined as:

$$V = \frac{I_{\max} - I_{\min}}{I_{\max} + I_{\min}} \qquad 4.7$$

In Equation 4.7, I_{max} indicates the maximum intensity, which corresponds to the bright fringes; I_{min} refers to the local minimum in the fringe pattern, which corresponds to the dark fringes. When the total intensity that passes through both apertures is the same (i.e., the distance from the source is much larger than the distance between the apertures), the visibility relates the complex degree of coherence γ_{12} as [73]:

$$V = |\gamma_{12}| \tag{4.8}$$

Equation 4.8 implies that one can explore the coherence of a light beam by studying the fringe pattern, because the visibility is identical to the modulus of the complex degree of coherence. In our experiments, the separation between the circular apertures is 200 μm while the slit is fixed 12 cm away from the samples. A notch filter was used to block the residual pump (see Chapter 3) and register only the random laser emission passing through the slit. The images used for this analysis were taken for a pump power well above threshold, and for different elongation steps during the mechanical tests. For each elongation step, four images were recorded for a fixed pump energy in order to average the recorded intensity. The visibility is then calculated with *Mathematica* upon finding the maximum intensity and its adjacent local minimum (see Figure 4.12).

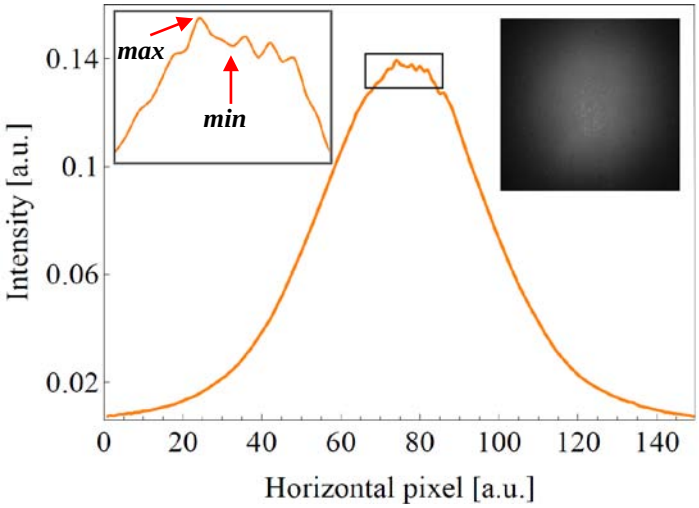

Figure 4.12. Typical intensity distribution recorded as function of the horizontal and vertical pixels of the image. The inset on the right shows the actual image as acquired by the CCD camera. The left inset shows a zoom view of the central part of the image. The arrows indicate the maximum and minimum positions used to calculate the visibility.

Figure 4.12 shows a typical image used to construct the intensity curve and calculate the visibility. For the data shown in Figure 4.12, the resulting visibility is 0.02, and in general, the values obtained in these experiments range between 0.005 and 0.026. These values indicate a low coherence for the light emitted by the samples. Notice that, as illustrated in Figure 4.12, a Gaussian-like curve was typically obtained rather than a well defined fringe pattern. Nevertheless, small local maxima and minima can be distinguished in the inset of Figure 4.12, even after the averaging process followed for these calculations. This indicates a rather small, but still present, degree of spatial coherence of the random laser emission from the bovine pericardium samples. Figure 4.13 shows the visibility as function of elongation ratio for the different pericardium samples.

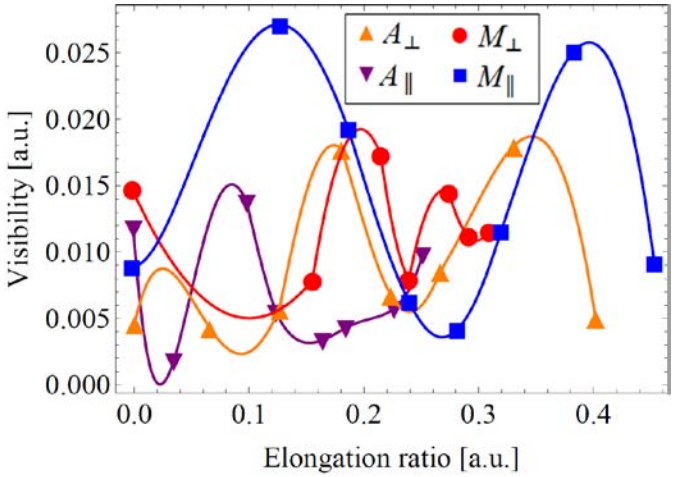

Figure 4.13. Visibility as function of elongation ratio for the different pericardium samples tested. $A^{\perp}$: Apical sample cut perpendicular to the apex axis; $A_{\parallel}$: Apical sample cut in the direction of apex axis. $M^{\perp}$: Medial sample cut perpendicular to the apex axis; $M_{\parallel}$: Medial sample cut in the direction of apex axis. Solid lines are merely a guide to the eye.

Figure 4.13 shows that for all the samples, the visibility oscillates between 0.005 and 0.025 as the elongation ratio increases. Apparently, the oscillations in visibility do not have the same period for all the samples; furthermore, each sample shows a different variation in the visibility during the mechanical test. A low value of visibility (and thus coherence) is not an expected result from any kind of laser. Nevertheless, it has been shown that the same random laser material can exhibit visibilities of 0.6 or 0.04 depending on the pumped volume [74]. This in turn is in agreement with the previous explanation in

which each collagen fiber can sustain several random laser modes. The presence of a large and uncorrelated number of lasing modes reduces the spatial coherence of the random laser emission. Although this low spatial coherence may be seen as a detrimental feature in a random laser, this characteristic can be useful in imaging applications [75]. In reference [75], the low spatial coherence of random lasers is used to obtain full-field speckle-free images.

CHAPTER 5

SCATTERING EXPERIMENTS VS RANDOM LASER EXPERIMENTS: A QUALITATIVE COMPARISON

Until this point, the scattering experiments and the results of random laser emission have been only considered as independent experiments. Each set of measurements have shown complementary information about the internal structure of the bovine pericardium samples. With this approach, the scattering media without optical gain was studied first exploring the way in which a tensile test changes the scattering properties of the material. Afterwards, chapters 3 and 4 focused on the spectral features of the random laser emission from similar samples but with the addition of a laser dye. In this chapter, a comparison between the two set of experiments is made, aiming at relating the scattering properties of the passive material (i.e. without gain) with the features of the emission in the random laser material (i.e. with gain).

5.1. MECHANICAL BEHAVIOR

In order to have a fair comparison of the two set of experiments, the experimental setups were maintained as similar as possible. The same imaging apparatus, pump laser and load frame are used for both cases, as well as the virtual instruments. Likewise, sample manipulation followed similar protocols, and even similar *Mathematica* notebooks for both cases were used for data analysis. Moreover, the samples for both set of experiments were cut from the same bovine pericardium sac. The similarity between the experimental setups allows switching from one setup to the other in a matter of minutes. This in turn allows carrying out both set of experiments in a time lapse of 48 hours. We first compare the mechanical behavior of the samples used in both set of experiments by plotting the stress-elongation curves (Figure 5.1).

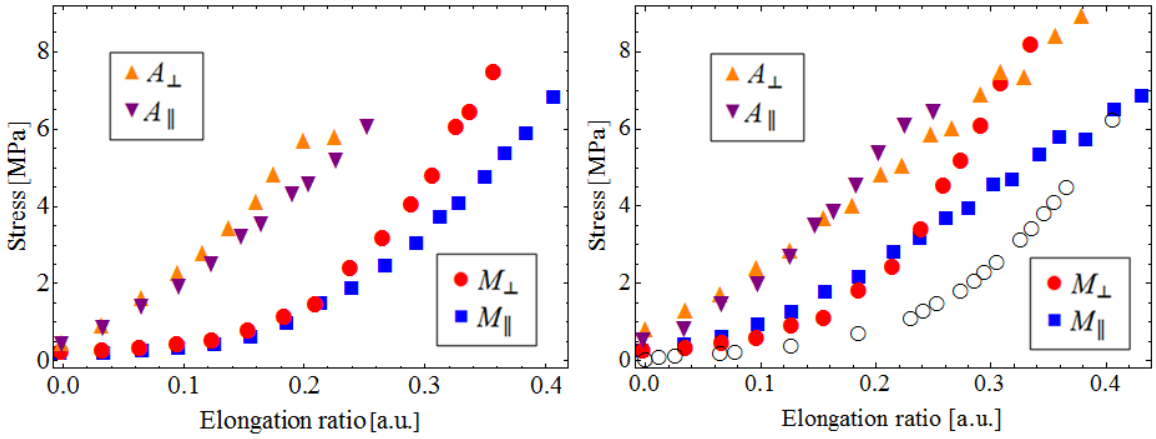

Figure 5.1. Comparison of the stress-elongation curves of the two set of experiments. Left plot: curves for bovine pericardium samples used in the scattering experiments of Chapter 2. Right plot: curves for bovine pericardium samples used in the random laser experiments of Chapter 3 and 4. The open circles in the right plot correspond to the data reported in reference [26].

Figure 5.1 shows that the samples used for these experiments exhibited different mechanical behaviors despite being cut from the same pericardium sac. Nevertheless, it is clear from Figure 5.1 that apical samples show a more linear tendency than medial samples. In particular, the $M\perp$ samples showed the most non-linear behavior for both sets of samples. When comparing the mechanical behavior of these samples with a different sac (open circles in the right plot of Figure 5.1), a clear difference is observed; it is evident that different specimens lead to distinct mechanical characteristics. The open circles in Figure 5.1 correspond to data presented in reference [26]; the main difference between the present experiments and those reported in [26] is the way in which the samples were manipulated. The variations in mechanical properties among samples cut in different tissue sections have been related to the content of collagen fibers [44]. More linear behavior is present in apical samples where more dense and compact fiber arrangements predominate [45]. Moreover, the crosslinking process enhances this behavior by linking several collagen fibers in more rigid beams [38]. On the other hand, medial samples show a less linear behavior despite being subjected to the same crosslinking process. This can be attributed to a less dense collagen fiber arrangement [50]. Less dense wavy fibers are less likely to form rigid fiber beams because even after the crosslinking, these kinds of fibers do not loss totally their

ability to uncrimp [50]. A distinction between samples cut perpendicular and parallel to the base-apex axis is not as clear as the difference between apical and medial samples. This suggests a random orientation in the fiber ensemble within the tissue.

5.2. MEAN FREE PATH AND NORMALIZED SHIFT

While the mean free path was obtained by means of an enhanced backscattering experiment (see Chapter 2, subsection 2.3.2), the normalized shift was defined in Equation 3.1 as the shift in emission peak wavelength normalized with respect to the spectral width (FWHM). The mean free path is the average length experienced by the light between two scattering events inside the scattering media [47, 48]. This parameter might be used as reference for random lasers because random lasing is intrinsically dependent on the scattering events inside the random material. Figure 5.2 depicts the mean free path obtained from the test of the $M_{\parallel}$ sample and the normalized shift obtained from the test of the $M_{\perp}$ sample. Both curves shown in Figure 5.2 are compared with their corresponding stress-elongation ratio curve.

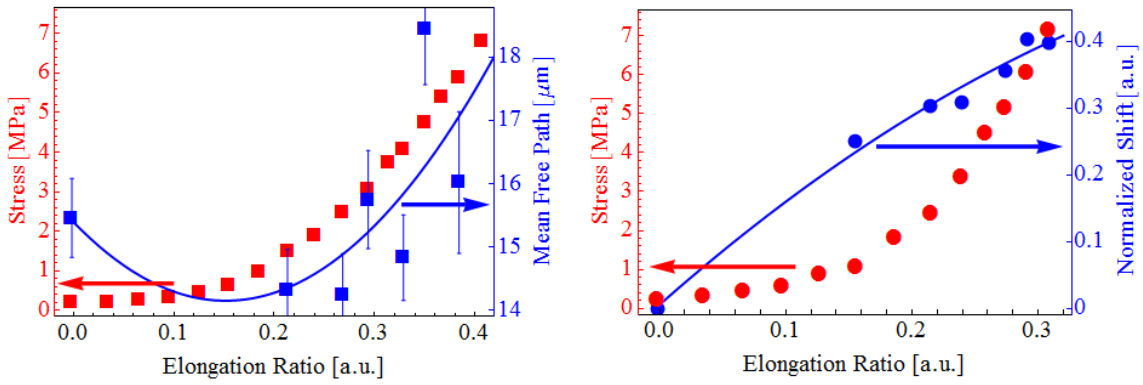

Figure 5.2. Left: Mean free path obtained by means of enhanced backscattering measurements in the corresponding test of the M∥ sample. Right: normalized shift calculated by comparing the peak wavelength with the width of the random laser emission of the corresponding test of the M⊥ sample. Both plots also show their corresponding stress-elongation ratio curve in red squares/circles.

In Figure 5.2 both, mean free path and normalized shift show a similar tendency to that obtained for the stress-elongation ratio curve: both parameters increase as the elongation ratio increases. The solid line in both cases corresponds to a polynomial fitting obtained by the least-square method. As seen in the figure, the mean free path shows a closer resemblance to its corresponding stress-elongation ratio curve than that observed for the normalized shift. Moreover, this same behavior of the mean free path was found in the two medial samples used for this set of experiments. On the other hand, the tendency of the normalized shift shown in Figure 5.2 was only observed in the apical perpendicular sample, while the others samples showed a nearly constant normalized shift during the tests. In the case of the other parameters of the random laser emission such as width and threshold, it was difficult to observe a clear tendency to correlate with the stress-elongation ratio curves.

At this point, conventional optical techniques such as enhanced backscattering seem to reveal more readily the changes in the microstructure of the samples than the random laser emission experiments. One of the difficulties in working with random lasers is the lack of a comprehensive theory capable to unveil all the rich phenomena involving random lasing. On the other hand, by its own nature, random laser emission is difficult to compare to a standard reference in order to have comparative measurements. In this work we compare the spectral features of random lasing with the parameters of scattering techniques in a qualitative approach knowing that the physics governing scattering and random laser emission are completely different.

5.3. MÜLLER MATRIX IMAGING, STOKES VECTOR IMAGING AND DIC ANALYSIS

A Müller matrix represents the transformation imposed by a material to the polarization state of an input beam [43]. Basically, an experimental Müller matrix is obtained by controlling the state of polarization of the input beam and analyzing the resulting polarization at the output of the sample. When a gain medium is added to the material, the concept of Müller matrix does not apply anymore because the relation

between the pump beam and the radiative emission is mediated by the processes of absorption and spontaneous/stimulated emission. Nevertheless, it is always possible to study the state of polarization of the light emitted from within a material with a random structure (i.e. tissue samples with gain). This in turns leads to the Stokes vector imaging when a CCD camera instead of a single detector is used to obtain the state of polarization of the light. Figure 5.3 shows a representative pair of images for both types of analysis.

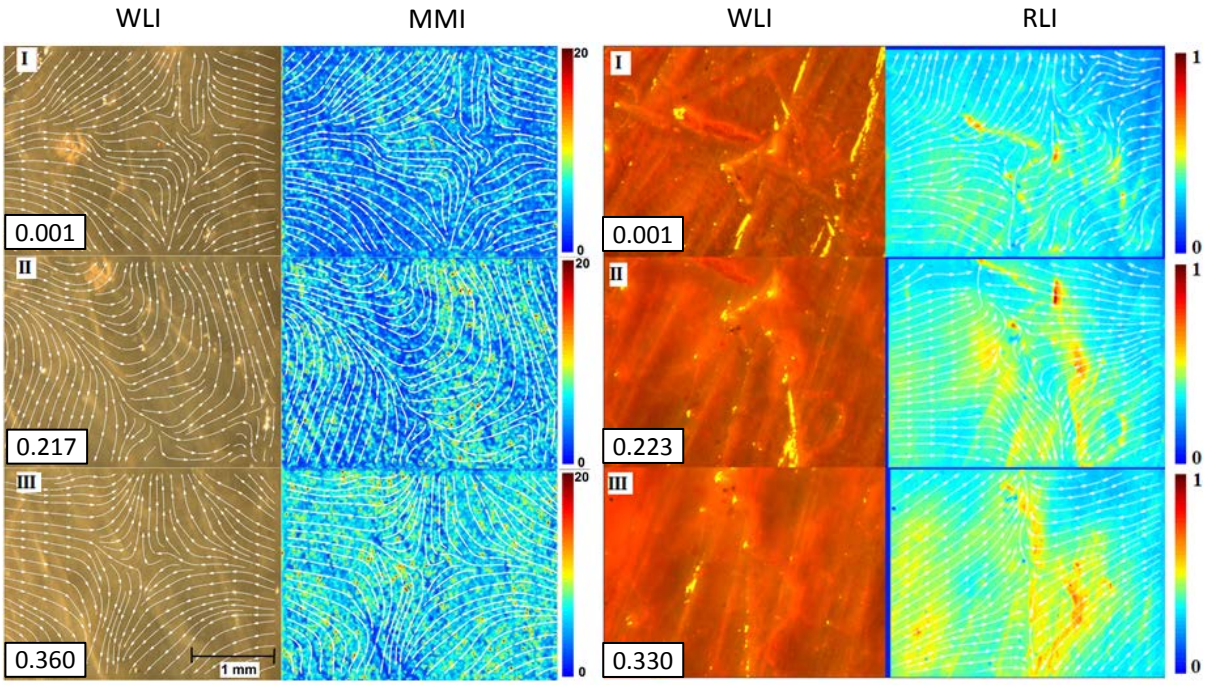

Figure 5.3. Comparison of the imaging techniques used in the scattering and random laser emission experiments. Left panel: retardance images obtained by means of Müller matrix imaging (MMI) with its corresponding white light images (WLI) and displacement vector fields for different elongation conditions. Right panel: Random laser intensity (RLI) images and its corresponding white light images and displacement vector fields for different elongation conditions. The charts at the bottom left corner of the white light images indicate the corresponding elongation ratio.

Figure 5.3 also shows the displacement vector fields obtained by digital image correlation (DIC). In this technique, two consecutive images are compared to determine the relative displacement between the two images [63]. As Figure 5.3 shows, when the elongation ratio was increased, both samples exhibited a hyperbolic pattern owing the

alignment of collagen fibers [62, 63]. The white light images of Figure 5.3 show that the inclusion of the dye increases the contrast in the image allowing observing more details in the superficial layer of the tissue. In order to emphasize this fact, the displacement vector fields were not depicted in the white light images of the samples corresponding to the random laser emission experiments. Because Müller matrix imaging is related to the whole thickness of the samples, the retardance images shown in Figure 5.3 indicate an increase in the overall birefringence in the imaged area. In contrast, the intensity of the random laser emission (S_0), shows zones of high intensity with fiber-like features that correlate with the superficial fibers shown in the white light images. This therefore shows that the information obtained from the tissue using both imaging techniques is complementary. Retardance images show the average behavior in the transversal direction of the fiber ensemble because the light analyzed has to travel across the whole thickness of the sample before reaching the CCD camera. On the other hand, data from the Stokes vector imaging suggest that the intensity of the random laser emission can provide information about the stress applied in a single fiber. As can be seen from Figure 5.3, the fiber-like features in the S_0 images increase in intensity from yellow-green tones to red-yellow tones. This might lead to a new approach for monitoring single collagen fibers during tensile tests upon proper image analysis.

5.4. FURTHER IMAGING ANALYSIS: INDIVIDUAL FIBER TRACKING

Additional analysis on the random laser intensity (S_0) included monitoring individual fibers during the tensile test. These were selected according to their orientation and intensity maps of the specific fibers were obtained by means of a binary mask performed with *Mathematica*. Thus far, the imaging methods have shown that the evolution of the random laser intensity depends on the orientation of the individual fibers. Moreover, images such as that shown in Figure 5.3 suggest that measurements of the stress exerted on individual fibers might be possible by means of monitoring the intensity of the random laser emission. In general, bovine pericardium contains collagen fibers with

different orientations. Some superficial fibers (those in the outermost layer) were observed in the white light images allowing for tracking their position during the mechanical test. By tracking the position of an individual fiber one can study its corresponding random laser emission during the mechanical test. This type of analysis is illustrated in Figure 5.4, showing the evolution of the random laser intensity (S_0) for individual fibers (labeled with ovals) during the test of the $A_{\parallel}$ sample.

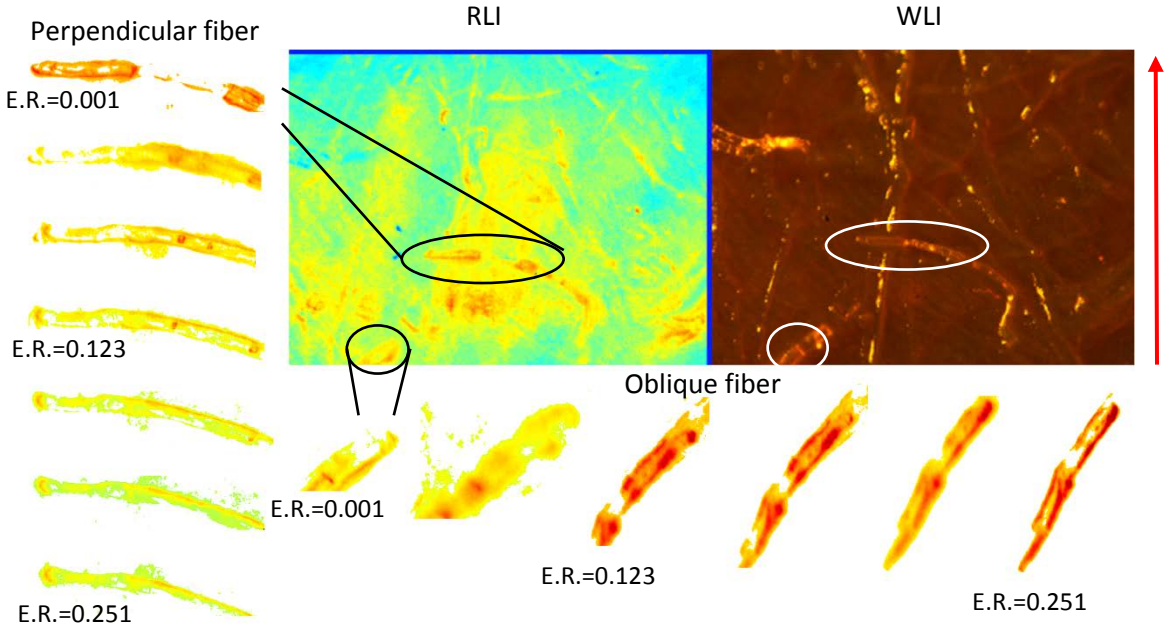

Figure 5.4. Random laser intensity (RLI) and white light image (WLI) of the $A_{\parallel}$ sample for zero elongation ratio. The ovals indicate individual fibers for which tracking of the random laser emission intensity was performed. Left and bottom panels: intensity maps of the random laser emission of the tracked fibers for different elongation ratios (some of the elongation ratios values have been marked as E.R. in both panels). The red arrow indicates the direction of the applied force.

Figure 5.4 shows two fibers that were selected for random laser intensity tracking during the mechanical test. One of the fibers has a horizontal orientation and is thus oriented perpendicularly to the applied stress. In contrast, the other selected fiber has an oblique orientation starting approximately at 45° at the beginning of the tests, and tends to align along the stress axis as the tests advances. The left and bottom panels in Figure 5.4 correspond to the intensity maps of the fibers at different elongation ratios and pumped

with the same energy per pulse (8.23 mJ). For the case of the perpendicular fiber, the random laser intensity decreases as the elongation ratio increases. In contrast, in the case of the oblique fiber shown in the bottom panel, the intensity maps show an increase as elongation ratio increases. This is a remarkable finding as the only difference between these fibers is their relative orientation to the stress axis. In order to quantify this observed effect, the mean intensity per pixel was obtained by integrating the intensity over the mapped area and divided by the total number of sampled pixels. The mean intensity per pixel for the two fibers tracked in Figure 5.4 is plotted in Figure 5.5 along with the corresponding stress-elongation ratio curve of the test.

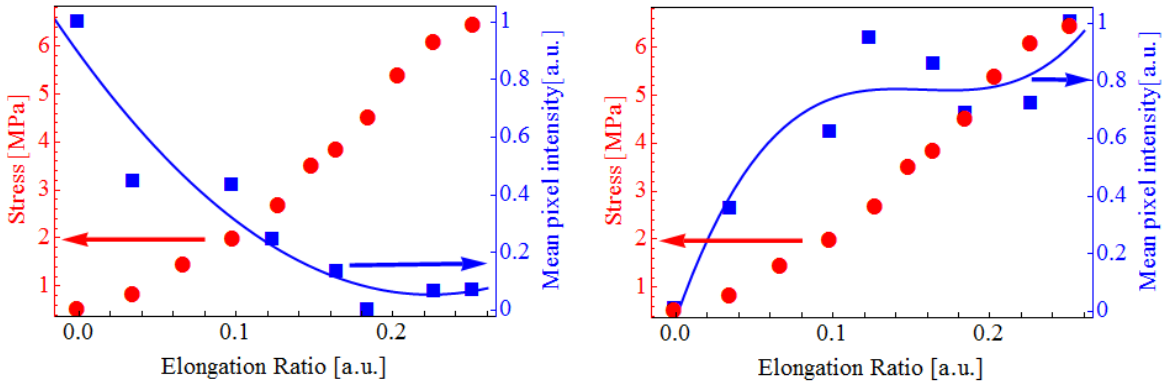

Figure 5.5. Mean intensity per pixel as function of elongation ratio for the two fibers tracked. Left panel: perpendicular fiber selected from the A∥ sample. Right panel: oblique fiber selected from the A∥ sample. The solid lines represent a polynomial fitting obtained with least-squares differences. The mean intensity per pixel in both cases was normalized and the red circles correspond to the stress-elongation ratio curve for this sample.

The mean intensity per pixel was used instead of the total intensity in order to effectively probe the intensity in maps with different areas. In particular, at the beginning of the mechanical test the oblique fiber is partially observed in the white light image but as the test advances, the vertical displacement of the sample during the test allows for observing more features of the fiber. Figure 5.5 shows that the mean intensity per pixel in the case of the perpendicular fiber decreases as the elongation ratio increases. On the other hand, for the case of the oblique fiber, the mean intensity per pixel increases as the elongation ratio was increased. In this particular case, a rapid increase at the beginning of

the test is observed; after a certain value of elongation ratio, the intensity remains unchanged showing a saturation-like behavior. In order to explore this effect further, another fiber from the test corresponding to the $M_{\parallel}$ sample was selected and analyzed with the same tracking procedure.

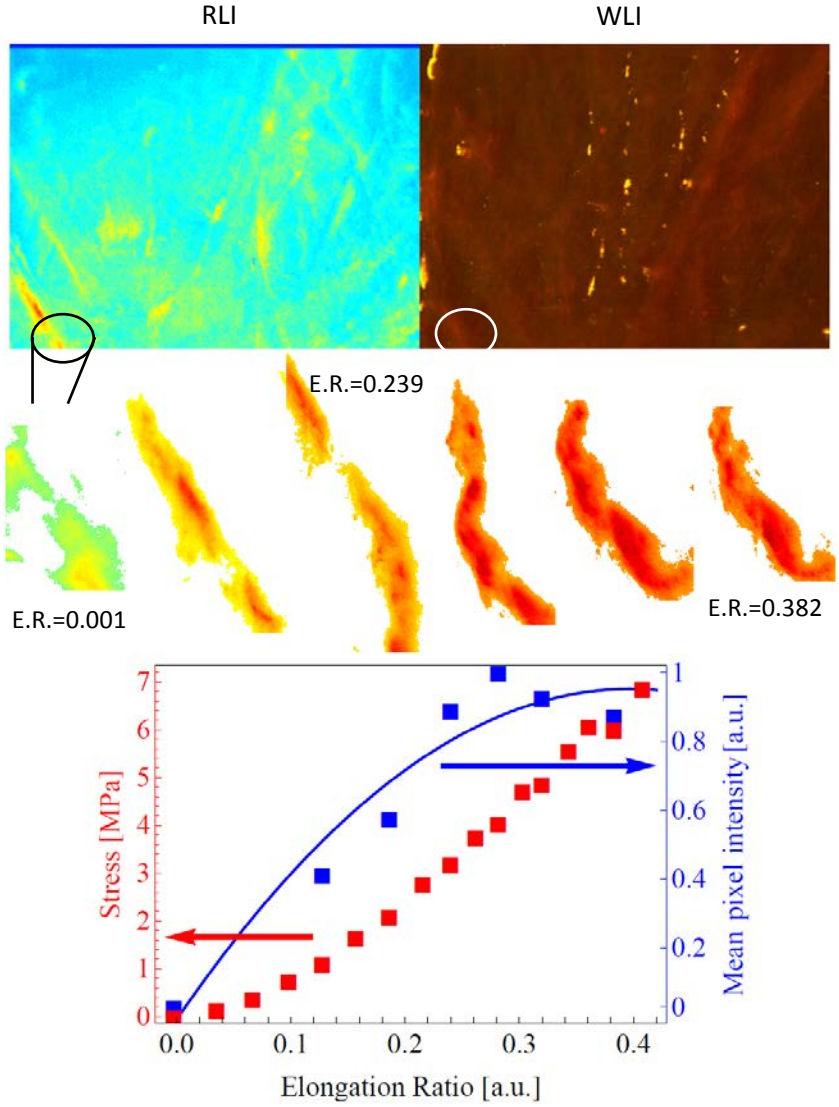

Figure 5.6. Upper panel: white light imaging (WLI) and random laser intensity (RLI) from the $M_{\parallel}$ sample at zero elongation ratio. The ovals indicate the tracked fiber. Central panel: intensity maps for different elongation ratios. Bottom panel: intensity per pixel as function of elongation ratio for the tracked fiber. The solid line represents a polynomial fitting (least-squares differences). The red squares correspond to the stress-elongation curve obtained for this sample.

Figure 5.6 shows an increase in the mean intensity per pixel as the elongation ratio increases. This is related to the vertical orientation of the tracked fiber shown in the upper panel of the figure. As in the case of the oblique fiber shown in Figure 5.5, the mean intensity increases rapidly at the begging of the test but the saturation-like behavior appears for higher elongation ratio values. The orientation of the fiber shown in Figure 5.6 is close to being parallel to the direction of the applied load; thus, the mean intensity increases noticeably as the elongation ratio increases. Evidently, more work on this type of analysis is required to fully elucidate the information provided by these observations. Nonetheless, these support the possibility of using the intensity of random laser emission from within collagen fibers as an indicator of the stress applied to individual fibers.

CHAPTER 6

CONCLUSIONS

In this work, we have demonstrated a versatile experimental setup to simultaneously perform optical and mechanical tests in soft and thin materials. The versatility of the setup allows switching from passive optical tests, such as Müller matrix imaging, to tests involving gain media such as random laser analysis. Switching from one type of test to the other can be done in a few minutes and control and data acquisition are conveniently obtained through comprehensive virtual instruments developed in *LabView*. Data analysis is subsequently carried out in *Mathematica* notebooks; hence, different types of data analysis can be performed as well.

Random laser emission from within bovine pericardium samples was also demonstrated. In all of the bovine pericardium samples used in this work, spectral narrowing (up to 10 times narrower than the fluorescence spectra) and threshold-like behavior were observed as a function of the pump energy. The spectral narrowing and the threshold behavior confirm that the light generated by the dye molecules experience enough scattering events to provide feedback to the laser medium. In this sense, this work represents the first effort to systematically probe the inner structure of bovine pericardium by means of random laser emission. In general the field of random lasers is an active research topic due to its potential applications and intriguing phenomena. Nevertheless, it is evident that more theoretical work is needed in order to gain a better understanding of all the rich effects involving random laser emission.

Aiming at having a reference for the random laser emission from the tissue samples, a set of experiments was performed exploring the passive characteristic of the bovine pericardium samples. Through scattering measurements, it was found that a clear

difference between medial and apical samples is observed, as obtained from measuring the mean free path from enhanced backscattering experiments. While in medial samples the mean free path increases with the elongation ratio, apical samples show a chaotic like behavior as a function of the elongation ratio. This observation may help to evaluate *in vivo* the condition of a leaflet by monitoring the mean free path, which gives information about the mean distance between collagen fibers. Even though the stress-elongation ratio curves show that apical samples are stiffer, the low stress values for small elongation ratios observed in medial samples may lead us to consider the formers as better suited for valve replacement; this is because minimizing the stress on these tissues can lead to a better hemodynamics facilitating the opening and closing of the valve [16, 76]. Moreover, the results shown in this work suggest that *in vivo* monitoring of the mean free path in bioprosthetic leaflets can lead to a detection of an increase of stiffness due to calcification.

Retardance images based on Müller matrix imaging have shown a good indicator of fiber alignment, as they correlate well with the displacement vector fields obtained by digital image correlation. Deeper investigation on these images may lead to a direct determination of the displacement vector fields via the retardance maps of the tissue. This in turns implies that a retardance image may predict the displacement of the tissue at small elongation ratio regimes based on the retardance gradients. Approaches such as the effective medium method [77] to study the refraction index of the tissue can complement these measurements in order to quantify the birefringence induce by complex and thin materials.

Using the Stokes vector imaging technique, we have found that the random laser emission is generated from within collagen fibers. Some of the implications of this statement are that for each collagen fiber pumped, a myriad of modes can be excited within the fiber, and the total emission from the tissue corresponds to the contributions of all the fibers. Each fiber can thus emit laser light in random modes, depending on its diameter and fibril density. As tensile tests induce low changes in fiber diameter [50], the spectral features of random laser emission registered no clear tendency during the mechanical test

performed in this work. In contrast, through tracking the laser emission from individual fibers, we found that the intensity of the random laser emission from these correlate well with the stress applied to the individual fibers. This result may represent a new approach on estimating the stress in individual collagen fibers by means of a correlation of the intensity of the random laser emission. It has been shown recently that the modes of intracellular lasers can be determined by means of hyperspectral imaging [78]. Hyperspectral imaging in our experiments could potentially give information about the specific modes excited by each fiber and thus provide a measure of the number of fibrils within a fiber. This approach to the understanding of collagen hierarchy would represent a novel method as the usual techniques to study nano and micro deformation in collagen tissues are based on x-ray spectroscopy [50]. In techniques such as wide angle x-ray diffraction (WAXD) and small angle x-ray scattering (SAXS), the helical collagen pitch or the fibril Ds tagger can be inferred from obtained spectra [79]. Nevertheless, these experiments require high degree of sophistication as they need a synchrotron source, an enclosed fluid chamber with transparent windows and low noise x-ray detectors. Compared to WAXD and SAXS, random laser emission imaging would allow probing the fibril hierarchy in a simple and inexpensive manner. We expect that this pioneer work in bovine pericardium random lasers will prove helpful in future biomedical applications based on optical tests.

REFERENCES

1. Saleh B., Teich M., *"Fundamentals of Photonics,"* Second Edition, John Wiley & Sons, USA, 2007, pp 540.
2. A. E. Siegman, *"Lasers,"* University Science Books, Cap. 13, 1986.
3. D. S. Wiersma, "Random lasers explained," *Nature Photonics*, vol. 3, pp. 246-247, 2009.
4. Q. Song, Z. Xu, S. Ho Choi, X. Sun, S. Xiao, O. Akkus, Y. L. Kim, "Detection of nanoscale structural changes in bone using random lasers," *Optics Letters*, vol. 35, no. 15, pp. 2624-2626, 2010.
5. Q. Song, S. Xiao, Z. Xu, V. M. Shalaev, Y. L. Kim, "Random Laser spectroscopy for nanoscale perturbation sensing," *Nature Photonics*, vol. 82, no. 11, pp. 2278-2281, 1999.
6. F. Lahoz, I. R. Martín, M. Urgellés, J. Marrero-Alonso, R. Marín, C. J. Saavedra, A. Boto, and M. Díaz, "Random laser in biological tissues impregnated with a fluorescent anticancer drug," *Laser Phys. Lett*. vol. 12, no. 4, 045805, 2015
7. H. Cao, Y. G. Zhao, "Random Laser Action in Semiconductor Powder," *Physical Review Letters*, vol. 82, no. 11, pp. 2278-2281, 1999.
8. C. R. Lee, S. H. Lin, C.H. Guo, S. H. Chang, T. S. Mo y S. C. Chu, "All-optically controllable random laser based on a dye-doped polymer-dispersed liquid crystal with nano-sized droplets," *Optics Express*, vol. 18, no. 3, pp. 2406-2412, 2010
9. Y. L. Chen, C. L. Chen, H. Y. Lin, C. W. Chen, Y. F. Chen, Y. Hung, C. Y. Mou, "Enhancement of random lasing based on the composite consisting of nanospheres embedded in nanorods template," *Optics Express*, vol. 17, no. 15, pp. 12706-12713, 2009.
10. X. Ma, P. Chen, D. Li, Y. Zhang, D. Yang, "Electrically pumped ZnO film ultraviolet random lasers on silicon substrate," *Applied Physics Letters*, vol. 91, no 25, pp. 1109-1111, 2007.
11. R. C. Polson, Z. V. Vardeny, "Random lasing in human tissues," *Appl. Phys. Lett*., vol. 85, no. 7, pp. 1289–1291, 2004
12. R. C. Polson, Z. V. Vardeny, "Cancerous tissue mapping from random lasing emission spectra," *Journal of Optics*, vol. 12, no. 2, pp. 4010-4014, 2010
13. N. Cuando-Espitia, J. Hernández-Cordero, C. García-Segundo, R. Quispe-Sicha, "Effects of the scatterer size and concentration on the spectral features of dye-based random lasers," Advanced Photonic Congress, Toronto, Canada, 2011.
14. Organ Procurement and Transplantation Network (OPTN) and Scientific Registry of Transplant Recipients (SRTR). OPTN/SRTR 2012 Annual Data Report. Rockville, MD: Department of Health and Human Services, Health

Resources and Services Administration; 2014.

15. K. Hammermeister, G. K. Sethi, W. G. Henderson, F. L. Grover, C. Oprian, and S. H. Rahimtoola, "Outcomes 15 years after valve replacement with a mechanical versus a bioprosthetic valve: Final report of the veterans affairs randomized trial," *J. Am. Coll. Cardiol*. vol. 36, no. 4, 1152–1158, 2000.

16. A. A. López-Zazueta, R. R. Ledesma-Alonso, J. V. Guzman, R. R: Zenit "Study of the Velocity and Strain Fields in the Flow Through Prosthetic Heart Valves." *J. Biomech. Eng*. vol. 133, no. 12, 2011.

17. X Li, Y Guo, K Ziegler, L. Model, S.D.D. Eghbalieh, R Brenes, S. Kim, Chang Shu, A. Dardik. "Current usage and future directions for the bovine pericardium patch". *Ann. Vasc. Surg*. vol. 25, no. 4, pp 561–568, 2011.

18. E. Akkermans, P.E. Wolf, and R. Maynard, "Coherent backscattering of light by disordered media: Analysis of the peak line shape," *Phys. Rev. Lett*., vol 56, 1471, 1986.

19. N. Cuando-Espitia, F.M. Sánchez-Arévalo, and J. Hernández-Cordero, "Enhanced backscattering measurements in bovine pericardium tensile tests," in *Latin America Optics and Photonics Conference*, OSA Technical Digest, paper LTh4A.22 (2014).

20. N. Ghosh, M. F. G. Wood, S. Li, R. D. Weisel, B. C. Wilson, R. Li, and I. A. Vitkin, "Mueller matrix decomposition for polarized light assessment of biological tissues," *J. Biophoton*., vol 2, no 3, pp 145-156, 2009.

21. J. Andreasen, A. A. Asatryan, L. C. Botten, M. A. Byrne, H. Cao, L. Ge, L. Labonté, P. Sebahh, A. D. Stone, H. E. Türeci and C. Vanneste, "Modes of random lasers," *Advances in Optics and Photonics*, vol. 3, no 1, pp. 88-127, 2011.

22. T. Mokhtari, C. M. Sorensen, A. Chakrabarti, "Multiple-scattering effects on static light-scattering optical structure factor measurements," *Applied Optics*, vol 14, no 36, pp. 7858-7861, 2005.

23. X. Jiang, C. M. Soukoulis, "Time dependent theory for random lasers," *Physical Review Letters*, vol. 85, no 1, pp. 70-73, 2000

24. F. Tenopala-Carmona, C. García-Segundo, Natanael Cuando-Espitia, Juan Hernández-Cordero, "Angular distribution of random laser emission," *Optics Letters*, vol 39, no. 3, pp. 655-659, 2014.

25. A. Smuk, E. Lazaro, L. P. Olson, N.M. Lawandy, "Random laser action in bovine semen," *Optics Communications*, vol. 284, pp.1257–1258, 2011.

26. J. C. Briones-Herrera, N. Cuando-Espitia, F. M. Sánchez-Arévalo, J. Hernández-Cordero, "Evaluation of mechanical behavior of soft tissue by means of random laser emission," *Rev. Sci. Instrum*., vol. 84, 104301,7 pp., 2013.

27. E. Filova, Z. Burdikova, L. Stankova, D. Hadraba; Z. Svindrych; D. Schornik, L. Bacakova, H. Chlup, E. Gultova, J. Vesely, L. Horny, R. Zitny, F. Straka; J. Pirk, "Collagen structures in pericardium and aortic heart valves and their

significance for tissue engineering," IEEE, E-Health and Bioengineering Conference (EHB), 6707382, 2013.

28. A. Viidik, *"Biology of Collagen",* Academic Press: London, 1980.

29. O. Ottani et al., "Collagen fibrillar networks as skeletal frameworks: a demonstration by cell-maceration/scanning electron microscope method," *Arch Histol Cytol*, vol 51, no. 3, pp. 249-261, 1988.

30. Y.C. Fung, "Elasticity of soft tissues in simple elongation," *Am J Physiol*, vol. 213, no. 6, pp. 1532-1544. 1967.

31. F.M. Sánchez Arévalo, M. Farfán, D. Covarrubias, R. Zenit and G. Pulos, "The micromechanical behavior of lyophilized glutaraldehyde-treated bovine pericardium under uniaxial tension," *J. Mech. Behav. Biomed. Mater*. vol 3, pp. 640–646, 2010.

32. L. Gross, M. Kugel, "Topographic anatomy and histology of the valves in the human heart," *American Journal of Pathology*, vol 7, pp. 445-456, 1931.

33. M.I Ionescu, et al., "Clinical durability of the pericardial xenograft: 11 years experience in Cardiac Bioprostheses," L.H. Cohn and V. Gallucci, Editors, Yorke Medical Books: New York. pp. 709-717, 1982.

34. C. Grapentin, S. Barnert, R. Schubert, "Monitoring the Stability of Perfluorocarbon Nanoemulsions by Cryo-TEM Image Analysis and Dynamic Light Scattering," PLoS ONE, vol 10 no 6, e0130674, 2015.

35. M. M. Basil-Jones, R. L. Edmonds, G. E. Norris, and R. G. Haverkamp, "Collagen Fibril Alignment and Deformation during Tensile Strain of Leather: A Small-Angle X-ray Scattering Study," *J. Agric.Food Chem*., 60, 1201 -1208, 2012.

36. L. D. Russell, *"Electron Microscopy. Principles and Techniques for Biologists*," jones and Bartlett Pub.: Boston, 1992.

37. E. A. Trowbridge, M. M. Black, C. L. Daniel "The mechanical response of glutaraldehyde-fixed bovine pericardium to uniaxial load," *Journal of Materials Science,* vol 20, pp 114-140, 1985.

38. H. Sung, Y. Chang, C. Chiu, C. Chen, H.Liang, "Crosslinking characteristics and mechanical properties of a bovine pericardium fixed with a naturally occurring crosslinking agent," *Journal of biomedical Materials Research*, vol 47, no 2, 1999.

39. L. G. Pikulik, K. I. Rudik, V. A. Chernyavskii, and A. F. Grib,"Induced anisotropy of solution of Rhodamine 6G in glycerin on excitation with a laser," *Journal of Applied Spectroscopy*, vol 63, no 2, 1996.

40. P. A. Anfinrud, D.E. Hart, J. F. Hedstrom and W. S. Struve, "Fluorescence depolarization of Rhodamine 6G in glycerol: a photon-counting test of three-dimensional excitation transport theory," *J. Phys. Chem*., vol 90, no 11, pp 2374-2379, 1986.

41. M. J. Pindera, C. T. Herakovich., "Shear characterization of uni directional

composites with the off-axis tension test," *Experimental Mechanics*, vol 26, no 1, pp 103-112, 1986.

42. V. Turzhitsky, J. D. Rogers, N. N. Mutyal, H. K. Roy, and V. Backman, "Characterization of light transport in scattering media at sub-diffusion length scales with Low-coherence Enhanced Backscattering," IEEE J Sel Top Quantum Electron. 16(3), pp. 619–626, (2010).

43. D. Golstein, *"Polarized Light",* Dekker, 2003.

44. J. Diamante t. al, "Collagen; ultrastructure and its relation to mechanical properties as a function of aging," *Proc R Soc Lond B*, vol 180, pp. 293-315, 1972.

45. J. Liao, I. Vesely, "Relationship between Collagen Fibrils, Glycosaminoglycans, and Stress Relaxation in Mitral Valve Chordae Tendineae," *Annals of Biomedical Engineering*, vol 32, no 7, 2004, pp 977-983

46. G. Kaminsky, L. Glazer, "Images of absolute retardance L·Δn, using the rotatingpolariser method," *Journal of Microscopy,* vol 198, no 1, 2000.

47. M. B. van der Mark, M. P. van Albada and A. Lagendijk, "Light scattering in strongly scattering media: Multiple scattering and weak localization," *Phys. Rev. Lett. B*., vol 37, no 7, 1988.

48. E. Akkermans, P.E. Wolf, and R. Maynard, "Coherent backscattering of light by disordered media: Analysis of the peak line shape," *Phys. Rev. Lett*. vol 56, pp 1471, 1986.

49. J. W. Dally, W. F. Riley, *"Experimental stress analysis,"* McGraw-Hill, 1965.

50. P. Fratzl, "*Collagen: Structure and Mechanics,"* Springer, 2008.

51. E. Akkermans, P.E. Wolf, R. Maynard and G. Maret, " Theoretical study of coherent backscattering of light by disordered media," *Journal de Physique. France*, vol 49, no 1, pp 77-98, 1988.

52. R. Bi, J. Dong, and K. Lee, "Coherent backscattering cone shape depends on the beam size," *Applied Optics*, vol 51, no 26, 2012.

53. S. Lu and R. Chipman, " Interpretation of Mueller matrices based on polar decomposition," *J. Opt. Soc. Am. A***,** vol 13, pp 1106-1113, 1996.

54. R. Azzam, " Propagation of partially polarized light through anisotropic media with or without depolarization: A differential 4 × 4 matrix calculus," *J. Opt. Soc. Am.* vol 68, pp 1756-1767, 1978.

55. R. Ossikovski, " Differential matrix formalism for depolarizing anisotropic media," *Opt. Lett*. vol 36, no 12,pp 2330-2332, 2011.

56. J. L. Pezzaniti and R. A. Chipman, " Angular dependence of polarizing beam-splitter cubes," *Applied Optics*, vol 33, no 10, 1994.

57. S. Kumar, H. Purwar, R. Ossikovski, I. A. Vitkin, and N. Ghosh, "Comparative study of differential matrix and extended polar decomposition formalisms for

polarimetric characterization of complex tissue-like turbid media," *J Biomed Opt.,* vol 10, 105006, 2012.

58. L. D. Barron, "*Molecular light scattering and optical activity,"* Cambridge University Press, 2004.

59. K. C. Hadley, and I. Alex Vitkin,"Optical rotation and linear and circular depolarization rates in diffusively scattered light from chiral, racemic, and achiral turbid media," *J. Biomed. Opt.,* vol 7, no 3, pp 291-299, 2002.

60. M. Ju, S. Tang, "Usage of polarization-sensitive optical coherence tomography for investigation of collagen cross-linking," *J. Biomed. Opt*., vol 20, no 4, 046001, 2015.

61. C. E. Willert, and M. Gharib, "Digital particle image velocimetry," *Exp. Fluids,* vol 10, no 4, pp. 181-193, 1991.

62. F.M. Sánchez-Arévalo, T. García-Fernández, G. Pulos, and M. Villagrán-Muniz, "Use of digital speckle pattern correlation for strain measurements in a CuAlBe shape memory alloy," *Mater. Charac.,* vol 60, no 8, pp 775-782, 2009.

63. F.M. Sánchez-Arévalo, and G. Pulos, "Use of digital image correlation to determine the mechanical behavior of materials," *Mater. Charac*., vol 59, no 11, pp 1572-1579, 2008.

64. M. Villagrán-Muniz, C. Garcia-Segundo, H. F. Ranea-Sandoval, C. Gogorza, G. M. Bilmes, "Photoacoustic analysis of stimulated emission in pulsed dye lasers," *Applied Physics B*., vol 61, no 4, pp 361-366, 1995.

65. D. Arifler, I. Pavlova, A. Gillenwater, and R. Richards-Kortum, " Light Scattering from Collagen Fiber Networks: Micro-Optical Properties of Normal and Neoplastic Stroma," *Biophysical Journal*, vol 92, pp 3260-3274, 2007.

66. L. R. G. Treloar, *"The physics of rubber elasticity,"* Oxford university press, 1975.

67. T. Zhai, J. Chen, L. Chen, J. Wang, L. Wang, D. Liu, S. Li, H. Liua and X. Zhang, "A plasmonic random laser tunable through stretching silver nanowires embedded in a flexible substrate," *Nanoscale*, vol 7, pp 2235-2240, 2015.

68. D.S. Wiersma and S. Cavalierit, "Light emission:A temperature-tunable random laser," *Nature*, vol 414, pp 708-709, 2001.

69. N. Cuando Espitia "Láseres aleatorios de tinte basados en partículas de SiO_2," Tesis de maestría, PCeIM-UNAM, 2011.

70. M. A. Noginov, *"Solid-state random lasers",* Springer, 2005.

71. N. Cuando-Espitia, F. Sánchez-Arévalo and J. Hernández-Cordero, "Mechanical assessment of bovine pericardium using Müeller matrix imaging, enhanced backscattering and digital image correlation analysis," *Biomedical Optics Express*, vol 6, no 8, 2015.

72. Mandel and E. Wolf, "Coherence properties of Optical Fields," *Revs. Modern Phys*, vol 37, 1965.

73. M. J. Beran, G. B. Parrent, *"Theory of partial coherence,"* Society of Photo-optical Instrumentation Engineers, 1974.

74. B. Redding, M. A. Choma, and H. Cao, "Spatial coherence of random laser emission," *Optics Letters*, vol 36, no 17, 2011.

75. B. Redding, M. A. Choma, and H. Cao, "Speckle-free laser imaging using random laser illumination," *Nature Photonics*, vol 10, pp 355-359, 2012.

76. O. Kraft, R Schwaiger, P. Wellner, "Fatigue in thin films: lifetime and damage formation," *Materials Science and Engineering A,* vol 319, pp 919-923, 2001.

77. R. G. Barrera and A. García-Valenzuela, "Coherent reflectance in a system of random Mie scatterers and its relation to the effective-medium approach," *Journal of the Optical Society of America A,* vol 20, no 2, pp. 296-311, 2003.

78. M. Humar, S. Hyun Yun, "Intracellular microlasers," *Nature photonics*, vol 9, pp. 572-576, 2015.

79. A. Fiorani, C. Gualandi, S. Panseri, M. Montesi, M. Marcacci, M.L. Focarete, A. Bigi, "Comparative performance of collagen nanofibers electrospun from different solvents and stabilized by different crosslinkers," *J Mater Sci Mater Med*, vol 25, no 10, 2014.

APPENDIX A

CALIBRATION OF THE LOAD CELL AND LVDT

The load cell calibration was done using pattern weights, which were previously corroborated by an analytical balance (Ohaus explorer pro, 0.1mg precision). The load cell signal output (N) vs. pattern loads (N) are presented in Figure A.1. For this force sensor the standard deviation was 68 mN. The LVDT calibration was done using the T-LA28A Zaber actuator as a positioner device. The LVDT signal output was compared with a Mitutoyo digital indicator used as a reference for displacement. The displacement calibration was done from -8 to 8 mm. As a result of this calibration the LVDT displacement signal output vs. digital indicator displacement was obtained as shown in Figure A.1. From these experimental points a linear regression was applied to get the equation of displacement and its standard deviation resulting in 58µm

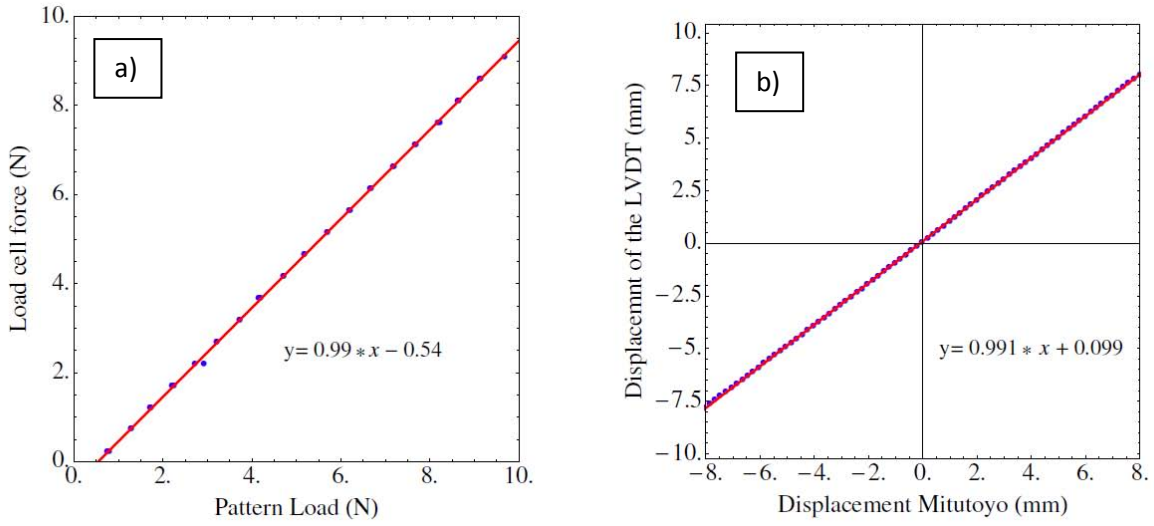

Figure A.1. Calibration curves for load cell (a) and LVDT (b). The force reference was done using pattern weights, and the position reference for the LVDT calibration was done by a Mitutoyo digital indicator.

A P P E N D I X B

PULSE ENERGY CHARACTERIZATION FOR THE PUMP LASER

A Laser Solo I by *New Wave* was used as the illumination source in the scattering experiments of chapter 2, and as a pump source in the random laser experiments of chapter 3. This is a Nd:YAG pulsed laser mainly designed for particle imaging velocimetry (PIV); nevertheless, it can be used as a illumination and pump source with the proper characterization of energy per pulse. In our case, energy per pulse for this laser was measured as function of laser console indicator with a *Molectron J2 5* system and a *Coherent* J 50MB YAG sensor head. Table B.1. shows the results of these measurements when console indicator is in *High*.

Console indicator (High)	Energy [mJ]
90	0.29
200	0.96
400	3.11
600	5.89
800	8.67
999	11.25

Table B.1. Energy per pulse as a function of laser console indicator. In all cases the indicator is in High. 30 pulses were averaged to obtain each measurement.

The standard deviation for the energy measurements was in the order of 5% for all the energies shown in Table B.1. It is important to note that we do not report any measurement of energy when console indicator is in *Low*; this is because the range limit of the *Molectron* system is 10 μJ and low energy pulses for this laser are below this value.

A P P E N D I X C

CALCULATION OF THE POLARIZATION PARAMETERS OF POLARIZERS AND WAVE PLATES

The general Müeller matrix for a polarizer that allows a proportional intensity p_x to pass in the x direction and p_y in the y direction is:

$$\begin{bmatrix} \frac{1}{2}\left(p_x^2 + p_y^2\right) & \frac{1}{2}\left(p_x^2 - p_y^2\right) & 0 & 0 \\ \frac{1}{2}\left(p_x^2 - p_y^2\right) & \frac{1}{2}\left(p_x^2 + p_y^2\right) & 0 & 0 \\ 0 & 0 & p_x p_y & 0 \\ 0 & 0 & 0 & p_x p_y \end{bmatrix}$$

Assuming a linear polarized beam with an angle α deviated from the y axis, the first component of the Stokes vector of the outcoming beam as the polarizer is rotated an angle θ is according to [43]:

$$\frac{1}{2}\left(p_x^2 + p_y^2\right) + \frac{1}{2}\left(p_x^2 - p_y^2\right) Cos(2(90+\alpha)) Cos(2\theta) + \frac{1}{2}\left(p_x^2 - p_y^2\right) Sin(2(90+\alpha)) Sin(2\theta) \qquad \text{C.1}$$

In order to obtain p_x and p_y, we let x and y be the laboratory horizontal and vertical reference axes, respectively. Then, we recorded the total intensity in the CCD for different angles of rotation of the polarizer with fixed energy in the illumination laser. As the intensity of a beam corresponds to the first component of the Stokes vector, we can find p_x, p_y and the angle α by fitting the intensity recorded in the CCD with the first component of the Stokes vector of equation C.1. Figure C.1a shows the experimental data and the fitting curve for the linear polarizer.

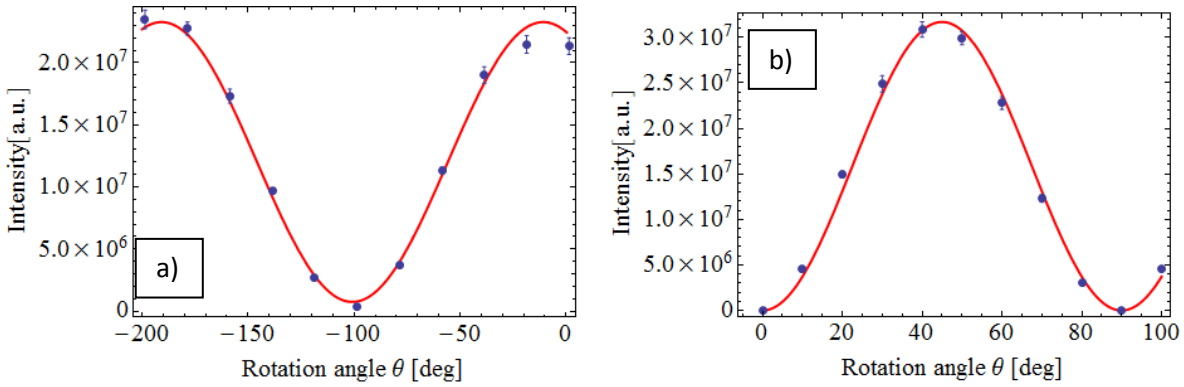

Figure C.1. Linear polarizer calibration curve (a), and quarter wave plate calibration curve (b). The blue points represent the experimental measurements, and the red solid line represents the fitting according to expressions C.1 and C.2.

The fitting values, found by means of mean square methods are p_x=0.1, p_y=0.72, α=21.7 deg. Similar values were found for the second linear polarizer used in the experimental setup (p_x=0.12, p_y=0.73, α=21.7 deg). In the case of an ideal wave plate, its Mueller matrix is given in terms of the shifting angle ϕ as:

$$\begin{bmatrix} 1 & 0 & 0 & 0 \\ 0 & 1 & 0 & 0 \\ 0 & 0 & Cos(\phi) & -Sin(\phi) \\ 0 & 0 & Sin(\phi) & Cos(\phi) \end{bmatrix}$$

When a wave plate is placed between two cross linear polarizers, the intensity as function of the angle of rotation θ is

$$\left[\frac{1}{4}+\frac{1}{4}\left(-Cos^2(2\theta)-Cos(\phi)Sin^2(2\theta)\right)\right]-\left[-\frac{1}{4}+\frac{1}{4}\left(Cos^2(2\theta)+Cos(\phi)Sin^2(2\theta)\right)\right] \qquad \text{C.2}$$

We used the linear polarizer described above to find shifting angles of $\phi_1/2$=48.5 deg and $\phi_2/2$=47.5 deg for the two quarter wave plates used in these experiments. The experimental data and the fitting curve are shown in Figure C.1b.

APPENDIX D

R6G-GLYCERIN PHOTODEGRADATION TEST

Photodegradation is the process in which photons alters a molecule by changing its shape, disassociating it to a smaller molecules or adding new atoms to the molecule. In dye molecules photodegradation is crucial because the molecule alteration typically leads to a non-fluorescent configuration. Photodegradation in dye lasers appears due to the interaction of the pump beam with the dye solution, which in general is subjected to recirculation in order to minimize photodegradation effects. We test the photodegradation of the optimum concentration of R6G-glycerin found in Chapter 3 by pumping a bovine pericardium sample immersed previously in the dye solution 24 hours before the test. The pump beam (Nd:YAG at 532 nm) was set to a fixed pulse energy of 10 mJ and the sample was illuminated with 35 consecutive pulses with a temporal separation of 2 minutes between pulses. Figure D.1 summarizes the results of this test.

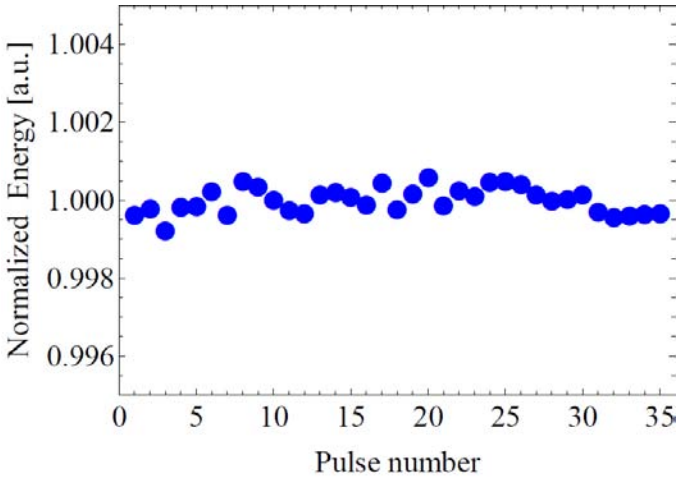

Figure D.1. Normalized energy as function of the number of pump pulses of a bovine pericardium sample with the solution of R6G-glycerin at 1g/l. The energy was normalized to the mean intensity of the 35 pulses.

As shown in table B.1, 10 mJ per pulse is in the upper energy limit provided by the pump laser used in this experiments. The light was collected and analyzed by means of a solid state spectrometer (Ocean Optics HR4000) and the counts were integrated over the spectrum to obtain the total energy recorded. Figure D.1 shows the normalized energy, calculated as the energy in each measurement divided by the mean energy of the 35 measurements. 35 pulses is the maximum number of pulses in each sample as we expect to probe 5 different energies in 7 elongation steps. As Figure D.1 shows, no significant decrease in energy appears in the sample after 35 pump pulses. In general, Figure D.1 shows a deviation of energy captured between pulses of the order of 0.01% which lies in the energy deviation of the pump pulse (5% maximum) reported in Appendix B.

APPENDIX E

CUSTOM MADE TWO APERTURE SLIT

In order to have an experimental apparatus to probe the degree of coherence of the random laser emission, we manufactured a two circular apertures slit by means of infrared laser light. A thin sheet of black plastic (polyethylene 0.3mm) was used as blocking material in which two circular holes were bored at the central region of the sheet. This method of fabrication was inspired in previous works in which opaque particles embedded in a polymeric matrix are heated by means of infrared laser light [1A]. The experimental setup used to fabricate the slit is shown in Figure E.1.

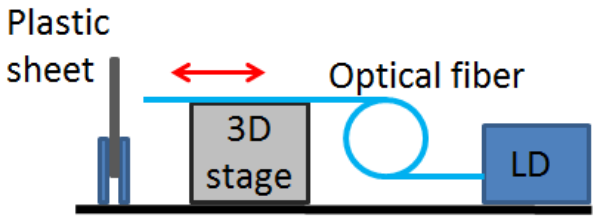

Figure E.1. Schematic representation of the experimental setup used to manufacture the two circular apertures slit. LD: CW laser diode (975 nm @50 mW), optical fiber (smf 28), plastic sheet (polyethylene 0.3 mm) and 3D stage.

Figure E.1 schematically shows a laser diode that launches laser light (975 nm, CW @ 50 mW) to the plastic sheet through an optical fiber mounted in a 3D stage. After turning the laser diode on, the 3D stage is slowly displaced towards the plastic sheet reducing the distance between the plastic sheet and the fiber tip. As this distance decreases, the light is absorbed in a smaller area, heating up the material. When the area is small enough the heat induced by the laser light is high enough to burn the material and the sheet start to incandesce generating a circular hole in the sheet. Then, the fiber is moved backwards and displaced aside. Finally, the fiber tip is moved towards the plastic sheet

again in order to fabricate a second hole. Figure E.2 shows an actual photograph of the custom made slit fabricated with this procedure.

Figure E.2. Left panel: photograph of the manufactured slit. The image shows two apertures of about 200μm separated a distance of 800 μm. Right panel: diffraction pattern generated by green laser light passing through the custom made slit. It is clear from the fringe patterns that the slit effectively diffracts the light passing through the slit.

As Figure E.2 shows, the slit has two circular apertures of about 200 μm in diameter and 800 μm apart. These dimensions are small enough to permit observable diffraction effects in the visible region. The right panel of Figure E.2 shows the diffraction pattern obtained by letting the pump beam pass through the slit in a similar configuration that the one schematically depicted in Figure 3.2. It is clear from the right panel of Figure E.2 that fringes of high intensity are evenly distributed in space with low intensity fringes in between. In particular, the ratio between these high and low intensities in the pattern is known as the visibility. For the case of the pattern shown in the right panel of Figure E.2, the visibility is 0.89, which shows the utility of this slit to probe the coherence of a beam in the visible region.

[1A] Reinher Pimentel-Domínguez, Francisco M. Sánchez-Arévalo, Mathieu Hautefeuille, Juan Hernández-Cordero, "Laser induced deformation in polydimethylsiloxane membranes with embedded carbon nanopowder," *Smart Materials and Structures*, Vol. 22, No. 3, 037001, 2013.

A P P E N D I X F

REQUESTED PATENT

SISTEMA OPTO-MECÁNICO Y METODOLOGÍA PARA EVALUAR EL COMPORTAMIENTO MACRO Y MICROMECÁNICO DE MATERIALES SUAVES Y TEJIDOS BIOLÓGICOS

DESCRIPCIÓN

CAMPO TÉCNICO DE LA INVENCIÓN

El objetivo de este sistema opto-mecánico es evaluar el comportamiento macro y micromecánico de tejidos biológicos suaves mediante dos técnicas ópticas no intrusivas: la correlación de imágenes digitales y el análisis espectral de la emisión láser aleatoria. Este sistema es capaz de registrar los cambios espectrales en la emisión láser aleatoria y correlacionarlos con el comportamiento macro y micromecánico del tejido biológico; estos últimos se obtienen a través de una prueba de tensión uniaxial acoplada a la correlación de imágenes digitales. Con la información obtenida es posible determinar el módulo de Young del material ensayado. El sistema está orientado hacia aplicaciones en el área de biomateriales; en particular para la caracterización mecánica de tejido biológico y polímeros suaves empleados como materiales sustitutos en bioimplantes; como son las válvulas cardiacas.

ANTECEDENTES

Los desórdenes causados en las válvulas cardiacas aórtica y mitral son cada vez más comunes hoy en día; estos se deben a nuestros recurrentes hábitos sedentarios y pésimos hábitos alimenticios; este no sólo es un problema nacional, es una tendencia mundial. En la mayoría de las patologías asociadas a válvulas cardiacas se requiere el reemplazo de alguna de las válvulas naturales por una válvula cardiaca mecánica o biológica: Alan S. Go, Dariush Mozaffarian, Veronique L. Roger, Emelia J. Benjamin, Jarett D. Berry et al. Heart disease and stroke statistics—2013 update: A report from the american heart association. Circulation, 127(1):e6–e245, 2013. Una de las ventajas de las válvulas biológicas es que los pacientes no tienen que tomar tratamientos anticoagulantes el resto de su vida: Lloyd-Jones, Robert J. Adams, Todd M. Brown, Mercedes Carnethon, Shifan Dai et al. Heart disease and stroke statistics—2010 update: A report from the american heart association. Circulation, 121(7):e46–e215, 2010; la principal desventaja se encuentra en su durabilidad que es no mayor a 10 años. Es por eso que en la actualidad se está trabajando en mejorar las propiedades mecánicas de los tejidos biológicos con los que se fabrican dichos bioimplantes. Así mismo se está trabajando en dispositivos y técnicas experimentales que

permiten caracterizar, cada vez de manera más detallada, el comportamiento mecánico de los materiales sustitutos. Existen reportes de dispositivos para estudiar tejidos suaves y delgados mediante pruebas de cedencia -esfuerzo constante- Medtronic Inc., "Droop tester apparatus and method", Carolyn Majkrzak, Roger Lee, KshitijaGarde, Eric Richardson, Benjamin Wong, USPTO 348135, 29 de Noviembre de 2012.; también se ha reportado un dispositivo electromecánico para determinar el comportamiento mecánico de tejido biológico a nivel macroscópico, en particular de pericardio de bovino: R. van Noort, S. Yates, T. Martin, A. Barker, and M. Black, "A study of theeffects of glutaraldehyde and formaldehyde on the mechanical behavior of bovine pericardium," Biomaterials**3**, 21–26 (1982). En ambos casos los estudios se enfocan en la parte macromecánica realizando pruebas estandarizadas.

Un aspecto importante en el diseño de las válvulas cardiacas del tipo biológico depende de la selección del tejido biológico con el cual se manufacturarán las valvas que conforman a la válvula cardiaca. Para seleccionar el tejido adecuado se requieren parámetros de diseño del material como el módulo de Young y la resistencia última a la tensión. La obtención de estos parámetros por medio de técnicas no invasivas resultan ampliamente útiles, ya que estas pruebas no alteran las propiedades mecánicas de las muestras ensayadas. Al conocer más parámetros del tejido estudiado, es posible desarrollar bioimplantes con mejor desempeño y predecir su funcionamiento con mayor precisión.

Se ha mostrado que es posible obtener parámetros como el módulo de Young a escala micrométrica a través de la correlación de imágenes: F. M. Sánchez-Arévalo, M. Farfán, D. Covarrubias, R. Zenit, y G. Pulos,"The micromechanical behavior of lyophilized glutaraldehyde-treated bovine pericardium under uniaxial tension," *J. Mech. Behav. Biomed.Mater*. **3**(8), 640–646, 2010. Además, esta técnica correlaciona bien con el módulo de Young a escala macroscópica. Recientemente se ha demostrado que la emisión de luz láser aleatoria generada en tejidos biológicos tiene propiedades espectrales que pueden correlacionarse con la estructura interna del tejido biológico: J. C. Briones-Herrera, N. Cuando-Espitia, F. M. Sánchez-Arévaloy J. Hernández-Cordero, "Evaluation of mechanical behavior of soft tissue by means of random laser emission*," Rev. of Sci.Instrum.,*84, 104301, 2013. El efecto de láser aleatorio se genera al combinar un medio activo que emita luz, con un medio que permita esparcir esta luz generada. La emisión que se obtiene en estas condiciones se conoce como luz láser aleatoria y sus características espectrales son altamente dependientes del material esparsor de luz. En especial, la longitud de onda de emisión y el ancho medio espectral (FWHM por sus siglas en inglés) son parámetros de la emisión láser aleatoria que dependen del arreglo de esparsores en el medio aleatorio, por ejemplo, tejido biológico: Consejo Superior de Investigaciones Científicas, European Laboratory for Non-linear Spectroscopy. "Método de control spectral de la emisión de un láser aleatorio," López Fernández Cefe, Blanco Montes Álvaro, Sapienza Riccardo, García Fernández Pedro, Wiersma Diederik,

Gottardo Stefano, H01S 3/30, 14 de Diciembre de 2009. En reportes anteriores se ha mostrado que es posible distinguir entre tejidos distintos al estudiar las características espectrales de la luz láser aleatoria que se produce dentro de los tejidos: Polson, R. C. Varden, Z. V. "Random lasing in human tissues," *Appl. Phys. Lett.*, vol. 85, no. 7, pp. 1289–1291, 2004. La presente invención correlaciona los cambios en las características espectrales de la emisión aleatoria en tejidos con los parámetros mecánicos durante pruebas de tensión uniaxial. Esto con la finalidad de obtener una técnica óptica no intrusiva para evaluar el módulo de corte y el módulo elástico de tejidos biológicos de manera simultánea, empleado correlación de imágenes digitales y análisis espectral de la emisión láser durante las pruebas.

DESCRIPCIÓN DETALLADA DE LA INVENCIÓN

El sistema para evaluar los tejidos consta de una parte mecánica y una parte óptica. La parte mecánica está formada por sensores de desplazamiento y fuerza (celda de carga) así como un actuador mecánico para elongar la muestra. Las muestras o probetas de tensión son sujetadas por medio de mordazas para evitar el deslizamiento de las mismas y permitir esfuerzos uniformes en la sección transversal de la probeta. El actuador, así como los demás elementos mecánicos se sujetan por medio de postes metálicos (acero inoxidable) como lo muestra la Figura 1. Por otro lado, la parte óptica está compuesta por un microscopio modular ensamblado específicamente para esta aplicación y consta de objetivos intercambiables (5Xy 10X), filtros ópticos montados en un tubo óptico que permite iluminación de campo claro y oscuro a través de un prisma. El microscopio se encuentra acoplado a una cámara CCD para registrar las imágenes de la superficie del tejido biológico; dicha superficie es iluminada por un láser de bombeo, y un espectrómetro capta los cambios de emisión del tejido durante la prueba de tensión. Los filtros bloquean el bombeo residual del láser de bombeo mientras que los objetivos permiten tomar imágenes de la muestra con aumentos de hasta 10X. El espectrómetro se utiliza para estudiar las características espectrales de la emisión láser de las muestras de tejido bombeadas con el láser de bombeo.

La metodología para preparar las muestras de tejido contempla el corte de probetas en forma estándar a través de un suaje (ASTM D1708) para pruebas de tensión uniaxial; posteriormente, se almacenan por al menos 24 horas en una solución de un tinte orgánico, por ejemplo Rodamina 6G, en glicerina con una concentración de entre 0.9 g/l y 1.1 g/l. La solución de tinte orgánico en glicerina actúa como medio activo del láser aleatorio. La acción láser se logra debido al medio activo embebido en el tejido y al esparcimiento óptico de las fibras de colágeno que constituyen el tejido. La realimentación positiva que es característica de los sistemas láser es fomentada por el esparcimiento múltiple ya que permite a la luz emitida permanecer más tiempo dentro del medio activo. Debido a que las características espectrales de la emisión láser aleatoria son altamente dependientes de la configuración del medio esparsor, los cambios de estas características ofrecen información acerca de la estructura interna del material estudiado. En este caso, los cambios en

ancho medio espectral de la emisión láser aleatoria durante la prueba están relacionados a la alineación de las fibras de colágeno del tejido biológico.

La metodología para realizar las pruebas consiste en elongar la probeta de tejido mientras su superficie es iluminada con el láser de bombeo. Durante la prueba el sistema opto-mecánico es capaz de registrar los datos de fuerza, desplazamiento, espectro de emisión e imágenes de la superficie de la muestra simultáneamente; lo anterior se logra a través de una tarjeta de adquisición de datos y una tarjeta de adquisición de imágenes conectadas a una PC y sincronizadas mediante un código computacional. Con los datos obtenidos durante la prueba se construyen las curvas de esfuerzo contra razón de elongación y ancho medio espectral contra razón de elongación. La curva de esfuerzo contra razón de elongación caracteriza a escala macrométrica el comportamiento mecánico del tejido. La curva de ancho medio espectral contra razón de elongación correlaciona con la curva de esfuerzo contra deformación debido a que el ancho medio espectral de un láser aleatorio está vinculado a la densidad y disposición espacial del arreglo de esparsores: J. C. Briones-Herrera, N. Cuando-Espitia, F. M. Sánchez-Arévaloy J. Hernández-Cordero, "Evaluation of mechanical behavior of soft tissue by means of random laser emission*," Rev. of Sci.Instrum.,*84, 104301, 2013.Por otro lado, las imágenes obtenidas son analizadas por medio de la correlación de imágenes digitales para obtener el campo de desplazamiento. Este procesamiento de imágenes permite obtener el módulo de Young del material a nivel micromecánico como ya fue reportado en: F. M. Sánchez-Arévalo, M. Farfán, D. Covarrubias, R. Zenit, y G. Pulos,"The micromechanical behavior of lyophilized glutaraldehyde-treated bovine pericardium under uniaxial tension," *J. Mech. Behav. Biomed.Mater*. **3**(8), 640–646, 2010 y por J. C. Briones-Herrera, N. Cuando-Espitia, F. M. Sánchez-Arévaloy J. Hernández-Cordero, "Evaluation of mechanical behavior of soft tissue by means of random laser emission*," Rev. of Sci.Instrum.,*84, 104301, 2013..Al correlacionar los datos mecánicos a macro y microescala con las características espectrales de la emisión láser aleatoria, se puede obtener información acerca de la estructura interna del tejido estudiado.

EJEMPLOS

Los siguientes ejemplos son para ilustrar la invención pero en ningún momento es para limitarla.

Una probeta de tensión uniaxial de pericardio de bovino que ha sido cortada en "forma de hueso" y tratada químicamente con glutaraldehído para mejorar sus propiedades mecánicas; la probeta es además almacenada durante 24 horas en una solución de Rodamina 6G en glicerina con una concentración de 1.0 g/l. Esta muestra se puede observar en la Figura 2. La muestra de tejido se coloca en el dispositivo de prueba y se elonga mientras se ilumina con un láser Nd:YAG operando nominalmente a 532 nm con una energía aproximada de 17mJ por pulso. El sistema opto-mecánico registra la fuerza, el desplazamiento, el espectro de emisión además de imágenes de una de las caras de la muestra durante la prueba. Con los datos de fuerza y desplazamiento de la

prueba junto con la geometría de la muestra se obtiene la curva de esfuerzo contra razón de elongación. El esfuerzo σ se define como la fuerza por unidad de área (de la sección transversal de la probeta) aplicada a la muestra de la siguiente forma:

$$\sigma = \frac{F}{A}$$

Por otro lado, la razón de elongación se define como:

$$Razón\ de\ elongación = \lambda - \lambda^{-2}$$

Donde λ puede definirse en términos de la deformación ingenieril ε como:

$$\lambda = \epsilon + 1$$

La curva de esfuerzo contra razón de elongación puede observarse en la Figura 3. En general, la curva de esfuerzo contra razón de elongación de la muestra estudiada es no lineal. Sin embargo, se observa que el comportamiento es más lineal para razones de elongación mayores, en este caso 0.8. En la Figura 3 se observan además imágenes tomadas a diferentes instantes de la prueba. Al analizar las imágenes mediante la técnica de correlación de imágenes digitales se obtienen campos de desplazamiento como los que se muestran en las Figura 4 y 5. Los campos vectoriales de desplazamiento mostrados en las figuras 4 y 5 corresponden a imágenes capturadas en los puntos A-B y C-D de la Figura 3 respectivamente. Mientras que el campo de vectores que corresponde entre las imágenes de los puntos A-B presenta un patrón sugiriendo deformación cortante, el campo de vectores entre imágenes correspondientes entre puntos C-D muestra un patrón hiperbólico, que es característico de un material compuesto por fibras alineadas.

Por último, los datos obtenidos a través del espectrómetro, en este caso un espectrómetro de estado sólido marca Ocean Optics modelo HR4000 son estudiados de acuerdo a la razón de elongación en que fue tomado cada espectro de emisión. La Figura 6 muestra distintos espectros de emisión para varias razones de elongación durante la prueba. Como lo muestra la Figura 6, los espectros para varias razones de elongación tienen distintas características. En la Figura 7 se grafican tanto el esfuerzo como el cambio en ancho medio espectral (ΔFWHM) en función de la razón de elongación durante la prueba. Como se observa en la Figura 7, la curva obtenida mediante la medición mecánica y la curva óptica se correlacionan bien en la parte lineal de las curvas. En esta región es posible establecer que la pendiente de la curva de esfuerzo contra la razón de elongación corresponde al módulo de corte (*G*) del tejido biológico; se ha reportado que para el pericardio de bovino la razón de Poisson es igual a 0.5 puesto que su comportamiento mecánico corresponde al de un elastómero [5]. Por otro lado sabemos que el aumento en el ancho medio espectral de la emisión indica que el láser aleatorio deja de emitir luz láser conforme la muestra es elongada. En conjunto, la información recopilada por el sistema indica que mientras la muestra es elongada, las fibras de las que está compuesto el tejido se alinean al eje en el cual se aplica la fuerza, como lo indica el patrón parabólico de la Figura 5. Además, la concentración de

fibras por unidad de volumen decrece con la elongación del tejido como lo muestra el aumento de ancho medio espectral de la Figura 7.

BREVE DESCRIPCIÓN DE LAS FIGURAS

Figura 1.Representación esquemática que muestra el sistema opto-mecánico para evaluar el comportamiento mecánico a micro y macro escala. El actuador, el sensor de desplazamiento (LVDT), la celda de carga y la muestra están acoplados mecánicamente en el mismo eje usando postes metálicos y elementos mecánicos. La parte óptica del sistema la constituyen el conjunto de filtros y objetivos de microscopio; así como la cámara CCD que registra las imágenes de la muestra durante la prueba de tensión. Se muestra también esquemáticamente el láser de bombeo y el espectrómetro para analizar la emisión de la muestra. Todos los elementos de lsistema presentado aquí están controlados mediante una PC con un código computacional.

Figura 2. Fotografía de una muestra de pericardio de bovino que fue almacenada por 24 horas en una solución de Rodamina 6G en glicerina con una concentración de 1.0g/l). La muestra de pericardio fue cortada siguiendo la metodología reportada anteriormente en “forma de hueso” para obtener una geometría estándar para las pruebas de tensión uniaxial.

Figura 3. Curva de esfuerzo contra razón de elongación para una muestra de pericardio de bovino tratado con glutaraldehído para lograr entrecruzamiento de fibras. La imágenes marcadas como i, ii, iii y iv corresponden a las imágenes tomadas en los puntos A,B,C y D de la prueba.

Figura 4. Campos de desplazamiento entre imágenes para los puntos A y B marcados en la figura 3. Este campo muestra el proceso de alineamiento de las fibras en la dirección de aplicación de la carga.

Figura 5. Campos de desplazamiento entre imágenes para los puntos C y D marcados en la figura 3. Este campo muestra un claro patrón hiperbólico que es característico de materiales hechos de fibras alineadas.

Figura 6. Espectros de emisión para distintas razones de elongación. Las características espectrales de la emisión cambian conforme la razón de elongación aumenta.

Figura 7. Curvas de esfuerzo contra razón de elongación y cambio en el ancho medio espectral contra razón de elongación. Ambas curvas tienen una pendiente similar para razones de elongación mayores a 0.2.

REIVINDICACIONES

Habiendo descrito suficiente nuestra invención, consideramos como una novedad y por lo tanto reclamamos como de nuestra exclusiva propiedad, lo contenido en las siguientes reivindicaciones:

1. El sistema opto-mecánico que consta de sensores de fuerza y desplazamiento; microscopio óptico; cámara CCD y espectrómetro. Caracterizado por obtener datos de

fuerza, desplazamiento y espectro de la emisión láser aleatoria en una prueba de tensión uniaxial.

2. El sistema según la reivindicación 1, en el que muestras de tejido suave son cortadas con geometrías estándar para pruebas de tensión uniaxial.
3. La metodología que se sigue para preparar las muestras utilizadas en el sistema de la reivindicación 1, que se basa en el uso de muestras de tejido suave, tratadas con una solución de tinte orgánico como Rodamina 6G en glicerina para obtener emisión láser aleatoria en tejido biológico suave.
4. De acuerdo con las reivindicaciones 1,2 y 3, la metodología para la prueba opto-mecánica se basa en realizar una prueba de tensión uniaxial al mismo tiempo que se ilumina la muestra con un láser de bombeo y se registra el espectro de emisión de la luz láser aleatoria.
5. Según las reivindicaciones 1, 2,3 y 4, la correlación entre las curvas de esfuerzo contra razón de elongación y ancho medio espectral contra razón de elongación se utilizan para determinar cambios en la microestructura de la muestra estudiada através de la determinación de módulo de corte.

RESUMEN

El sistema opto-mecánico para evaluar el comportamiento mecánico de materiales suaves y delgados y tejido biológico. El sistema incorpora dispositivos mecánicos y ópticos para obtener el comportamiento macro y micromecánico de muestras de materiales suaves con geometrías estándar para pruebas de tensión uniaxial. La parte mecánica del sistema consta de sensores de fuerza y desplazamiento además de un actuador para realizar pruebas de tensión uniaxial estándar. La parte óptica del sistema consta de un microscopio, una cámara CCD para registrar los cambios a nivel micro de la superficie de la muestra y una fibra óptica acoplada a un espectrómetro que registra la información de la emisión láser aleatoria. Esta última es obtenida al bombear la muestra con un láser de bombeo que provee la energía externa para el láser aleatorio. Al usar las técnicas de correlación de imágenes digitales y el análisis espectral de la emisión láser aleatoria se obtiene información sobre la respuesta de las muestras bajo distintos niveles de esfuerzo aplicado. La correlación entre las curvas mecánicas y óptica brindan información acerca de los cambios en la microestructura de la muestra durante la prueba.

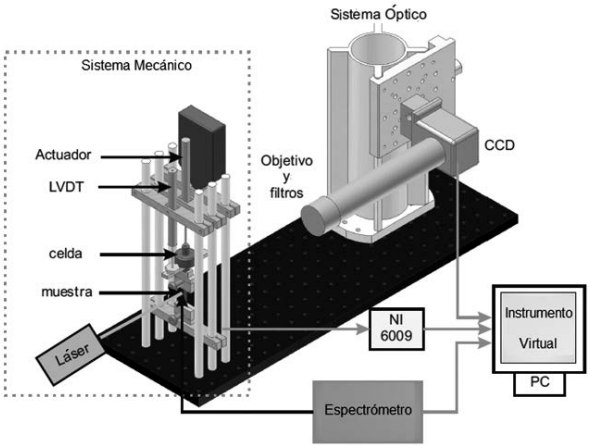

Figura 1

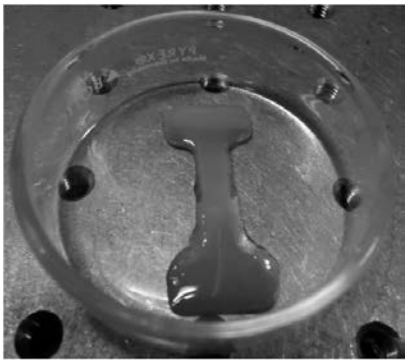

Figura 2

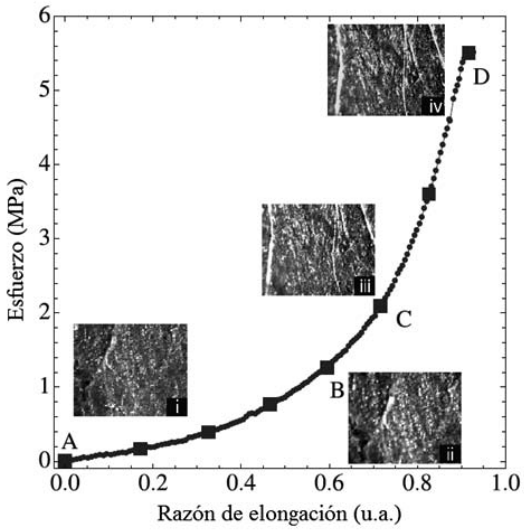

Figura 3

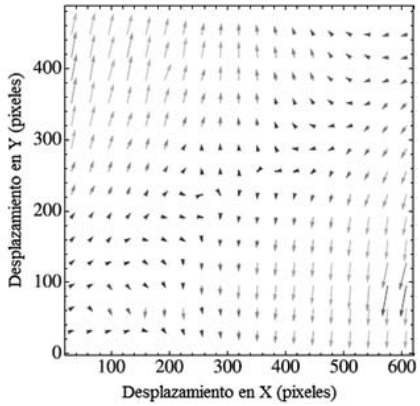

Figura 4

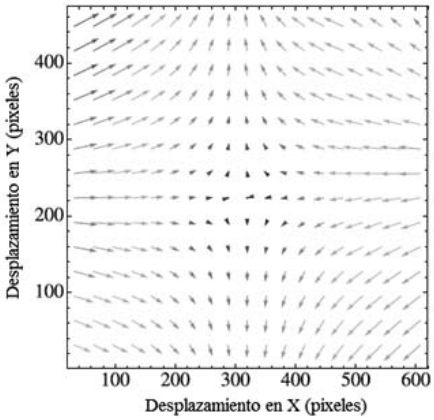

Figura 5

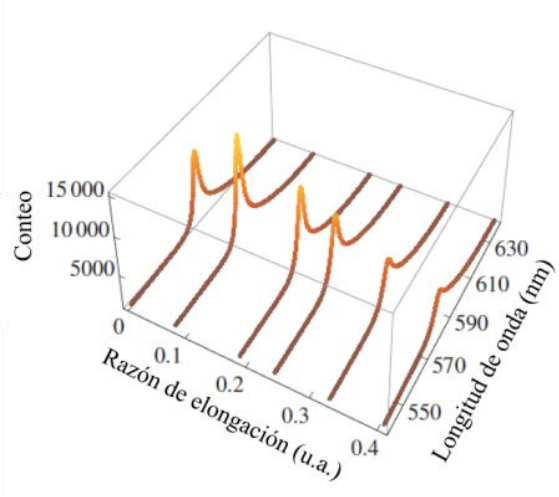

Figura 6

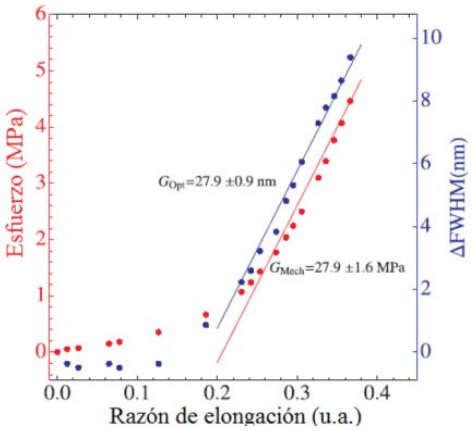

Figura 7

OFICIO DGAJ/DPI/1314/2014
VOL. 1731/14
ASUNTO: Solicitud de patente.

DRA. ANA MARÍA MARTÍNEZ VÁZQUEZ
Directora del Instituto de Investigaciones en Materiales
P r e s e n t e

En relación con el oficio número IIM/DIR/059/2014, referente a la invención denominada "SISTEMA OPTO-MECÁNICO Y METODOLOGÍA PARA EVALUAR EL COMPORTAMIENTO MACRO Y MICROMECÁNICO DE MATERIALES SUAVES Y TEJIDOS BIOLÓGICOS", le comunico que el día 20 de febrero del año en curso, se presentó ante el Instituto Mexicano de la Propiedad Industrial, la solicitud de patente de la invención de referencia, la cual quedó registrada con el número de expediente MX/a/2014/001999. Por lo anterior, envío a usted para los fines que estime conducentes copia de la documentación presentada.

A t e n t a m e n t e
"POR MI RAZA HABLARÁ EL ESPÍRITU"
Ciudad Universitaria, a 20 de febrero de 2014
EL DIRECTOR GENERAL

DR. ENRIQUE GUADARRAMA LÓPEZ

Anexo: Lo indicado.
LCS/MFP

INSTITUTO DE INVESTIGACIONES EN MATERIALES
21 FEB 2014
U. N. A. M.
DIRECCION

Instituto Mexicano de la Propiedad Industrial

INSTITUTO MEXICANO DE LA PROPIEDAD INDUSTRIAL
Dirección Divisional de Patentes

[X] Solicitud de Patente
[ ] Solicitud de Registro de Modelo de Utilidad

[ ] Solicitud de Registro de Diseño Industrial, especifique cual:
[ ] Modelo Industrial [ ] Dibujo Industrial

Antes de llenar la forma lea las consideraciones generales al reverso

Uso exclusivo Delegaciones y Subdelegaciones de la Secretaría de Economía y Oficinas Regionales del IMPI
Sello
Folio de entrada
Fecha y hora de recepción

Solicitud
Expediente: MX/a/2014/001999
Fecha: 28/FEB/2014 Hora: 18:24:45
Folio: MX/E/2014/012477
311861

I DATOS DEL (DE LOS) SOLICITANTE(S)

El solicitante es el inventor [ ] El solicitante es el causahabiente [X]

1) Nombre (s): UNIVERSIDAD NACIONAL AUTÓNOMA DE MÉXICO

2) Nacionalidad (es): MEXICANA

3) Domicilio: calle, número, colonia y código postal: 9° PISO DE LA TORRE DE RECTORÍA S/N, CIUDAD UNIVERSITARIA, DELEGACIÓN COYOACÁN, C.P. 04510

Población, Estado y País: MÉXICO, DISTRITO FEDERAL.

4) Teléfono (clave): 56 22 63 29 AL 31 5) Fax (clave): 56 65 46 44

II DATOS DEL (DE LOS) INVENTOR(ES)

6) Nombre (s): FRANCISCO MANUEL SÁNCHEZ ARÉVALO, NATANAEL BENITO CUANDO ESPITIA, JUAN ARNALDO HERNÁNDEZ CORDERO Y JOSÉ CELSO BRIONES HERRERA.

7) Nacionalidad (es): MEXICANA, MEXICANA, HONDUREÑA, MEXICANA

8) Domicilio: calle, número, colonia y código postal: TIZAPA 11, COLONIA CENTRO, C.P. 56600

Población, Estado y País: CHALCO, ESTADO DE MÉXICO.

9) Teléfono (clave): 10) Fax (clave):

III DATOS DEL (DE LOS) APODERADO (S)

11) Nombre (s): LIC. MARTHA FIGUEROA PÉREZ R.G.P. DDAJ-14782

13) Domicilio: calle, número, colonia y código postal: EDIFICIO "B" 3er. PISO, ZONA CULTURAL DE CIUDAD UNIVERSITARIA, DELEGACIÓN COYOACÁN, C.P. 04510

Población, Estado y País: MÉXICO, DISTRITO FEDERAL. 14) Teléfono (clave): 56 22 63 29 AL 31 15) Fax (clave): 56 65 46 44

16) Personas Autorizadas para oír y recibir notificaciones: LIC. LAURA CORTÉS SÁNCHEZ, LIC. YESICA MARIBEL CORONEL RIVERA, LIC. ROCIO JUAREZ VÁZQUEZ y el C. MIGUEL ÁNGEL NIEVES MARTÍNEZ.

17) **Denominación o Título de la invención: "SISTEMA OPTO-MECÁNICO Y METODOLOGÍA PARA EVALUAR EL COMPORTAMIENTO MACRO Y MICROMECÁNICO DE MATERIALES SUAVES Y TEJIDOS BIOLÓGICOS".**

18) **Fecha de divulgación previa**
Día Mes Año

19) **Clasificación Internacional** **uso exclusivo del IMPI**

20) **Divisional de la solicitud**
(Número) (Figura jurídica)

21) **Fecha de presentación**
Día Mes Año

22) **Prioridad Reclamada:**

País	Fecha de presentación: Día Mes Año	No. de serie

Lista de verificación (uso interno)

No. Hojas		
X	1	Comprobante de pago de la tasa
X	10	Descripción y reivindicación (es) de la invención
X	5	Dibujo (s) en su caso
X	1	Resumen de la descripción de la invención
X	1	Documento que acredita la personalidad del apoderado

No. Hojas		
X	4	Documento de cesión de derechos
		Constancia de depósito de material biológico
		Documento (s) comprobatorio(s) de divulgación previa
		Documento (s) de prioridad
		Traducción
	22	TOTAL DE HOJAS

Observaciones:

Bajo protesta de decir verdad, manifiesto que los datos asentados en esta solicitud son ciertos.

LIC. MARTHA FIGUEROA PÉREZ
Nombre y firma del solicitante o su apoderado

CU, UNIVERSITARIA, D.F. A 19 DE FEBRERO DE 2014
Lugar y fecha

IMPI-00-005

A P P E N D I X G

PUBLISHED ARTICLE

Biomedical Optics EXPRESS

Mechanical assessment of bovine pericardium using Müeller matrix imaging, enhanced backscattering and digital image correlation analysis

Natanael Cuando-Espitia,* Francisco Sánchez-Arévalo, and Juan Hernández-Cordero

Instituto de Investigaciones en Materiales, Universidad Nacional Autónoma de México, A.P. 70-360, Cd. Universitaria, México D.F. 04510, Mexico

natanael@iim.unam.mx

Abstract: Mechanical characterization of tissue is an important but complex task. We demonstrate the simultaneous use of Mueller matrix imaging (MMI), enhanced backscattering (EBS) and digital image correlation (DIC) in a bovine pericardium (BP) tensile test. The interest in BP relies on its wide use as valve replacement and biological patch. We show that the mean free path (MFP), obtained through EBS measurements, can be used as an indicator of the anisotropy of the fiber ensemble. Our results further show a good correlation between retardance images and displacement vector fields, which are intrinsically related with the fiber interaction within the tissue.

OCIS codes: (170.0170) Medical optics and biotechnology; (170.0110) Imaging systems; (170.6935) Tissue characterization.

References and links

1. Organ Procurement and Transplantation Network (OPTN) and Scientific Registry of Transplant Recipients, (SRTR). OPTN/SRTR 2012 Annual Data Report. Rockville, MD: Department of Health and Human Services, Health Resources and Services Administration; 2014.
2. X. Li, Y. Guo, K. R. Ziegler, L. S. Model, S. D. D. Eghbalieh, R. A. Brenes, S. T. Kim, C. Shu, and A. Dardik, "Current usage and future directions for the bovine pericardial patch," Ann. Vasc. Surg. **25**(4), 561–568 (2011).
3. K. Hammermeister, G. K. Sethi, W. G. Henderson, F. L. Grover, C. Oprian, and S. H. Rahimtoola, "Outcomes 15 years after valve replacement with a mechanical versus a bioprosthetic valve: Final report of the Veterans Affairs randomized trial," J. Am. Coll. Cardiol. **36**(4), 1152–1158 (2000).
4. J. H. Cyriax, *Diagnosis of soft tissue lesions (Vol. 1)* (Elsevier Health Sciences, 1982).
5. F. M. Sánchez-Arévalo, M. Farfán, D. Covarrubias, R. Zenit, and G. Pulos, "The micromechanical behavior of lyophilized glutaraldehyde-treated bovine pericardium under uniaxial tension," J. Mech. Behav. Biomed. Mater. **3**(8), 640–646 (2010).
6. N. Ghosh, M. F. G. Wood, S. H. Li, R. D. Weisel, B. C. Wilson, R.-K. Li, and I. A. Vitkin, "Mueller matrix decomposition for polarized light assessment of biological tissues," J. Biophotonics **2**(3), 145–156 (2009).
7. N. Cuando-Espitia, F. M. Sánchez-Arévalo, and J. Hernández-Cordero, "Enhanced backscattering measurements in bovine pericardium tensile tests," in Latin America Optics and Photonics Conference, OSA Technical Digest, paper LTh4A.22 (2014).
8. P. I. Okagbare, D. Begun, M. Tecklenburg, A. Awonusi, S. A. Goldstein, and M. D. Morris, "Noninvasive Raman spectroscopy of rat tibiae: approach to in vivo assessment of bone quality," J. Biomed. Opt. **17**(9), 090502 (2012).
9. J. C. Briones-Herrera, N. Cuando-Espitia, F. M. Sánchez-Arévalo, and J. Hernández-Cordero, "Evaluation of mechanical behavior of soft tissue by means of random laser emission," Rev. Sci. Instrum. **84**(10), 104301 (2013).
10. V. Turzhitsky, J. D. Rogers, N. N. Mutyal, H. K. Roy, and V. Backman, "Characterization of light transport in scattering media at sub-diffusion length scales with Low-coherence Enhanced Backscattering," IEEE J. Sel. Top. Quantum Electron. **16**(3), 619–626 (2010).
11. A. Lagendijk, "Observation of weak localization of light in a random medium," Phys. Rev. Lett. **55**(24), 2692–2695 (1985).
12. E. Akkermans, P. E. Wolf, and R. Maynard, "Coherent backscattering of light by disordered media: Analysis of the peak line shape," Phys. Rev. Lett. **56**(14), 1471–1474 (1986).

#241610 Received 22 May 2015; revised 2 Jul 2015; accepted 3 Jul 2015; published 20 Jul 2015

13. S. Lu and R. Chipman, "Interpretation of Mueller matrices based on polar decomposition," J. Opt. Soc. Am. A **13**(5), 1106–1113 (1996).
14. R. Azzam, "Propagation of partially polarized light through anisotropic media with or without depolarization: A differential 4 × 4 matrix calculus," J. Opt. Soc. Am. **68**(12), 1756–1767 (1978).
15. R. Ossikovski, "Differential matrix formalism for depolarizing anisotropic media," Opt. Lett. **36**(12), 2330–2332 (2011).
16. C. E. Willert and M. Gharib, "Digital particle image velocimetry," Exp. Fluids **10**(4), 181–193 (1991).
17. F. M. Sánchez-Arévalo and G. Pulos, "Use of digital image correlation to determine the mechanical behavior of materials," Mater. Charact. **59**(11), 1572–1579 (2008).
18. F. M. Sánchez-Arévalo, T. García-Fernández, G. Pulos, and M. Villagrán-Muniz, "Use of digital speckle pattern correlation for strain measurements in a CuAlBe shape memory alloy," Mater. Charact. **60**(8), 775–782 (2009).
19. P. Fratzl, *Collagen: Structure and Mechanics* (Springer, 2008).
20. R. Puxkandl, I. Zizak, O. Paris, J. Keckes, W. Tesch, S. Bernstorff, P. Purslow, and P. Fratzl, "Viscoelastic properties of collagen: synchrotron radiation investigations and structural model," Philos. Trans. R. Soc. Lond. B Biol. Sci. **357**(1418), 191–197 (2002).
21. M. J. Ju and S. Tang, "Usage of polarization-sensitive optical coherence tomography for investigation of collagen cross-linking," J. Biomed. Opt. **20**(4), 046001 (2015).

1. Introduction

Heart transplant procedures cover only a small portion of the actual needs of patients with heart related problems. In 2012, and only in the US, heart donation rates remained flat at 3.5 donations per 1000 deaths [1]. Most of the top causes of heart related diseases, such as aortic and mitral valve disorders, require valve replacement using bioprosthetic or mechanical heart valves. Bovine pericardium (BP) is a widely used soft tissue for medical applications such as valve replacement [2]. Among other interesting features, patients with BP-based valves usually do not need a life-long anticoagulation treatment [3]. Although BP is commonly used in medical applications, the knowledge to fully predict its behavior once inside the human body is still unclear, and long-term results are not fully documented. In general, *in vivo* soft tissue characterization methods are limited and very expensive [4].

Recently, digital image correlation (DIC) and Müeller matrix imaging (MMI) have been reported as useful techniques for extracting information from biological tissue [5,6]. Similarly, enhanced backscattering (EBS) measurements have shown to provide information of structural changes in soft tissue during mechanical tests [7]. In general, optical characterization methods allow for performing non-contact and less invasive procedures, particularly those intended to obtain mechanical features of soft tissue. Moreover, optical techniques for soft tissue tests have the potential to be integrated with fiber optics technology and lead to applications such as *in vivo* early tissue diagnosis [8]. In this paper, we report on the application of MMI for uniaxial tensile tests of BP previously fixed with glutaraldehyde. Our experiments are performed using a setup specifically designed for mechanical testing of soft tissue [9]. This allows for incorporating optical techniques for tissue analysis during uniaxial tension tests. In particular, data from DIC, EBS and MMI are obtained simultaneously thus providing information regarding structural changes of the tissue samples during the tensile test. In this way, the mechanical properties of the tissue can be readily correlated with the optical measurements.

2. Materials and methods

2.1 Experimental setup

The experimental setup consists of a mechanical testing device designed to perform tensile tests on thin and soft materials [9]. This mechanical "minitester" further incorporates optical elements to acquire information for EBS and MMI measurements. As depicted schematically in Fig. 1, a set of circular polarizers is used to generate and analyze the states of polarization required for MMI [6]. Images are acquired via a long working distance microscope and a CCD camera, both arranged to register the beam coming out from the sample in the forward direction (green arrows in Fig. 1). Illumination for both, MMI and EBS, is performed with a

#241610 Received 22 May 2015; revised 2 Jul 2015; accepted 3 Jul 2015; published 20 Jul 2015

pulsed, frequency-doubled Nd:YAG laser at 532nm, with a spot diameter of approximately 0.5 cm.

A second CCD camera placed as shown on the right side of Fig. 1 registers data for EBS measurements. After interacting with the sample, the scattered light in the backward direction passes through the circular polarizer for filtering of specular reflections. The EBS cone is then registered using a lens with a focal length of 45 mm and the 1024x768 CCD. This configuration provides a resolution of 0.1 mrad with no moving parts once adjustments on the alignment have been completed [10].

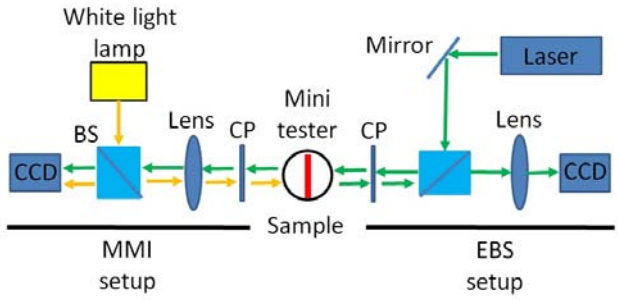

Fig. 1. Experimental setup: data for MMI, DIC and EBS are acquired during a single uniaxial test. The setup includes circular polarizers (CP), a beam splitter (BS), a laser and a white light source for illumination as well as two CCD cameras (see text).

Conventional images are recorded using white light illumination for subsequent processing using DIC. The mechanical "minitester," CCD cameras and laser trigger are controlled and synchronized with a PC via a Virtual Instrument (VI) programmed in *LabVIEW*. The VI is set to start the test in a sequential manner; first, the sample is elongated in steps of 200 μm, simultaneously acquiring white light images and data such as applied force and displacement for subsequent mechanical analysis. In order to avoid relaxation effects in the BP sample during MMI measurements, the VI is set to pause during 4 minutes once the applied load reaches a preset value. This relaxation time was determined experimentally through preliminary measurements showing that after 4 minutes, relaxation effects are negligible for MMI and EBS analysis. After this pause, the Nd:YAG laser is triggered to launch 10 pulses per each of the 16 combinations on the circular polarizers required for the Müeller matrix for the corresponding loading condition. Subsequently, the laser is triggered again to launch 10 pulses for acquiring images for EBS analysis. The VI then starts the loading procedure again for data and image acquisition under different loading conditions.

2.1 Sample preparation

As other connective tissues, BP has a complex structure based on three layers: the serosa, the fibrosa and the epipericardial connective tissue layer [2]. The fibrosa layer is mainly made of wavy bundles of collagen fibers and elastin; the properties of this layer provide bovine pericardium with the appropriate features for its clinical use as a biological patch and for heart valve replacement [2,3]. For our experiments, pericardial sacs from 18 month-old calves were collected fresh from a local slaughterhouse. Sample sheets of selected sacs were cut and hung in custom-built frames; subsequently, they were cross-linked with glutaraldehyde (GA). The fixation process was carried out during 24 hours at 4°C, using 0.5% GA in 0.1 M phosphate buffered saline solution with a pH of 7.4 [5]. Next, the sheets were washed in distilled water and subsequently cut with a special jig, according to the ASTM D1708 standard, to obtain samples with a dog bone shape. Finally, the samples were immersed and stored in a glycerin solution until the experiment was performed.

#241610 Received 22 May 2015; revised 2 Jul 2015; accepted 3 Jul 2015; published 20 Jul 2015

2.3 Mean free path measurements (EBS)

According to EBS theory, when light interacts with multiple scattering media a twofold enhancement in the diffuse intensity appears in the exact backward direction. The factor of two arises from photons going over time-reversed paths, which constructively interfere in the direction of backscattering [11,12]. Out from the exact backscattering direction, the enhancement decreases inversely proportional to the mean free path (MFP), forming an angular distribution that decays to the diffusive intensity. For non-absorbing media, the intensity α near the backscattering direction as a function of the solid angle θ is given by [12]:

$$\alpha(\theta) = \frac{3}{8\pi}\left[1+\frac{2z_0}{l}+\frac{1}{(1+ql)^2}\left(1+\frac{1-e^{-2qz_0}}{ql}\right)\right] \quad (1)$$

In this expression, $q = 2\pi\theta/\lambda$, l is the photon mean free path; $\boldsymbol{z_0}$ is given by the boundary conditions and for a plane geometry $\boldsymbol{z_0} \sim 0.7\ l$ [12]. Equation (1) shows that for fixed boundary conditions and wavelength λ, the shape of the EBS cone is fully described by the mean free path (MFP), which is a measure of the turbidity of the sample. This allows for obtaining an experimental measurement of the MFP for a sample upon evaluation of the width of the angular distribution of the backscattered intensity. In our experiments, the intensity recorded in each pixel of the CCD was mapped to the scattering angle considering both, the pixel width and the focal length as described in [10]. Subsequently, Eq. (1) was fitted to the experimental data to obtain the MFP (i.e., l) in terms of the wavelength and the width of the EBS cone.

2.4 Experimental Müeller matrix decomposition

Müeller calculus is a well-established technique for homogeneous transparent media. Nevertheless, when dealing with inhomogeneous materials such as tissue, the elements of the experimental Müeller matrix can mislead to a non-physical behavior of the material [6]. Scattering, depolarization and inhomogeneity of the material must be considered in data analysis in order to obtain the relevant physical parameters from the matrix. Two methods have been reported aiming at solving this difficulty: the so-called polar decomposition [13], and the differential matrix formalism [14]. We used the extension of the differential matrix formalism for depolarizing anisotropic media [15], in which the spatial derivative of the Müeller matrix along the propagation axis follows the relation:

$$\frac{d\mathbf{M}(z)}{dz} = \mathbf{m}\mathbf{M}(z) \quad (2)$$

$\mathbf{M}(z)$ represents the position dependent Müeller matrix and $\mathbf{m}$ is the differential matrix. Equation (2) implies that the optical effect caused by the material scales with the sample thickness [14,15]. For the boundary condition $\mathbf{M}(z = 0) = \mathbf{I}$, where $\mathbf{I}$ is the identity matrix, the solution of Eq. (2) has the form $\mathbf{M} = \exp(d\mathbf{m})$, in which d is the path traveled by the light beam. In our experiments, we construct the experimental Müeller matrix using the different combinations of the circular polarizers for a sample of thickness d. Each pixel in the acquired images thus has an associated Müeller matrix; these are subsequently used to obtain the differential matrix $\mathbf{m}$ using Jordan decomposition. The Müeller matrix provides information such as linear retardance (δ), optical rotation and average depolarization [6]. We focus on the linear retardance, which is related to the stress-induced changes in refractive index.

2.5 DIC analysis

Digital image correlation is a full-field and non-contact technique to measure displacement/strain vector fields (DVFs) on the surface of materials. With the series of acquired images during the mechanical tests, the DVFs $\boldsymbol{u}_k\ (x_k, y_k)$ and $\boldsymbol{v}_k\ (x_k, y_k)$ between pair of images were calculated by using the Willert and Gharib algorithm [16]. Here $\boldsymbol{u}$ and $\boldsymbol{v}$ represent the displacement vectors of the object or region of interest in the x and y directions,

#241610 Received 22 May 2015; revised 2 Jul 2015; accepted 3 Jul 2015; published 20 Jul 2015

respectively [17,18]. The position coordinates in each image are represented by x and y and subindex k indicates the corresponding object/region of interest, which is defined as an area of 64 × 64 pixels. Hence, a full image is divided in subimages (64 × 64 pixels) used to perform the DIC analysis yielding the DVF at throughout the full image for a given loading condition. The in-plane strains in the sample were evaluated by minimizing the errors of a six parameters linear model (typically used in linear elasticity theory) and previously used in other materials including bovine pericardium [17,18]. This minimization yields the values for the normal strain in the x and y directions (ε_x and ε_y), translation, shear strain (ε_{xy}), and in-plane rotation within the analyzed region of the sample [18].

3. Results and discussion

Macroscopically, BP can be seen as an ensemble of fibers that tend to align in the direction of the stress axis during the mechanical test [5]. Before rupture, the tissue exhibits three main regions in the stress-elongation ratio curve. In the first region, the elongation ratio increases with small changes in the applied stress as depicted in Fig. 2. After a certain value of the elongation ratio, some of the fibers start to align, and a highly nonlinear transition region appears. Finally, when most of the fibers are aligned, a third region showing a linear response to elongation can be identified. As shown in Fig. 2(b), these three regions were obtained in our experiments for elongation ratios of 0.0-0.15 (region I), 0.15-0.3 (region II) and 0.3-0.4 (region III). Changes in the fiber alignment for different loading conditions are evident in the images shown in Fig. 2(a): as the load increases, the fibers tend to align along the direction of the force applied to the sample.

Fiber alignment modifies the scattering conditions within the tissue thereby affecting the MFP. As shown in Fig. 2, the resulting MFP measured through EBS varies under different loading conditions. The preset values for the load on the sample were set to obtain data for EBS within the three regions of the stress-elongation curve. As seen in the figure, the MFP exhibits an inflexion point within region II, indicating a transition zone in which the collagen fibers of the tissue begin to align. These ordered-disordered transitions are characteristic for collagen fibers based tissue [19]. Within region III, both the stress and MFP show a similar behavior increasing with the elongation ratio. This can be related to an increase in scatterers per unit volume as the elongation ratio increases. Upon loading the BP sample, the tissue experiences a contraction along the transversal direction owing to the Poison ratio. This contraction leads to a rearrangement of the collagen fibers along the horizontal direction thus increasing the number of scatterers (fibers) per unit of volume. Hence, the scattering force within the sample increases along with the MFP [10]. This may be related to the intrafibrillar structure of collagen, and has been directly observed during mechanical tests by means of small-angle X-ray scattering (SAXs) measurements [20]. We therefore believe that EBS measurements provide an alternative means for evaluation of intrafibrillar modifications in densely packaged collagen tissue.

#241610 Received 22 May 2015; revised 2 Jul 2015; accepted 3 Jul 2015; published 20 Jul 2015

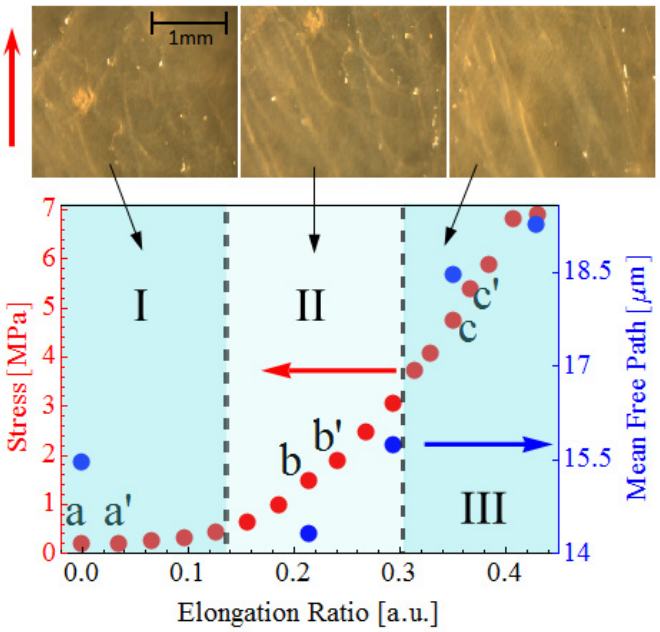

Fig. 2. Stress vs. elongation ratio curve of the BP tensile test (red points, left axis) and MFP as function of elongation ratio (blue points, right axis). The pictures show representative images for each region of the stress vs. elongation ratio curve. The arrow on the left side of the images indicates the direction of the load during the uniaxial tension test.

While the mechanical data recorded during the tests are linked to the behavior of the fibers at a macroscopic scale, EBS measurements provide information related to fiber interaction within the illuminated portion of the sample. More localized information of the tissue is provided by DIC and MMI. These provide data at the micron scale within the probed area acquired by the imaging system. The left column of Fig. 3 shows the images obtained using white light illumination of the BP sample together with the corresponding DVFs (superimposed white lines with arrow heads). By means of DIC, the DVFs are obtained upon comparing subsequent images for different loading levels [5]. In this case, we present three sets of vectors, one for each of the regions shown in the stress-elongation curve (i.e., regions I, II and II). The DVFs for each region were obtained from image pairs acquired during the elongation test; the selected points of the curve for this calculations are shown in Fig. 2 and are labeled as a-a' (region I), b-b' (region II) and c-c' (region III). For comparison, the corresponding images for the linear retardance (δ) in degrees, calculated through differential matrix decomposition, are shown in the right column of the same figure. The linear retardance for each pixel is represented in an arbitrary color scale and is shown together with the corresponding DVFs.

The DVFs in Fig. 3(a) display a larger displacement component along the perpendicular axis to the applied load. Since Fig. 3(a) corresponds to elongation conditions of region I, in which the fibers are not aligned, some compression is to be expected owing to fiber displacement during the initial elongation. The retardance image for the initial conditions (right column of Fig. 3(a)) shows a relatively regular distribution of low retardance. This is a consequence of the highly isotropic orientation of the fibers for this loading condition, where alignment is not yet achieved. Notice also that the zones with highest retardance in Fig. 3(a) tend to match the elongation components of the DVFs, suggesting that the vectors are attracted to the zones with higher retardance. For elongation ratios beyond 0.2 (region II), the DVFs exhibit a clear change as the predominant component is aligned towards the loading axis, as seen in Fig. 3(b). This alignment is associated with the appearance of high retardance

#241610 Received 22 May 2015; revised 2 Jul 2015; accepted 3 Jul 2015; published 20 Jul 2015

zones increasing the contrast of the image. In general, the DVF in Fig. 3(b) tends to run from high retardance zones to lower retardance zones as in Fig. 3(a). Finally, the DVF of Fig. 3(c) shows the characteristic hyperbolic pattern of an aligned ensemble of fibers, as expected within the linear region of the tensile test [5]. In this case the retardance image displays a spread of higher retardance zones, owing to an increased interaction among the microfibers within the tissue [19]. In general, high retardance zones tend to spread as the elongation ratio increases. Notice however that for larger loading conditions, some of the zones with low retardance seem to attract the DVFs as it is shown at lower part of Fig. 3(c). This may be attributed to buckling in the central part of the image, which has been previously reported to appear in BP tissue samples under high stress conditions [5].

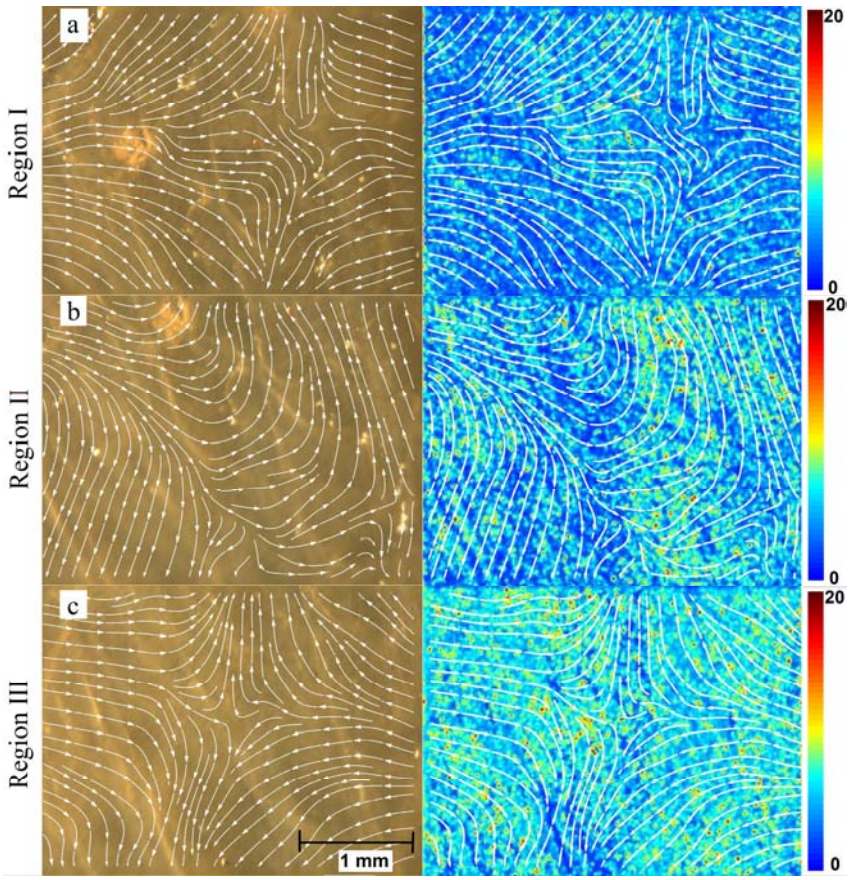

Fig. 3. Left column: white light images of the BP and their corresponding DVF. Right column: retardance images obtained from MMI analysis and their corresponding DVF. The scales for the retardance images are in degrees; each row is associated with different regions of the tensile test (see text). DVFs correlate well with retardance images obtained by means of MMI during the tensile test (Visualization 1).

Another interesting feature of the retardance images is the localized points of high retardance. These localized points reach the maximum values of the color scale and become more evident as the load increases as it is illustrated in Fig. 3. An increase in collagen fiber interactions typically leads to the rupture of cross-links between adjacent fibers [19]. Mechanical testing of BP tissue has shown to generate cross-linking rupture creating localized zones of high shear stress [5]. This condition is achieved under the loading conditions shown in region III of Fig. 2 and leads to changes in birefringence that appear as localized zones with high retardance as shown in Fig. 3. Similar conditions have been observed when

#241610 Received 22 May 2015; revised 2 Jul 2015; accepted 3 Jul 2015; published 20 Jul 2015

studying collagen cross-linking effects in corneal tissue using polarization sensitive OCT [21].

4. Conclusions

We have demonstrated that optical measurements, in particular DIC, MMI and EBS, can be incorporated into tensile tests of BP tissue. While DIC provides information related to the interaction between the tissue matrix and the collagen fibers, MMI accounts for interfibrillar changes in the tissue structure; EBS in turn shows intrafibrillar effects during the elongation test. The proposed arrangement is thus capable to provide information at different scales during a single mechanical test. It is clear from EBS measurements that the mean free path (MFP) within the tissue sample increases with elongation. Longer MFPs are associated to the linear region of the tensile test, where fibrils are in a more compact and aligned arrangement. The displacement vector fields (DVFs) obtained by DIC show a good correlation with the retardance images calculated by means of MMI. Our observations suggest that DVFs tend to run from low retardance zones to high retardance zones, where more fiber interaction is present. Similar trends in changes of tissue structure during mechanical tests have been reported using more elaborated techniques such as OCT and SAXs. We therefore believe that incorporation of these optical tools for tissue characterization represents a promising approach for elucidating mechanical properties of materials used for biological prosthetic devices.

Acknowledgments

This work was partially supported by DGAPA-UNAM through grants PAPIIT IT100215, IT101215. Natanael Cuando-Espitia acknowledges support from CONACYT. The authors are also grateful to Professor Enrique Geffroy-Aguilar for facilitating the laser equipment used in this work.